UNIVERSIDAD NACIONAL AUTÓNOMA DE MÉXICO

POSGRADO EN CIENCIA E INGENIERÍA DE MATERIALES
INSTITUTO DE INVESTIGACIONES EN MATERIALES

Atomic structure and properties of amorphous, liquid and amorphous porous Cu-Zr alloys by *ab initio* simulations

Tesis

que para optar por el grado de Doctor en Ciencia e ingeniería de Materiales

Presenta:

M. en C. Jonathan Galván Colín

Tutor:

Dr. Ariel Alberto Valladares Clemente
Instituto de Investigaciones en Materiales

Miembros del comité tutor:

Dr. Jacques Soullard Saintrais
Instituto de Física

Dra. Renela María Valladares Mc Nelis
Facultad de Ciencias

México, D.F. 2016

Ciudad Universitaria, Cd. Mx. Noviembre 2016

Declaración de autoría

Yo, M. C. e I. M. Jonathan Galván Colín, declaro que la presente tesis, con título: "Atomic structure and properties of amorphous, liquid and amorphous porous Cu-Zr alloys by *ab initio* simulations", y el trabajo correspondiente son míos.

Yo confirmo que:

- Este trabajo fue hecho totalmente durante el periodo de mi doctorado en el Posgrado en Ciencia e Ingeniería de Materiales de la UNAM.
- Ninguna parte del presente trabajo ha sido mandada para ningún otro tipo de grado o certificación en la presente Universidad, ni en ninguna otra institución.
- La autoría de todo el material consultado se le atribuye debidamente a sus respectivos autores.
- Cuando se ha citado el trabajo de otros autores, siempre se ha dado la fuente de origen. Con la excepción de dichas citas, toda la información contenida en el presente trabajo es de mi autoría.
- He reconocido todas las fuentes de ayuda usadas en el trabajo.
- Cuando el trabajo fue hecho en colaboración con otros, he especificado qué es lo que han hecho los otros y cuales fueron mis contribuciones.

Firma:

Fecha:

"That is why I write for myself [...] For the man who writes and yet makes his name and actions to be engraved on stone, it is he who lives with the hope that his words could be read and that the future generations will praise his actions and good sense. But there is nothing to praise in my words; my actions are not worth of acclamation; my science is bitter for the heart and pleases nobody [...] Mankind will not repeat my words to improve themselves with my knowledge. I have given up on all hope to ever be read or understood."

-Sinuhe the Egyptian-

Synopsis

In this dissertation a method to generate amorphous, liquid and amorphous porous Cu-Zr alloys based on the *undermelt-quench* amorphization method is proposed. The resulting amorphous and liquid structures are compared with the experimental alloys available in the literature, they fairly agree so that our method is validated and it could be transferred to other bulk metallic glasses. From this agreement we calculated the electronic and phonon density of states for amorphous and liquid samples, while for amorphous porous structures the Fukui functions were calculated to qualitatively analyze reactivity. When comparing the properties slight differences arose, but in general, the experimental trends were followed by our simulated structures. Furthermore, amorphous porous structures were analyzed carefully due to the limitations in determining certain aspects of the topology: pore size/surface ratio. Although further studies related to the generation of amorphous porous material are needed, the results shown in this work drive us to carry on with the onerous but fascinating work of materials science.

En este trabajo se propone un método basado en el método de amorfización San Diego (desarrollado en el grupo), para generar estructuras amorfas, líquidas y amorfas porosas. Las estructuras resultantes amorfas y líquidas son comparadas con las aleaciones experimentales reportadas en la literatura. Ya que los resultados concuerdan, podemos decir que nuestro método es válido y que se puede transferir a otros vidrios metálicos de bulto. A partir de la comparación y la posterior validación de nuestras estructuras amorfas y líquidas, calculamos las densidades de estado electrónicas y fonónicas; mientras que las funciones de Fukui fueron calculadas para las estructuras amorfas porosas, con el objeto de hacer un análisis cualitativo de la reactividad. Asimismo, las estructuras amorfas porosas se analizaron cuidadosamente debido a que existen limitaciones para determinar el tamaño del poro, es decir, el límite de la superficie. A pesar de que se necesitan más estudios sobre la generación de materiales amorfos porosos, los resultados que se muestran en el presente trabajo nos motiva para continuar con el oneroso, pero fascinante, trabajo de la ciencia e ingeniería de materiales.

Acknowledgements

Firstly, I would like to express my sincere gratitude to my advisor Prof. Ariel Alberto Valladares Clemente for the continuous support of my Ph.D study and related research, for his patience, motivation, and immense knowledge. His guidance helped me in all the time of research and writing of this dissertation. Also because he provided me the opportunity to join his team, and special thanks for the continuous food supplies: *"there is nothing better than a friend, unless it is a friend with chocolate"*.

Besides my advisor, I would like to thank the rest of my thesis committee: Prof. Héctor Octavio Murrieta Sánchez, Prof. Pablo de la Mora y Palomar Askynasy, Prof. Susana Orozco Segovia and Dr. Fernando Álvarez Ramírez, for their time to read this thesis and their insightful comments and encouragement.

My sincere thanks also goes to Prof. Jacques Soullard Saintrais and Prof. Renela María Valladares Mc Nelis, who accepted to be in my Ph.D. committee.

I thank my fellow labmates for the stimulating discussions and for all the fun we have had in the last years: `ggwp report my team`.

Also I thank CONACyT for the financial support of my Ph.D. study and DGAPA-UNAM for continued funding to carry out projects IN101798, IN100500, IN119105, IN119908, IN112211 and IN110914.

Many thanks to DGTIC-UNAM for the CPU time provided, whenever it was possible, to perform most of the simulations of this dissertation. My gratitude to Instituto de Investigaciones en Materiales for providing the research facilities during the last 7 years, and to Universidad Nacional Autónoma de México, my *alma mater*, which has been my second home for the last 13 years.

Last but not the least, I would like to thank my family for supporting me throughout my post-graduate studies and writing this thesis.

Contents

List of my Publications

I. *"New Approaches to the Computer Simulation of Amorphous Alloys: A Review"*, A. A. Valladares, J. A. Díaz-Celaya, J. Galván-Colín, L. M. Mejía-Mendoza, J. A. Reyes-Retana, R. M. Valladares, A. Valladares, F. Álvarez-Ramírez, D. Qu, J. Shen, Materials **4**, 716-781 (2011)

II. *Structural and Electronic Properties of $Cu_{64}Zr_{36}$ BMG by ab initio Molecular Dynamics"*, J. Galván-Colín, A. A. Valladares, R. M. Valladares, A. Valladares, Materials Research Society Symposium Proceedings **1517**, DOI: 10.1557/opl.20121757 (2013).

III. *"Short-range order in ab initio computer generated amorphous and liquid Cu-Zr alloys: A new approach"*, J. Galván-Colín, A. A. Valladares, R. M. Valladares, A. Valladares, Physica B **475**, 140-147 (2015).

IV. *"Ab initio generation of binary alloy foams: the case of amorphous $Cu_{64}Zr_{36}$"*, J. Galvan-Colín, A. A. Valladares, R. Valladares, A. Valladares, In Proceedings of the 2nd International Electronic Conference on Materials, Sciforum Electronic Conference Series, Vol. 2 **B001**, doi:10.3390/ecm-2-B001 (2016).

Abbreviation Index

SRO	Short Range Order
PDF	Pair Distribution Function
RDF	Radial Distribution Functional
XRD	X-Ray Diffraction
BT	Bathia-Thornton
PPDF	Partial Pair Distribution Function
PRDF	Partial Radial Distribution Function
BAD	Bond-Angle Distribution
CNA	Common Neighbor Analysis
BMG	Bulk Metallic Glass
BMGF	Bulk Metallic Glass Foam
EL	Expanding Lattice
MSD	Mean Square Displacement
CN	Coordination Number
AIMD	*Ab initio* Molecular Dynamics
RGL	Rosato-Guillope-Legrand
ND	Neutron Dispersion
RMC	Reverse Monte Carlo
MD	Molecular Dynamics
DFT	Density Functional Theory
HOMO	Highest Occupied Molecular Orbital
LCAO	Linear Combination of Atomic Orbitals
eDOS	Electronic Density of States
LDA	Local Density Aproximation
NVT	Constant number of particles N, volume V, and temperature T
MO	Molecular Orbitals
vDOS	Vibrational Density of States
FF	Fukui Function
GEOPT	Geometry Optimization

DTS	Default Time Step
3DTS	Three Times the Default Time Step
TM	Transition Metal
ILSRO	Icosahedron-like Short-Range Order
FK	Frank-Kasper
CND	Coordination Number Distribution
peDOS	Partial Electronic Density of States
FFT	Fast-Fourier Transform
MRO	Medium-Range Order
ap-	Amorphous Porous

Preface

The study of the atomic interactions that take place in a material are paramount to understand the properties that characterize such material because they are determined by its atomic structure. Periodicity in crystals boosted the development of a wide spectrum of properties in these materials; however, throughout history, structurally disordered matter has played an important role from the technological point of view. Amorphous materials as semiconductors, porous and metals have gained a lot of attention due to the extraordinary properties that exhibit, yet full knowledge and understanding of the mechanisms that give birth to those properties is an undergoing task. Glassy materials are among those which have been relevant since its transparency was not fully understood.

About fifty years ago, bulk metallic glasses hit the scientific community with the $Au_{75}Si_{25}$ glass because it had been very difficult to grow such materials; they could only be prepared as thin films. This discovery fostered further investigations on this materials which were based on multicomponent alloys due to the fact that the more elements involved, the higher the stability of the bulk metallic glass. These materials have extraordinary mechanical properties, even better than steel in some cases because their elastic deformation could be greater. Nonetheless, the premise of materials science and engineering is to study and discover the driving processes that a material undergoes in order to manipulate them and modify those properties according to specific needs. For this reason, in this work we focus on the binary alloy Cu-Zr. But why this alloy?

First, the Cu-Zr system is binary, so its composition is relatively simple compared with other multicomponent alloys; therefore, a study of the atomic structure would be far easier. Secondly, experimental work is constrained by the conditions that can be generated physically, while computer simulations are a wide open window that allows us to explore beyond the environments that could be built on Earth. Then, if one generates a model that accurately represents a real situation, the model can be extrapolated to the predictive field or even transferred to other situations. So, by using computer simulations we may be able to have resolution to the atomic level when studying the generation and the properties of the simulated system; this is particularly useful in the case of the binary Cu-Zr alloy.

To carry out the computer simulations a powerful tool is used in this work: classical mechanics+quantum mechanics, i.e., studying the dynamics of the system based on the

electron density within the density functional theory framework allows us to avoid fitting parameters that frequently cannot be transferred to other systems, so the first principles methodology provides a robust engine to study thoroughly the generation of materials. Although these simulations are computationally demanding, an appropriate set of simulation parameters along with existing computational power would save computational time without compromising the quality of the calculations.

With these ideas in mind, in the present work a new approach, based on a succesful methodology that has proven to be effective in the generation of amorphous semiconducting structures, is proposed to generate amorphous, liquid and amorphous porous Cu-Zr alloys.

In the first chapter an introduction is given on the main features that structurally disordered matter exhibits. Some tools to characterize the structures are presented and a brief review of some works related to Cu-Zr alloys and its properties are listed. In the second chapter the underlying theoretical apparatus is discussed: density functional theory, molecular dynamics, the code used to generate the structures and the properties. The third chapter presents the methodology and the parameters used. In the last part of this dissertation the results of the amorphous, liquid and amorphous porous samples are presented in chapters 4, 5 and 6, correspondingly. They are treated separately in order to fully address the discussion related to the particular properties. Finally, a summary is given and the conclusions of the work are shown.

Chapter 1

Introduction

1.1 Background

Although metals have been used for thousands of years, their application fields have grown dramatically during the last centuries due to emerging new techniques and metallurgical processes. Particularly, the advent of the quantum theory in the last century helped to clarify some aspects related to the properties of metals that until that time were thought to originate from certain assumptions, e.g., Drude's model. Moreover, deepening in the study and applications of metals has not been restricted to crystalline alloys, but has included complex non-crystalline structural compounds.

Unlike crystalline materials, the lack of long-range structural ordering in non-crystalline materials hinders their study since there is a wide range of plausible structures associated to a disordered material (Fig. 1.1). However, these materials do have a peculiarity: short-range order (SRO), and it is this SRO the main cause of the properties that structurally disordered matter exhibits.

In spite of the lack of translational ordering, structurally disordered materials may be characterized by their local atomic environment, i.e., by taking any atom in the system as origin and analyzing its vicinity up to a distance of $\sim$5 Å.

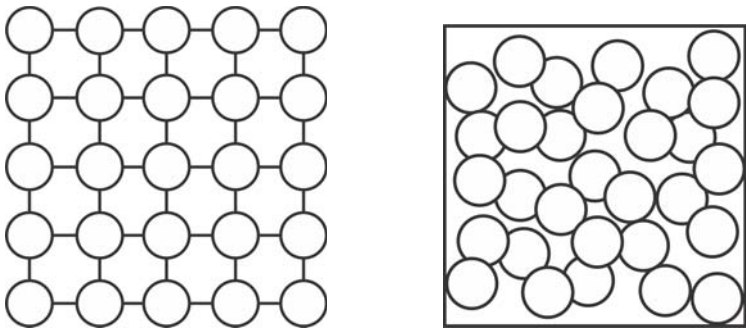

Figure 1.1. 2D representation of a typical (left) crystalline material, and (right) an amorphous material.

In order to do such analysis several approaches are used. Among them, one of the

most widely used is the study of the pair distribution function (PDF), which is sometimes referred to as the radial distribution function (RDF), and viceversa. Although the PDF and RDF are related, different information can be extracted from each one. Therefore, special care should be taken when analizing the information they provide, either quantitative or qualitative, for references to them as a simple indicator of disorder in structures are utterly common. However, a deep scrutiny of these functions, specially the PDF, may lead to valuable information about SRO.

Now lets see what each function means and the information that can be obtained from each one, for such invaluable information extracted from these is relevant in the strenous task of understand how the SRO in amorphous alloys leads to very distinctive properties.

1.1.1 Distribution functions

Among the several methods of studying and characterizing the structure of disordered materials the most common used distributions functions since they can be obtained either experimentally via different measurement techniques or theoretically from computer models and simulations.

1.1.1.1 Structure factor - $S(q)$

Before exploring the distribution functions it is worth mentioning that scattering experiments via diffraction theory are the origin of these distribution functions: x-rays, neutrons and electrons are used to determine the structure of matter. Although x-ray diffraction (XRD) is the most popular, the topological analysis of structurally disordered matter is based on scattered beams that interfere with each other, which results in different intensities depending on the relative positions of atoms in a given material.

In crystals, the structure factor $S(q)$ provides Bragg peaks. In the case of structurally disordered matter, since there is no long-range order, the structure factor enables PDF to be calculated via a Fourier transformation, thus $S(q)$ is a means to the pair distribution, the radial distribution function and whatever quantitative information that can be obtained from them. Therefore, obtaining and analyzing the structure factor is very important in the study of both amorphous and liquid systems.

There is a set of partial structure factors S_{ij} called the Bathia-Thornton (BT) partial structure factors [1] which are obtained from the Fourier transformations of the local number density and concentration fluctuations in the long-wave-length limit ($Q \to 0$). The partial BT structure factors are $S_{NN}(q)$, $S_{CC}(q)$ and $S_{NC}(q)$, which represent the mean-square fluctuations in the particle number (or number density ρ_0), the concentration and

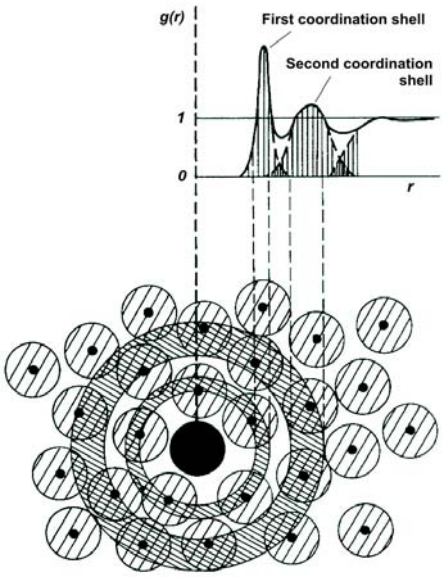

Figure 1.2. Schematical representation of the pair distribution function [4].

their cross term, respectively (with c_A and c_B the corresponding concentration of A-type and B-type atoms). $S_{NN}(q)$ oscillates around one, $S_{CC}(q)$ oscillates around the value of the corresponding alloy concentration $c_A c_B$, and each approaches those values in the high-Q region respectively. On the other hand, $S_{NC}(q)$ oscillates about zero and vanishes for random mixtures, i.e, mixtures in which the local number density of A and B atoms around an A-type atom is the same as that around a B-type one; thus taking $Q \to 0$, $S_{NN}(q) \to 1$, $S_{CC}(q) \to c_A c_B$ and $S_{NC}(q) \to 0$.

Although BT partial structure factors have a useful significance in the long-wave-length limit because they can be related directly to the thermodynamic properties of a binary alloy [2], they are not the only structure factors that can be derived, but their formulation is better than others when discussing the relation between structure and thermodynamic quantities for mixtures [3].

1.1.1.2 PDF - $g(r)$

This distribution function is very useful because both experimentalists and theoreticians can easily compare to their resulting structures. The PDF, $g(r)$, gives the probability of finding an atom in a region dr located in at a distance r from another atom taken as the origin (Fig. 1.2). Due to atom sizes the distribution is not uniform; but it is for large values of r because interparticle influences vanish.

Although the information that can be extracted from the PDF might seem limited due

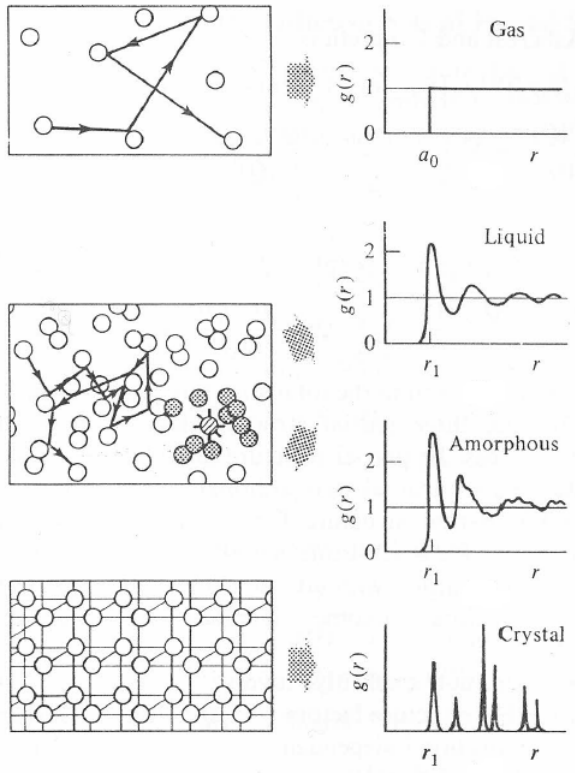

Figure 1.3. Schematic diagram of atomic distribution (left) and pair distribution function (right) in the gas, liquid, amorphous and crystal states [3].

to the one-dimensional representation of a three-dimensional structure, it is useful. As seen in Fig. 1.2, the PDF does not only validate the disorder topology of a given sample (in the case of a crystalline material sharp and well-defined peaks are exhibited), it also provides information about the coordination shells and sub-shells. Thus, its qualitative interpretation may lead to important information about the local atomic environment which is paramount in disordered materials. Furthermore, quantitative data can be obtained from the PDF as well via a simple mathematical manipulation.

In order to clearly differentiate among gaseous, liquid, amorphous and crystalline phases, see the 2D atomistic schematic representations and PDFs in Fig. 1.3.

1.1.1.3 RDF - $J(r)$

Similar to the PDF, the radial distribution function $J(r)$, RDF, is also used in the study of the structure of non-crystalline materials. Unlike the PDF, the RDF corresponds to the number of atoms in a spherical shell of width $r + \mathrm{d}r$, and is defined as

$$J(r) = 4\pi r^2 \rho_0 g(r), \tag{1.1}$$

where $\rho_0 = N/V$ is the number density, N is the number of atoms in the system and V is the volume of the sample cell. By integrating the first peak of the RDF up to a cutoff distance r_c, quantitative data such as the nearest neighbor number n or coordination number can be calculated as

$$n = \int_0^{r_c} J(r)\mathrm{d}r = \int_0^{r_c} 4\pi r^2 \rho_0 g(r)\mathrm{d}r. \tag{1.2}$$

However, for binary alloys the following applies. First the different atomic constituents have to be taken into account, that is, the number of A-type atoms N_A and B-type atoms N_B, which have associated their corresponding concentrations $c_A = N_A/N$ and $c_B = N_B/N$. Now the total number of atoms N is the sum of both atomic species $N = N_A + N_B$. Moreover, there is the average number density of every atom type, i.e., $\rho_{ij}(r)$, which shows the density of j-type atoms at a distance r from an i-type atom. Then, the partial pair distribution function (PPDF) arises as follows

$$g_{ij} \equiv \frac{\rho_{ij}(r)}{\rho_0 c_j} = \frac{\rho_{ij}(r)}{\rho_j}, \tag{1.3}$$

where $\rho_j = \frac{N_j}{V} = \frac{N}{V}\frac{N_j}{N}$. Since long-range atomic pair correlations in non-crystalline solids vanish, the probability of finding pair correlations with increasing distance will tend to the average value, hence, interparticle distance must be identical, which leads to $g_{ij} = g_{ji}$. Thence, the partial radial distribution funtcion (PRDF) is defined as

$$J_{ij} = 4\pi r^2 \rho_{ij}(r) = 4\pi r^2 \rho_0 c_j g_{ij}(r), \tag{1.4}$$

consequently, the partial coordination number

$$n_{ij} = \int_0^{r_c} J_{ij}(r)\mathrm{d}r = \int_0^{r_c} 4\pi r^2 \rho_0 c_j g_{ij}(r)\mathrm{d}r. \tag{1.5}$$

At this point it is noteworthy to consider that several approaches are used to calculate the partial and total coordination numbers, e.g., the ones considered by Waseda [3].

One of them involves the consideration of a symmetrical first peak in the RDF. This approach better suits the case of amorphous semiconductors since a clear first peak appears in the corresponding RDF due to the nature of the bonds, which is not the case of amorphous alloys based on transition metals. Another approach considers the integration of the first peak up to the first minimum in the RDF. However, this method sometimes overestimates the coordination number for if the first minimum does not correspond to

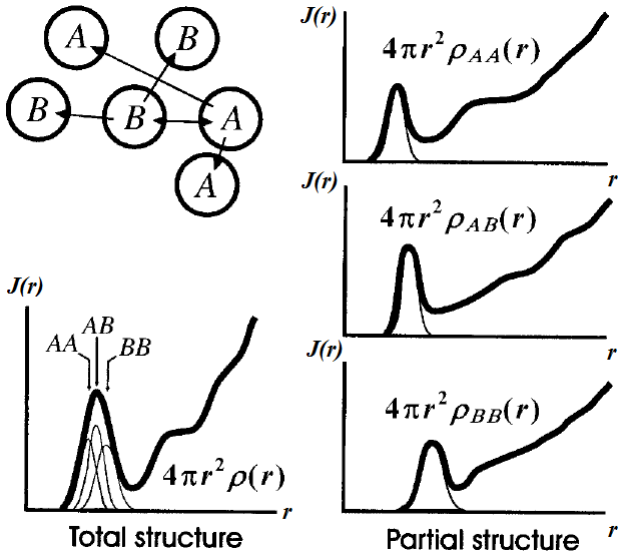

Figure 1.4. Schematics of the total and partial radial distribution functions of a disordered binary alloy AB [3].

zero, spurious counts of second neighbors are taken into account besides fluctuations in the RDF (due to the number of atoms simulated in computer simulations for example) might lead to an ambiguous determination of the first minimum.

In the case of a binary alloy, a third approach can be used. This involves, the calculation of the partial n_{ij} by direct integration of the first peak in the corresponding J_{ij} up to the first minimum and then adding such partial coordination numbers to calculate the total coordination n. This is based on the construction of the total PDF from the weighted addition of the first peak of each PPDF [5] (Fig. 1.5):

$$\begin{aligned} n &= \sum_k n_k = \sum_k \int_0^{r_k} J_k(r)\mathrm{d}r = 4\pi\rho_0 \sum_k \int_0^{r_k} r^2 g_k(r)\mathrm{d}r \\ &= 4\pi\rho_0 \left[\int_0^{r_{ii}} r^2 W_{ii} g_{ii}(r)\mathrm{d}r + 2\int_0^{r_{ij}} r^2 W_{ij} g_{ij}(r)\mathrm{d}r + \int_0^{r_{jj}} r^2 W_{jj} g_{jj}(r)\mathrm{d}r \right]. \quad (1.6) \end{aligned}$$

In the above equation, r_{ij} are the corresponding cutoff distances upon which the integration is made and W_{ij} are the weight factors which are obtained via

$$W_{ij} = \frac{(\#\text{ i-type atoms}) \times (\#\text{ j-type atoms})}{[(\#\text{ i-type atoms}) + (\#\text{ j-type atoms})]^2}. \quad (1.7)$$

Equation 1.7, corresponding to the last method described above, would be used to calculate the coordination number throughout the present work.

1.1.1.4 BAD

So far we have seen how qualitative and quantitative information of a given amorphous structure via the PDF and RDF can be obtained. However, since these distributions provide information about neighbor distances from a given atom, one can pick the first and second peak positions in order to correlate them with the origin atom by means of the angle they form. By doing so with every triad of atoms, the bond-angle distribution (BAD) function can be calculated. In order to do this, the criterion to determine whether two atoms are bonded or not is based on the cutoff distance r_c, which was used in the coordination number calculation, and is considered as the interatomic distance.

From this, in a binary alloy there would be six partial BADs which correspond to A-A-A, B-A-A, B-A-B, B-B-B, A-B-B and A-B-A triads. These partial distributions are useful to discern the bonding geometry of A-type and B-type atoms in a structurally disordered sample. Then, the form of the bond-angle distribution (BAD) would be a function of all possible SRO geometries present in the amorphous sample; that is, if the sample resembles a crystal, then the BAD would have localized peaks around the characteristic angles of the crystalline structure, e.g. a localized peak in 109.5° for a cubic diamond structure. If, on the contrary, the sample lacks long-range order (LRO) then the peaks in the BAD would become smooth due to the many different arising geometries; nevertheless, prevailing peaks that should indicate the presence of any possible preferred geometry might appear.

Despite the information provided by the BAD, there is not an explicit way to quantify the contributions of different geometries in a sample. A possible solution would be to roughly adjust either a gaussian or lorentzian function to the BAD at peak positions of the corresponding geometries, i.e., if one is looking for ideal icosahedra or icosahedron-like SRO then the peaks should be adjusted at 60°, 63.5°, 108°, 116.5° and 138.2° [6]. Now we will consider another method to characterize and quantify the local environment in a disordered material.

1.1.1.5 Common Neighbor Analysis

In analyzing the atomic structure of disordered materials, one faces the task of extracting important information from the resulting numerical coordinates, thus it becomes difficult to identify complex ordering phenomena from coordination numbers, RDFs and BADs. Although the BAD is very useful to figure out the possible tendency of the SRO geometries that arise upon melting or amorphization, it does not provide quantitative information of how much of this or that geometry is present in the sample.

The structural analysis technique often referred to as the common neighbor analysis

(CNA), that was first used by Blaisten-Barojas [7] and later generalized by Honeycutt and Andersen [8], is based on the decomposition of the first two peaks of the PDF according to the environment of the pairs. As in the BAD, the first minimum between the first and second peaks in the RDF is the cutoff distance defined as the interatomic distance, i.e., the maximum distance at which a pair of atoms are considered 'bonded'. Each pair of atoms is classified with a set of indices, $jklm$, that specify the local environment of the pair. The first index, j, refers to the peak of the PDF to which the 'bonded' pair under consideration belongs to; the second index, k, is the number of near neighbors shared by the 'bonded' pair; the third index l is the number of bonds between these common neighbors; and the fourth index m is used to discern among configurations with the same first three indices that have different topology [8,9]. Therefore, the CNA provides a way to clearly ascertain contributions of fcc, hcp, bcc and icosahedral packing, e.g., indices corresponding to fcc and hcp packings are 1421 and 1422, respectively; 1441 and 1661 correspond to crystalline bcc; 1551 and 1541 correspond to icosahedral packing, and so on.

CNA is easier to interpret than Voronoi polyhedra [1] analysis because minor perturbations in the coordinates dramatically change such analysis. This represents a problem when one wants to identify between fcc and hcp close packings, which are often present in disordered metals.

1.2 Amorphous metals

As mentioned in the former section, metals have had a great impact in technology development which include both crystalline pure metals and alloys, as well as non-crystalline metals. But what is a non-crystalline metal?

Non-crystalline metals are either amorphous or glassy and liquid. The first are characterized by the disordered structure they have upon fast cooling from the liquid phase; being rather alloys than pure metals, for it has been proven that amorphization of pure (transition) metals is not achievable at room temperature due to recrystallization upon cooling. On the other hand, in alloys—mainly multicomponent—disparities in atom sizes aid to reduce atomic mobility which leads to high viscosities thus preventing the formation of crystalline phases during cooling. As a result, the material reaches the metastable amorphous phase. If cooling is not fast enough, then the system has enough time to rearrange in crystalline domains generating a crystalline phase. And the liquids, of course, are the ones

[1] Voronoi polyhedra (in 3D), polygons or cells (in 2D) are partitions of the space or a plane based in atomic sites. For each atomic site there is a corresponding region consisting of all points closer to it than any other. A well-known Voronoi cell is the Wigner-Seitz cell.

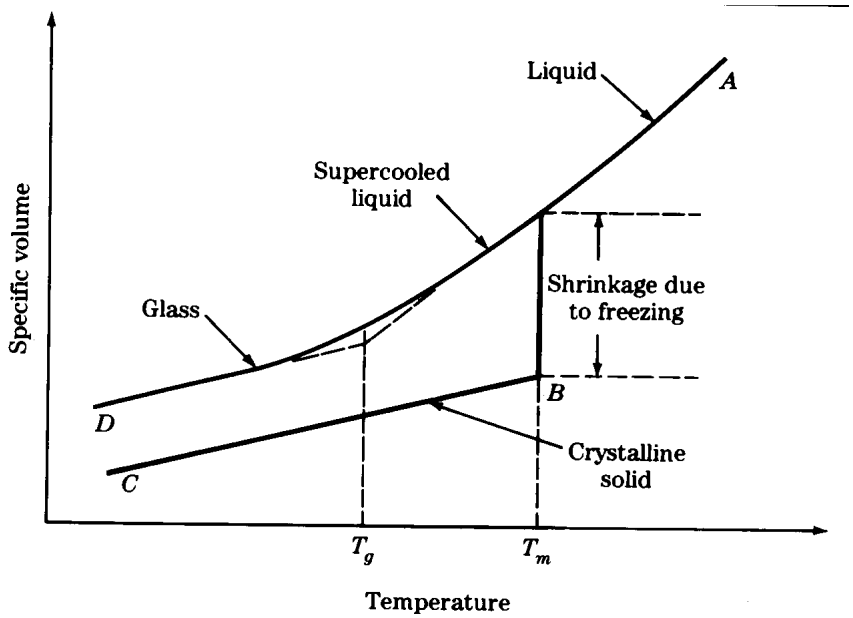

Figure 1.5. Schematic representation of how a glass is formed compared to a crystalline solid by tracking how the volume changes as the temperature is lowered.

characterized by a state above the melting temperature for pure elements, or the *liquidus* temperature for alloys. These will be addressed in the next section.

The generation of the first metallic glass dates back to 1960 when Klement *et al.* obtained an Au-Si amorphous alloy experimentally [10]. What differentiates a metallic glass from a common amorphous alloy is the presence of the glass transition or vitrification (Fig. 1.5). In those early days, preparation of specimens was limited to ribbons, thin films or wires due to the high cooling rates needed for molten materials. The reason was that, in order to achieve such high rates, heat could only be extracted quickly from the sample if the material had one small dimension, which of course limited the thickness of the samples.

Further investigation led to alloys either ternary, quaternary, quinary, etc., which enhanced both thickness and reduced cooling rates. With this, thicknesses of milimeters were accesible and a new kind of materials was born, the so-called ***bulk metallic glasses*** (BMGs).

BMGs generated interest because they exhibited extraordinary mechanical properties than their crystalline counterpats. For example, since they lack long range order there is an absence of grain boundaries and dislocations which leads to an enhanced resistance to wear and corrosion and to an improved toughness [11]. Moreover, unlike oxide glasses and ceramics which are insulators, BMGs are good electrical conductors. However, studies on the electronic properties of BMGs have been disregarded in the literature for they have

been focused mainly on their mechanical properties, such as the strenght and fracture limit.

In order to understand the ruling mechanisms that govern the features of BMGs, a study of the structure in the atomistic regime and its relation to such properties is essential. For that purpose, multicomponent BMGs are inadequate since it becomes an exhaustive task due to the presence of different kinds of atomic types. A plausible option to overcome this, is to study a simple system like a binary or—at worse—a ternary alloy. Such alloys would be ideal for experimentalists and theoreticians to work with, letting them to deeply explore the interactions among atoms due to electron interactions. Thus, that is the reason why in the present work we chose binary amorphous Cu-Zr; whose properties would be further discussed in section 1.4.

There are two structural properties that can be verified via the PDF of metallic glasses that would help to discern between the general features of amorphous materials and liquids: a split of the second peak, also known as a bimodality or shoulder which is a consequence of the non-directional nature of the metallic bond which tends to arrange atoms around a central atom in several well-defined coordination shells and subshells; the ratio of peak positions of the first peak (r_1) to that of the second peak (r_2) which has proven to be around 1.67, and the ratio of the first peak to the third peak (r_3) about 1.95, contrary to the ratios in the liquid state which are 1.85 and 2.70, respectively [3]. However, it is well-known that such positions may vary due to thermal vibrations, which are higher in liquids.

One of the objectives of this dissertation is to study several properties of amorphous Cu-Zr. However, a new kind of material based on BMGs gained relevance during the past decade, those materials are called ***bulk metallic glass foams*** (BMGFs) which, besides exhibiting an amorphous state, are porous.

1.2.1 Amorphous porous metals

Although pores in an alloy might be regarded as a major structural defect since it may be the cause of defficiencies in a material, there has been a great interest in generating porous materials lately and many experimental techniques to control pore size and form have been devised [12]. Some works have been devoted to generating porous metals and the study of these systems is an ongoing task [13].

The spectrum of applications of porous metals is very wide because of the unique combination of their topology and the inherent material properties of the atomic constituents. From such potential applications, those related to mechanical properties stand out. They can be used as lightweight structural members, impact/blast mitigators, fluid filters, catalytic supports, biocompatible medical implants, etc [13]. Nonetheless, the most widely

known porous materials are aluminum-based which are limited by the properties of their base alloys, although they can easily be fabricated. Other porous materials based on stronger materials usually need complex processes to be generated [13].

With the advent of the *nano era*, materials scientists have been driven to a nanoscopic design of new materials that would exhibit certain desired properties. Among the different experimental techniques, dealloying by selective dissolution of the most electrochemically constituent is one of them and leads to nanosized structures [14]. According to the International Union of Pure and Applied Chemistry (IUPAC), micro and mesopore sizes are at most 2 nm (20 Å) and 50 nm, respectively [15], and the corresponding micro and mesoporous structures are often referred to as nanoporous metals.

Non-desired features are not constrained only to porous metals and alloys but also to BMGs, for their major limitations reside in poor ductility and high processing costs which have restrained their mass production and commercialization. At this point the idea of addressing such drawbacks was thought by considering a material that *mixes* both porous and BMG features, i.e., that would combine their corresponding advantages into a promising new material: a bulk metallic glass foam.

Albeit, BMGFs are limited by their manufacturing process difficulting their characterization and application. Complications arise when trying to control pore size and bulk homogeneity. Therefore the BMGFs generated so far are based on multicomponent alloys with micron to milimeter pore sizes.

The first successful method to create a BMGF experimentally was reported by Schroers *et al.* in 2003. They generated a palladium-based material with pores of 200-1000 μm [16]. Other reported BMGFs were: $Zr_{57}Nb_5Cu_{15.4}Ni_{12.6}Al_{10}$ with pore sizes of 25-50 μm [17]; successive experimental works of Lee *et al.* [18], Demetreiou *et al.* [19] and Brothers *et al.* [20] should be mentioned. Porous materials, *per contra*, have been very difficult to simulate. From the theoretical point of view, a few methods have been formulated which either involve reconstructing the model from experimental data or mimicry of the experimental processes followed to generate the amorphous porous samples. The main disadvantage of the former is that one is limited by the experimental data available, while in the latter there is a lack of transferability [21].

A few years ago Valladares *et al.* reported an *ab initio* approach called the expanding lattice (EL) method to generate amorphous porous structures which uses neither empirical data nor any mimicring of experimental processes [**?**]. They simulated nanoporous carbon and silicon [23,24]. This approach has proven to be effective in reproducing some properties of amorphous carbon as well [25,26]. Moreover, Santiago-Cortés *et al.* recently reported the application of a dealloying-like process along with the EL approach to generate amorphous

nanoporous carbon, silicon, copper and silver [27]. They found that a depletion in the PDF appears in the medium range regime which could be useful to roughly estimate the pore size. However these *ab initio* techniques have not been applied strictly to alloys.

Once again, by using a widely studied and simple system as Cu-Zr we can simulate an amorphous porous metallic glass foam once the BMG is generated. Thus, not only the amorphous porous Cu-Zr is investigated in this work, but also amorphous porous copper and zirconium; the details of the generation of the amorphous porous alloy would be discussed further in chatper 3.

1.3 Liquid metals

Among disordered metallic materials there are also liquid metals which also lack long range order due to the difference in energy contrary to the solid state. Liquid phase has been intriguing for researchers because when a liquid is cooled down an interesting phenomena takes place, the onset of a phase change: nucleation. The inital phase of crystallization (nucleation) triggers grain growth which eventually ends with the full phase change into solid state. However, the early stage of nucleation still remains a mystery due to the short time scale of such transformation.

By studying the atomic behavior in the liquid phase of a binary alloy upon amorphization, a way to figure out the governing mechanisms of phase transformation in metals could be devised.

The obvious fact that melting a crystalline metal does not turn it into a non-metal implies that much of the interest in molten metals is the behavior of their conduction or valence electrons. Chemical, thermal, reological and other properties interest metallurgists and engineers; however, the scientific concern has much to do with the motion of unbound electrons in a disordered array of ions [2]. Thus, based on their thermodynamics and electronic properties, as well as on the structural data obtained from diffraction experiments, various methods are used to classify liquid binary alloys [3] if the hard sphere model is considered:

I. The total structure factor $S(Q)$ does not exhibit a subpeak or asymmetry in the first peak, i.e, a random-mixing behavior. Also, the maximum of the partial structure factor $i - j$ lies between the other two partial structure factors ($i - i$ and $j - j$) maxima. In this case the size, charge number and electronegativity of the elements of the alloy are similar.

II. Whether there is a subpeak in the first peak of the total $S(Q)$, the behavior is

compound-forming-like. This has to do with large differences in the size, charge number and electronegativity of the alloy constituents.

III. Although a subpeak in the first peak is not found, the partial structure factor $i-j$ resembles one of the like-atom partial structure factors.

However, if the constituents of a binary alloy have different physico-chemical properties deviations from the simple mixture of hard spheres of different sizes are observed.

Another interesting worth-studying property of liquids is the one related to the dynamics over a constant temperature stage: the mean-square displacement (MSD). The MSD is often used to analyze the average evolution and dynamics of a liquid structure in order to discern whether the behavior is of a liquid, or an amorphous material (e.g. glass), based on the difference in the position of the i-th atom at a certain time $\overline{r}_i(t)$, and its initial reference position $\overline{r}_i(0)$. The MSD is defined as

$$MSD = \langle|\overline{r}_i(t) - \overline{r}_i(0)|^2\rangle. \tag{1.8}$$

From the MSD, one can extract useful information on the diffusivity of the atoms in a simulation. If the system is a solid, the MSD saturates to a finite value; the MSD will grow linearly if the system is liquid. Therefore, the diffusion coefficient D can be obtained by calculating the slope of the linear behavior of a liquid, where D (in $[\frac{m^2}{s}]$) is

$$D = \lim_{t\to\infty} \frac{1}{6}\langle|\overline{r}_i(t) - \overline{r}_i(0)|^2\rangle. \tag{1.9}$$

1.4 The amorphous Cu-Zr system

As we referred in section 1.2, the Cu-Zr binary alloy has been studied experimentally and from computer simulations. Those studies were mainly focused on the atomic structure for different concentrations. Although a few studies have been published, other properties as the electronic or vibrational have been disregarded. In this section a review of some reports about studies on the structure, electronic and phonon properties of amorphous and liquid Cu-Zr alloys is made.

1.4.1 Morphology

Mendelev *et al.* [28] proposed a qualitative study of the disordered structure via semiempirical potentials based on adjustable parameters from the crystalline properties of $Cu_{64.5}Zr_{35.5}$.

They reported a XRD structural analysis along with a comparison to computer simulations. PDFs, coordination numbers (CNs) and first neighbor distances were reported as well. In addition, they showed that there exists an icosahedral ordering tendency in their resulting structures by performing a BAD characterization.

Wang *et al.* [29] studied the metallic glass $Cu_{64.5}Zr_{35.5}$. They prepared a rod and a ribbon of 1 mm thickness each by melt spinning. To characterize their samples they used high energy XRD and reported the reduced PDF $G(r)$:

$$\begin{aligned} G(r) &= \left[\frac{J(r)}{r} - 4\pi r\rho_0\right] = \left[\frac{4\pi r^2\rho_0 g(r)}{r} - 4\pi r\rho_0\right] \\ &= 4\pi r\rho_0\left[g(r) - 1\right] \end{aligned} \tag{1.10}$$

Furthermore, they performed *ab initio* molecular dynamics (AIMD). They applied a many-body Rosato-Guillope-Legrand-like (RGL) potential to a 128-atom cell ($Cu_{64.1}Zr_{35.9}$) [30]. Once the sample was equilibrated at 2400 K, they quenched it at 2.5, 5 and 10×10^{12} Ks^{-1} rates using a 1 fs time step. They argued that due to the existence of icosahedral SRO, the formation of the metallic glass is favored since Cu-centered icosahedral clusters are less distorted than Zr-centered clusters.

Mattern *et al.* [31] reported a study of $Cu_{65}Zr_{35}$, $Cu_{50}Zr_{50}$ and $Cu_{35}Zr_{65}$ metallic glass using amorphous ribbons prepared by melt spinning. Using both XRD and neutron dispersion (ND) they characterized the samples and reported total PDFs, CNs, experimental density, and first neighbor distances based on Reverse Monte Carlo (RMC) simulations. First coordination shell was found to be 12 for Cu and 14 for Zr using Voronoi polyhedra; however, they concluded that there is no short-range dominant structure.

Jakse and Pasturel [32] studied both amorphous and liquid Cu_xZr_{1-x} via AIMD (with $x = 0.28, 0.46, 0.64, 0.80$) applied to a 256 cubic cell using a time step of 3 fs. Although a computational approach lets one to deepen into the analysis of the structural properties, they only reported PPDFs. Moreover, first neighbor distances, coordinations and diffusion coefficients were reported. The information they extract from a common neighbor analysis showed that there is a preferential icosahedral SRO.

Li *et al.* [33] reported both experimental and simulational results of $Cu_{35}Zr_{65}$ and $Cu_{50}Zr_{50}$ concentrations. The PPDFs obtained with classical molecular dynamics (MD) and RMC, along with a BAD and Voronoi polyhedra, led them to conclude that the samples exhibit the formation of a solid matrix with liquid interstices, which is related to the presence of icosahedral-like clusters and the glass forming ability of the material.

Sun *et al.* [34] simulated the liquid and glassy phase of $Cu_{60}Zr_{40}$ using Finnis-Sinclair potential. Although the alloys were studied over a wide range of temperatures, no com-

parison with the experiment was made. They reported partial PDFs, CNs, first neighbor positions, mean-square displacements (MSD) and diffusion coefficients. They concluded that icosahedral SRO is maximized as temperature decreases; besides, Cu atoms diffuse more than Zr atoms due to the mass difference.

Antonowicz *et al.* [35] performed a XRD study of $Cu_{33}Zr_{67}$, $Cu_{60}Zr_{40}$ and $Cu_{64}Zr_{36}$ alloys. Although they presented CNs and difussion coefficients, they argued that their structural results are inconclusive and that an *ab initio* or MD study would provide deep structural insight.

Lagogianni *et al.* [36] reported MD results based on tigh-binding-like potentials with second moment approximation. They calculated total PDFs of Cu_xZr_{100-x} alloys with $x = 20, 40, 60, 80$, and reported that the number of icosahedral clusters increases as temperature decreases. They concluded that Cu-rich alloys have a larger number of icosahedral clusters. Moreover, from Density Functional Theory (DFT) calculations, they reported the charge distribution at the highest occupied molecular orbital (HOMO) for some clusters. In all cases, Zr-Cu and Cu-Zr orbital overlapping was favored rather than Cu-Cu overlapping, suggesting tighter atomic bonds.

Valencia-Balvín *et al.* [37] used classical MD with a RGL approach for crystalline, amorphous and liquid $Cu_{46}Zr_{54}$. They obtained PDFs, BADs, CNs, as well as phonon spectra and diffusion coefficients. As other previous reports, they conclude the presence of distorted icosahedral clusters as building basis of their resulting amorphous structures. Their vibrational densities of states for their amorphous sample exhibit peaks at 19 THz for Cu and 8 THz for Zr; no total phonon spectra were reported nor any comparison with experiment was made.

Valladares *et al.* [**?**, 38] previously reported AIMD results of amorphous $Cu_{64}Zr_{36}$. Based on a linear combination of atomic orbitals (LCAO) approach they reported total and partial PDFs, CNs and first neighbor distances. The strong presence of icosahedral SRO in their reported BADs and its relation with the PDFs was discussed.

Holland-Moritz *et al.* [39] reported the static structure factors of Zr-Cu alloy melts ($Zr_{50}Cu_{50}$, $Zr_{66.7}Cu_{33.3}$, $Zr_{41.2}Cu_{58.8}$) combining ND and synchrotron radiation. Furthermore, Bhatia-Thornton structure factors were calculated. They showed that, although it is assumed that glass forming ability in Zr-Cu alloys is related to icosahedral SRO in the melt, their liquid Zr-Cu samples do not exhibit a dominant icosahedral SRO ordering.

Hao *et al.* [40] studied liquid Cu_xZr_{100-x} alloys ($x = 80, 72, 65, 57, 50, 33.3$). By correlating the low diffusivities in their structures with the presence of some specific clusters, including icosahedra, they argued that such clustering was responsible for slowing dynamics in the composition range $50 \leq x \leq 70$, which has often been related to an enhanced

vitrification of the material.

1.4.2 Properties

Oelhafen *et al.* [41] ($Cu_{60}Zr_{40}$, $Cu_{40}Zr_{60}$ and $Cu_{30}Zr_{70}$), **Nguyen *et al.*** [42] (Cu_xZr_{100-x} with $x = 20, 25, 33, 50, 66, 75$), **Fujiwara** [43] and **Krey *et al.*** [44] ($Cu_{65}Zr_{35}$, $Cu_{50}Zr_{50}$ and $Cu_{35}Zr_{65}$), **Takahara and Narita** ($Cu_{65}Zr_{35}$) [45], **Walker *et al.*** [46] (Cu_xZr_{x-100}, with $x = 46, 71, 89$) are examples of some reports of the electronic density of states (eDOS). In these works two important contributions related with Cu d band and Zr d band were shown. Furthermore, the existence of available states at the Fermi level due to Zr is reported, while deeper states are related to Cu.

Hua *et al.* [47] reported first neighbor distances, CNs and CNA. They also calculated the eDOS by AIMD for Cu_xZr_{100-x} alloys ($x = 36, 46, 50, 56, 64$). Their results are consistent with the ones commented above, i.e., that Zr is reponsible for the presence of states at the Fermi level.

As for vibrational properties, besides Valencia-Balvín [37], **Suck *et al.*** [48] ($Cu_{46}Zr_{54}$) and **Kobayashi and Takeuchi** [49] ($Cu_{57}Zr_{43}$) reported a large number of low frequency vibrational modes in the amorphous state.

Recently, **Nakashima *et al.*** [50] reported the phonon dispersion of $CuZr_2$ metallic glass. By using high resolution X-ray dispersion they observed acoustic-like longitudinal propagations and determined the phonon spectrum. Moreover they observed the existence of two peaks in the low energy regime which could be the so called "bosonic peaks" observed in several amorphous materials.

Chapter 2

Theoretical basis

In this chapter I present a general view of the underlying theoretical basis for this project. First, the density functional theory (DFT) apparatus is presented. Then, I present some ideas about molecular dynamics (MD) and finally I include the theory behind the computational code used in the present thesis, which mixes both DFT and MD. Throughout this chapter the reader must have in mind that atomic units are used.

2.1 Density functional theory

Any problem related to the electronic structure of matter leads one to find the solution of Schrödinger's equation. However, in many cases an interest in systems which involve a large number of atoms or molecules whose interactions do not depend on time arises.

Although finding the solution of Schrödinger's equation might appear to be an easy task, it is not. Up to now an exact solution to this equation applied to molecular systems is not known; nevertheless, one of the most important and popular approximations to calculate properties of molecules and solids is the **density functional theory**, whereby the groundstate electronic energy E_0 and other properties are approximated by means of the electronic density ρ_0.

In 1964 Hohenberg and Kohn proved that the groundstate wave function, the groundstate energy and all the electronic properties of a system were determined by a function that only depended on the coordinates of the particles, i.e., the groundstate electronic density $\rho_0(\overline{r})$, and so the groundstate electronic energy would be a functional of the density: $E_0[\rho_o]$ [51]. To prove such idea Hohenberg and Kohn supposed that the atomic nuclei α remained fixed which, in turn, would define the external potential that acts on the *ith* electron

$$v_{ext}(\overline{r}_i) = -\sum_{\alpha} \frac{Z_\alpha}{r_{i\alpha}}. \tag{2.1}$$

With this they showed that the groundstate electronic density determines the external potential. Moreover, based on Hohenberg-Kohn's assumption the Hamiltonian operator

becomes

$$\hat{H} = \sum_{i=1}^{N} \left(-\frac{1}{2}\nabla_i^2 \right) + \sum_{i=1}^{N} v_{ext}(\overline{r}_i) + \sum_{i<j}^{N} \frac{1}{r_{ij}}, \tag{2.2}$$

where the first and second terms are the kinetic energy T and the nucleus-electron interaction V_{ne} correspondingly, and the last term is the electron-electron interaction V_{ee}. Now, since E_0 is a functional of the electron density, so are the terms individually,

$$E_0[\rho_0] = T[\rho_0] + V_{ne}[\rho_0] + V_{ee}[\rho_0]. \tag{2.3}$$

Recalling the fact that $\int \rho(\overline{r})\mathrm{d}\overline{r} = N$ and that the potential energy due to the nucleus-electron atraction can be written as $E_{ne}[\rho_0] = \int \rho_0(\overline{r}) V_{ne}[\rho_0]\mathrm{d}\overline{r}$ [52], the expresion for the energy becomes

$$E_0[\rho_0] = \int \rho_0(\overline{r}) V_{ne}\mathrm{d}\overline{r} + F_{HK}[\rho_0], \tag{2.4}$$

where the so-called *universal* Hohenberg-Kohn functional appears as:

$$F_{HK}[\rho_0] = T[\rho_0] + V_{ee}[\rho_0]. \tag{2.5}$$

Although the functional F_{HK} is not known and has to be calculated, Hohenberg and Kohn proved that it is a universal function of the density, not depending explicitly on the external potential, and that it exists so that the energy $E[\rho]$ obtains its minimal value, which is the ground-state energy of the system $E_0[\rho_0]$ [53].

To tackle the problem of not knowing F_{HK}, Kohn and Sham [54] suggested a new approach to approximate it—as previously devised in the Hartree-Fock scheme using a Slater determinant to represent the exact wave function of a non-interacting system of N electrons immersed in an effective potential V'. Their suggestion was to use the same expression of the kinetic energy of the non-interacting reference system $T'[\rho] = \sum_i^N \langle \phi_i | -\frac{1}{2}\nabla^2 | \phi_i \rangle$ for the real interacting system by reminding that $\rho = \sum_i^N \langle \psi_i(\overline{r}) | \psi_i(\overline{r}) \rangle$ and accounting for the separation of the functional $F[\rho]$ as

$$F[\rho(\overline{r})] = T'[\rho(\overline{r})] + J[\rho(\overline{r})] + E_{XC}[\rho(\overline{r})], \tag{2.6}$$

where the second term is the classical Coulomb interaction and the last term is the exchange-correlation energy which is defined as

$$E_{XC} \equiv (T[\rho] - T'[\rho]) + (V_{ee}[\rho] - J[\rho]) = T_R[\rho] + E_{NC}[\rho], \tag{2.7}$$

where T_R is the residual part of the kinetic energy not covered by T', and E_{NC} takes into account the non-classical electrostatic contributions.

However, the problem of defining a V' in such a way that it provides a Slater determinant characterized by the same density of the real system prevails. To this purpose the separation made by Kohn and Sham is used (eq. 2.7), where the expression of the energy of the real interacting system is

$$E[\rho(\overline{r})] = T'[\rho] + J[\rho] + E_{XC}[\rho] + E_{ne}[\rho], \tag{2.8}$$

which in turn becomes

$$\begin{aligned} E[\rho(\overline{r})] &= -\frac{1}{2}\sum_{i}^{N}\langle\psi_i|\nabla^2|\psi_i\rangle - \frac{1}{2}\int\frac{\rho(\overline{r})\rho(\overline{(r)'})}{|\overline{r}-\overline{r}'|}\mathrm{d}\overline{r}\mathrm{d}\overline{r}' \\ &\quad + E_{XC}[\rho(\overline{r})] - \int\rho(\overline{r})V_{ne}\mathrm{d}\overline{r}. \end{aligned} \tag{2.9}$$

At this point a similar approach to the Hartree-Fock method is applied, i.e., to determine the condition that the $\{\psi_i\}$ orbitals must fullfill in order to minimize the energy under the well-known constraint $\langle\psi_i|\psi_j\rangle = \delta_{ij}$ by means of the variational principle [53]. The resulting equation is

$$\left(-\frac{1}{2}\nabla^2 + V_{eff}(\overline{r}_1)\right)\psi_i = \epsilon_i\psi_i \tag{2.10}$$

where the potential V_{eff} and the potential due to exchange and correlation are respectively

$$V_{eff} = \int\frac{\rho(\overline{r}')}{|\overline{r}-\overline{r}'}\mathrm{d}\overline{r}' + V_{XC}(\overline{r}) + V_{ne}(\overline{r}), \tag{2.11}$$

$$V_{XC} = \frac{\delta E_{XC}[\rho]}{\delta\rho}. \tag{2.12}$$

From equation 2.12, V_{XC} depends on $\rho(\overline{r})$, which in turn depends on the $\{\psi_i\}$. Therefore, equations 2.10 and 2.11 have to be solved in a self-consistent way as depicted in figure 2.1.

In spite of this ingenious mathematical apparatus, the value of E_{XC} still remains unknown. In other words, if E_{XC} were known, the Kohn-Sham equations would lead to the exact value of the energy of the system. Even though such thing does not happen, Kohn and Sham proposed an approximation to calculate the value of the exchange-correlation energy: **the local density approximation (LDA)**, which has been widely used in many DFT-based calculations.

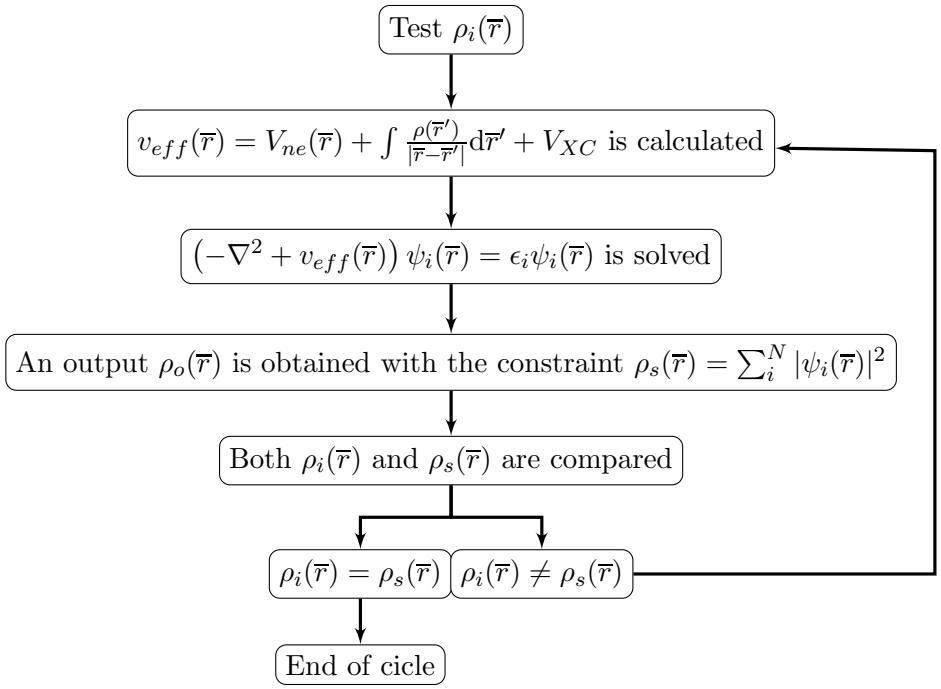

Figure 2.1. Kohn-Sham self-consistent process.

2.1.1 Local density approximation

In spite of the way of incorporating the kinetic energy term $T'[\rho]$ in their equations, Kohn and Sham still found the problem partially unsolved for the exchange-correlation energy for it had no explicit form. Even nowadays the search for an accurate value of such energy is still and ongoing task and has been one of the greatest challenges for DFT theoreticians.

In order to approximate the exchange-correlation energy, and recalling the early attempts of Thomas [55] and Fermi [56] to find a functional expression of the energy of a uniform electron gas, Kohn and Sham used the uniform electron gas formula for the unknown part of the rest of the energy functional; thus introducing their local density approximation [53] so that

$$E_{XC}^{LDA}[\rho] = \int \rho(\overline{r}) \epsilon_{XC}(\rho) \mathrm{d}\overline{r}, \tag{2.13}$$

where ϵ_{XC} represents the exchange-correlation energy per particle of a uniform electron gas of density ρ. Furthermore, the corresponding exchange-correlation potential becomes

$$v_{XC}^{LDA}(\overline{r}) = \frac{\delta E_{XC}^{LDA}}{\delta \rho(\overline{r})} = \epsilon_{XC}(\rho(\overline{r})) + \rho(\overline{r}) \frac{\delta \epsilon_{XC}(\rho)}{\delta \rho}, \tag{2.14}$$

and the Kohn-Sham equations are

$$[-\frac{1}{2}\nabla^2 + v(\overline{r}) + \int \frac{\rho(\overline{r}')}{|\overline{r} - \overline{r}'|}\mathrm{d}\overline{r}' + v_{XC}^{LDA}(\overline{r})]\psi_i = \epsilon_i\psi_i. \tag{2.15}$$

The self-consistent solution of equations 2.15 defines the Kohn-Sham LDA, or commonly referred to as the LDA method. In addition, the term $\epsilon_{XC}(\rho)$ can be divided into separate exchange and correlation contributions

$$\epsilon_{XC}(\rho) = \epsilon_X(\rho) + \epsilon_C(\rho), \tag{2.16}$$

where the exchange part is given by the Dirac exchange energy functional [53]

$$\epsilon_X(\rho) = -\frac{3}{4}\left(\frac{3}{\pi}\right)^{\frac{1}{3}}\rho(\overline{r})^{\frac{1}{3}}, \tag{2.17}$$

whereas the correlation part is calculated from computations or numerical interpolations like the ones obtained by Monte Carlo calculations of Ceperly and Alder [57], or the widely used parameterizations of Vosko, Wilk and Nusair [58] and Perdew and Wang [59]. The application of the LDA method to solids involves the knowledge of the exchange-correlation energy of a nonuniform system from the uniform electron gas results, applied to infinitesimal portions of the nonuniform electron distribution and then summing the individual contributions, $\epsilon_C(\rho)\rho(\overline{r})\mathrm{d}\overline{r}$, over all space.

In the early formulation of the LDA method it was considered that it could be suitable only for systems with slowly-varying electron densities, discarding atoms and molecules from its applicability range. However, it has been proven that it also works, although to some extent, for inhomogeneous electronic density systems, as covalent materials, and highly correlated systems as metals.

2.2 Molecular dynamics

Molecular Dynamics (MD) is a computational simulation technique where the time evolution of an atomic or molecular system is followed by the integration of the equations of motion [60]. In order to do this the degrees of freedom of the atomic nuclei must be handled separately from the electrons. To this purpose the Born-Oppenheimer approximation is used since it is well-known that the atomic mass mainly concentrates in the nucleus, i.e., the mass of the nucleus is larger than the electron mass. This fact makes the electrons in an atom to instantaneously react to any motion coming from the nucleus. Therefore, for any set of positions of the nuclei Schrödinger's equation can be solved to obtain the electronic contribution to the energy which, along with the nucleus-nucleus repulsion, determines the

total energy of the system. In this way, the forces acting on the nuclei can be calculated considering a conservative system governed by the following newtonian equations of motion

$$m_i\ddot{\overline{r}}_i = \overline{f}_i = -\frac{\partial}{\partial \overline{r}_i} V(\overline{r}_i), \tag{2.18}$$

where the forces $\overline{f}_i$ are obtained from the derivative of the potential $V(\overline{r}_i)$.

Once the forces among the atoms in the system, that arise from their interactions, are computed, time must be discretized between consecutive points in the simulation, also known as the simulation time step Δt. Below, the basic steps that have to be followed in order to solve equation 2.18 [61] are shown.

- $\overline{r}(t + \Delta t)$ is expanded in Taylor series:

$$\overline{r}(t + \Delta t) \approx \overline{r}(t) + \Delta t \overline{v}(t) + \frac{\Delta t^2}{2}\overline{a}(t) + \ldots, \tag{2.19}$$

  where $\overline{v}(t)$ is the velocity and $\overline{a}(t)$ the acceleration.

- From eq. 2.19 the value of $\overline{a}(t)$ is worked out and then substituted in Newton's Second Law equation:

$$\overline{F} = m\overline{a}(t) = \frac{2m}{\Delta t^2}\left\{\overline{r}(t + \Delta t) - \overline{r}(t) - \Delta t \overline{v}(t)\right\}. \tag{2.20}$$

- Eq. 2.20 is rearranged:

$$\overline{r}(t + \Delta t) = \overline{r}(t) + \Delta t \overline{v}(t) + \frac{\Delta t^2}{2m}\overline{F}. \tag{2.21}$$

Thereupon, given the forces, the velocities and the current positions in a system of particles at time t, it is possible to determine the positions at time $t + \Delta t$.

At this point, with the dynamics of the system established, the next step to be considered is that the dynamics must portray a process of true interest. One of the most common problems in MD is to consider the system immersed in a thermal bath, implying the need of a thermotsat and a way to establish its temperature T.

From the equipartition theorem we have that for each degree of freedom a value of $\frac{k_B T}{2}$ is assigned,

$$E = \frac{1}{2}N k_B T = \frac{1}{2}\sum_i m_i \langle \overline{v}_i \rangle^2, \tag{2.22}$$

where k_B is the Boltzmann constant. Then, the main role of the thermostat is to exchange heat with the system. For example, if one wants to perform an MD simulation at constant

temperature (NVT ensemble), the kinetic energy has to be kept constant by scaling the velocity at each time step. However, it appears that the resulting configurations of the velocity scaling approach do not belong to configurations within the canonical ensemble. To overcome this, the Nose-Hoover thermostat can be used [62, 63]. The formulation of the thermostat involves the addition of a degree of freedom s to the Langrangian of the system, thus allowing the total energy of the system to fluctuate while a right choice of the potential for the variable s guarantees that the averages of the static quantities in such method are equal to those in the canonical ensemble [63].

So far we haven't considered the kind of interactions that the atoms in the system will be subjected to. Since the behavior of bulk atoms is not the same as the one observed for atoms located at the surface of a given material, the idea of taking into account boundary constraints arises naturally since it is often desired to discard surface effects and consider that all the atoms interact in the same way. For this purpose periodic boundary conditions are used where there are no real boundaries or they are disregarded. This is attained by surrounding the simulation box with replicas of itself and adopting the minimum image convention [**?**, Rapaport]Fig. 2.2).

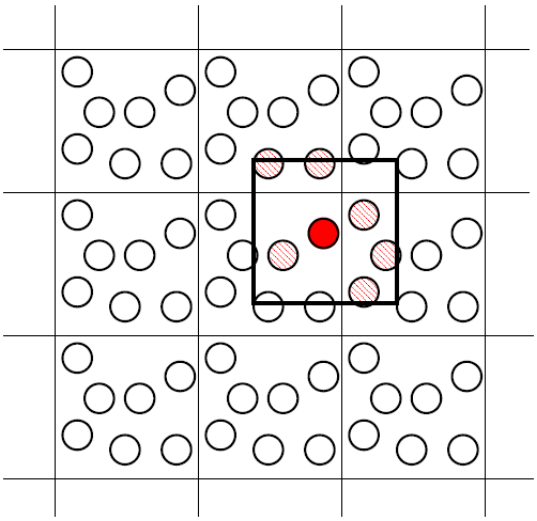

Figure 2.2. Boundary conditions of a 2D simulation box applying the minimum image convention. The solid red circle interacts only with the nearest atom or image in the periodic array (dashed red).

It is important to bear in mind that this is an artificial periodicity and that care must be taken when calculating the properties that depend upon long-range correlations.

Up to now we have mentioned that the potential is a prior quantity to integrate the equations of motion and to calculate a new set of positions after a simulation time step.

These potentials are often built classically by adding and fitting several parameters from experiment in order to replicate certain properties of a material in a simulation. This approach has several advantages and disadvantages. For example, by fitting such parameters some properties are well reproduced, while others are not and the potential used for a given system might not be effective for a different one; however, the number of atoms that can be used in the simulations much larger than those handled by DFT-based methods.

An alternate way to calculate the forces acting on the atoms is using DFT. In this approach, the potential is extracted quantum-mechanically without any adjustable parameter from the DFT computation of the energy of the system. Rigorously speaking, in the DFT formalism there exist parameterizations in the construction of the exchange and correlation functionals, which do not make it an entirely *pure* first-principles framework, rather a semi-empirical one. One of the disadvantages of using an MD+DFT approach, is that the calculations become burdensome and the computer time increases as the third power of N, the number of particles. Nonetheless, first-principles or *ab initio* simulations lead to very accurate results for a huge variety of systems.

Almost 30 years ago, Carr and Parrinello published their work where they mixed both MD and DFT [65]. Its formulation made possible the calculation of the electronic structure of large systems, including disordered ones. By relating the temperature of the system with the average kinetic energies of the ions, it was possible to develop constant temperature, annealing, melting and cooling or quenching processes.

2.3 DMol^3 code

In the present work we used the computational code DMol^3, a built-in module in the Materials Studio Suite [66]. DMol^3 was originally developed by Delley [67] and, as in many different molecular orbital (MO) methods, it builds the charge density from the MOs $\psi_i s$. Since the MOs can be occupied by up or down spin electrons, different charge densities are built for each spin-oriented electron (up or down) so that the sum of both charge densities gives the total charge density.

In DMol^3 the MOs are expanded in terms of a linear combination of atomic orbitals (LCAO), i.e.,

$$\psi_i = \sum_{i\alpha} c_{i\alpha}\chi_\alpha, \tag{2.23}$$

where the atomic orbitals χ_α are known as the atomic bases functions and the $c_{i\alpha}$ are the expansion coefficients of the MOs. Moreover, DMol^3 uses numerical bases which, unlike

the MOs, are not orthonormal [67]. Then, this leads to a reformulation of equation 2.10, which turns into

$$\hat{H}_{\alpha\beta}c_{i\alpha} = \epsilon S_{\alpha\beta}c_{i\alpha}, \tag{2.24}$$

where

$$\hat{H}_{\alpha\beta} = \langle\chi_\alpha(\overline{r}_1)| - \frac{1}{2}\nabla^2 - v'(\overline{r}_1)|\chi_\beta(\overline{r}_1)\rangle, \tag{2.25}$$

$$S_{\alpha\beta} = \langle\chi_\alpha(\overline{r}_1)|\chi_\beta(\overline{r}_1)\rangle. \tag{2.26}$$

Since $\hat{H}$ depends on the coefficients $c_{i\beta}$, eq. 2.24 can be solved iteratively via the flow chart shown schematically in figure 2.3.

Once we have the energy from the self-consistent process an initial velocity is randomly assigned to the atoms, such velocity satisfies a Maxwell-Boltzmann distribution, thus the temperature parameter is included by means of the equipartition theorem.

It is worth-mentioning that DMol^3 is based on the Yoshida-Suzuki [68, 69] algorithm combined with a numerical bases approach. Their approach permits to relax simultaneously all degrees of freedom in the system, which it makes possible to update the forces exerted on the ions at every step, given their spatial coordinates. In other words, the whole MD process is as follows: (a) the initial coordinates are given; (b) the energy of the system is evaluated from the process depicted in figure 2.3; (c) once the energy is obtained, the forces acting on the ions are calculated [**?**]; (d) the ions are displaced in the direction of the forces during a time Δt until they reach their new coordinates and the cycle starts over again.

2.3.1 Electronic and vibrational density of states

2.3.1.1 Electronic density of states (eDOS)

In a crystalline solid periodicity simplifies tremendously the mathematical treatment of the behavior of the electrons. Electrons states are described by Bloch states which, in turn, are related to the symmetry of the lattice by the wave vectors $\overline{k}$ in the reciprocal space. This leads to the band structure $E(\overline{k})$ of the solid.

However, if we have an amorphous solid the story is completely different since the characteristical long-range order of the crystal not longer exist and the periodicity, which once favored the use of Bloch states to represent the electron states, breaks down. In spite of this, there remains a quantity that is equally valid to describe the electronic states

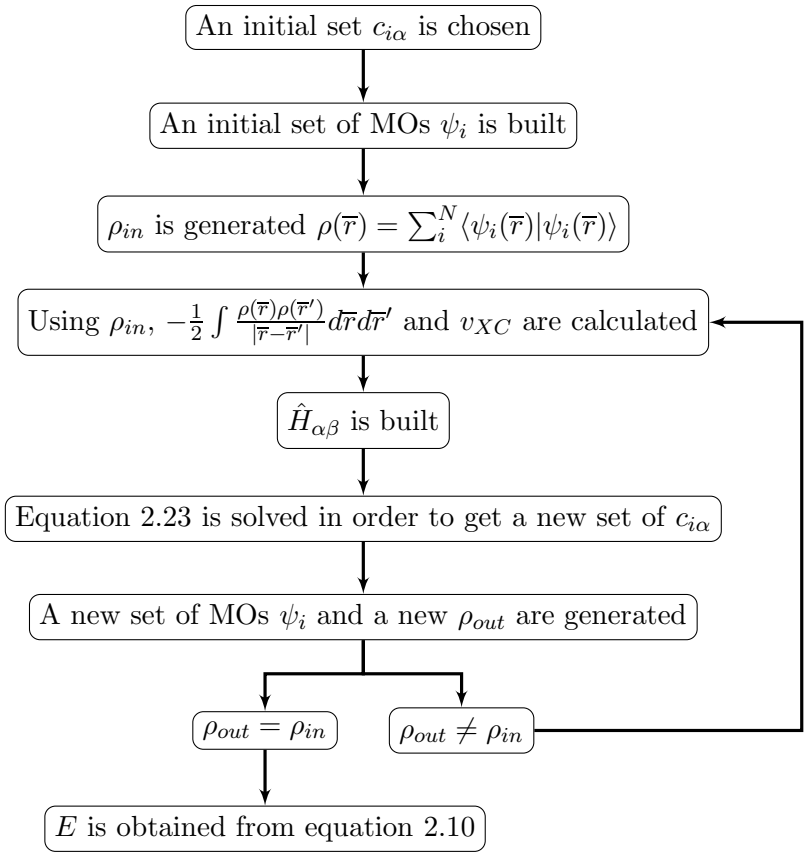

Figure 2.3. Flux diagram of the process to obtain the DFT energy of the system followed by DMol^3.

in both crystalline and amorphous systems; the density of states $\eta(E)$ (eq. 2.27). This quantity is mainly determined by the local ordering.

$$\eta(E) = \frac{1}{V}\sum_n \delta(E - E_n) \Longrightarrow N(E) = \int^E \eta(E')\mathrm{d}E'. \tag{2.27}$$

DMol^3 computes $N(E)$ since the energy of each state is calculated numerically in such a way that if an energy calculation is run, a list that contains the energy and occupation of each level is generated. Therefore, $N(E)$ can be obtained by performing an statistical counting of that list, and that count of states per energy interval represents the eDOS of the system.

2.3.1.2 Vibrational density of states (vDOS)

The atomic vibrations in either a crystalline solid or an amorphous solid manifest in different ways. Despite the structural disparities of both systems, the vibrational behavior of an

amorphous solid is similar to that of a crystal to some extent. They vary in the fact that the selection rules for transitions are relaxed and the sharp peaks of the density of vibrational modes of a crystal are smoothed due to the lack of periodicity upon amorphization [4].

Under certain circumstances, in non-metallic systems the electromagnetic radiation might interact with the vibrational excitations making the characterization of an amorphous system plausible with either infrared or Raman spectroscopy. Inelastic neutron scattering is also feasible since neutrons can gain or lose energy from atomic vibrations. In particular for energies below 10 meV—where more dispersion is present—low energy modes typical of an amorphous structure emerge. This means that short-range order determines the main characteristics of thermal motion as it happens for energies above 10 meV [2].

In order to obtain the vibration frequencies from atomic movement in a solid we can use the classic harmonic approximation. First, the kinetic energy can be written as

$$2T = \sum_{i=1}^{N} m_i \left\{ \left(\frac{d\Delta x_i}{dt} \right)^2 + \left(\frac{d\Delta y_i}{dt} \right)^2 + \left(\frac{d\Delta z_i}{dt} \right)^2 \right\}. \tag{2.28}$$

In the above equation it is appropriate to replace the coordinates $\Delta x_i, \Delta y_i, \Delta z_i$ with mass-weighted displacement coordinates: $q_1 = \sqrt{m_1}\Delta x_1$, $q_2 = \sqrt{m_1}\Delta y_1$, $q_3 = \sqrt{m_1}\Delta z_1$, $q_4 = \sqrt{m_2}\Delta x_2$, $q_5 = \sqrt{m_2}\Delta y_2$, $q_6 = \sqrt{m_2}\Delta z_2$, etc., as well as to change the time derivatives notation in such a way that equation 2.28 reduces to

$$2T = \sum_{i=1}^{3N} \dot{q_i}^2. \tag{2.29}$$

The potential energy is then a function of the displacements and the q_i coordinates [70]. Taking the limit of small displacements, the potential energy V can be written as a power series of such displacements q_i as follows:

$$\begin{aligned} 2V &= 2V_0 + 2\sum_{i=1}^{3N} \left(\frac{\partial V}{\partial q_i} \right)_0 q_i + \sum_{i,j=1}^{3N} \left(\frac{\partial^2 V}{\partial q_i \partial q_j} \right)_0 q_i q_j + O(q_i) \\ &= 2V_0 + 2\sum_{i=1}^{3N} f_i q_i + \sum_{i,j=1}^{3N} f_{ij} q_i q_j + O(q_i). \end{aligned} \tag{2.30}$$

Now, if the zero of energy is taken at the equilibrium configuration ($V_0 = 0$), that is when atoms are in their equilibrium positions $q_i = 0$ for $i = 1, 2, 3, ...$ (energy minimum), then we will have

$$\left(\frac{\partial V}{\partial q_i} \right)_0 = f_i = 0 \qquad i = 1, 2, ..., 3N. \tag{2.31}$$

Furthermore, high-order q terms $O(q_i)$ can be neglected if only small amplitude vibrations are considered:

$$2V = \sum_{i,j=1}^{3N} \left(\frac{\partial^2 V}{\partial q_i q_j} \right)_0 q_i q_j = \sum_{i,j=1}^{3N} f_{ij} q_i q_j, \quad \text{con} \quad f_{ij} = f_{ji}. \tag{2.32}$$

In DMol^3 the harmonic vibrational frequencies are calculated via matrix diagonalization of f_{ij}, since the square roots of its eigenvalues are the frequencies sought. However, since there is no analytical form to calculate the second derivatives of the potential in DMol^3, they are calculated from the first derivatives using a finite differences method. Then, the gradients are calculated in displaced geometries and the second derivatives are obtained numerically. For this purpose two-point differentiation is employed [71]:

$$\frac{\partial^2 E}{\partial q_i q_j} \approx \frac{1}{2\Delta} \left\{ \frac{\partial}{\partial q_i} E(q_j + \Delta) - \frac{\partial}{\partial q_i} E(q_j - \Delta) \right\} \tag{2.33}$$

As in the previous case of the eDOS, at the end of the calculation we will have a list of values representing the normal vibration frequencies of the system, and by statistically counting them, the vDOS can be obtained.

2.4 The Fukui function (FF)

One important feature of porous materials that is worth studying is the chemical reactivity. Unlike non-porous materials, porous ones have a large surface which could be chemically reactive in the presence of an external reagent. Therefore, it is important to analyze how the material behaves along its surface due to electron transfer.

A widely used technique that arose from a "thermo-chemical" application of DFT and that has furthered the knowledge of chemical reactivity of molecules is the Fukui function (FF), which plays the role of a regioselectivity (site reactivity) indicator. The FF measures the local change in the electron density $\rho(\overline{r})$ which occurs as the number of electrons N changes within a fixed molecular configuration [72]. The FF is simply identified as

$$f(\overline{r}) = \left(\frac{\partial \rho(\overline{r})}{\partial N} \right)_{v(\overline{r})} = \left(\frac{\delta \mu}{\delta v(\overline{r})} \right)_N, \tag{2.34}$$

where we can see that it is related to the chemical potential μ which, in turn, relates to the electronegativity χ, the hardness η, and thus to softness $S = \eta^{-1}$ of the system [73]. In other words, the FF will measure how the electronic cloud will redistribute itself in order that the energy reaches a minimum value when a fraction of an electron ϵ is transfered

from or to an N electron system resulting in a $N\pm\epsilon$ electron system. When differentiation takes place and the number of electrons is an integer, the derivative does not exist, rather the left- and right-handed derivatives have to be used [74]. Then the FFs arise as

$$f_N^+(\overline{r}) = \left(\frac{\partial\rho(\overline{r})}{\partial N}\right)^+_{v(\overline{r})} \simeq \rho_{N+1}(\overline{r}) - \rho_N(\overline{r}), \tag{2.35}$$

$$f_N^-(\overline{r}) = \left(\frac{\partial\rho(\overline{r})}{\partial N}\right)^-_{v(\overline{r})} \simeq \rho_N(\overline{r}) - \rho_{N-1}(\overline{r}), \tag{2.36}$$

where $\rho_N(\overline{r})$, $\rho_{N+1}(\overline{r})$, $\rho_{N-1}(\overline{r})$ are the N, $N+1$ and $N-1$ electron system densities correspondingly. This means that when the system accepts electrons they will tend to locate at the sites where the system becomes stabilized, that is, where the value of f_N^+ is large, thus leading to high susceptibility sites of a nucleophilic attack; analogously, high susceptibility sites of an electrophilic attack will be those where the value of f_N^- is large, meaning that those regions in the system will feature less destabilization upon electron removal [75]. It is noteworthy that the FFs are evaluated at the same geometry.

If we recall the frontier molecular orbital theory proposed by Fukui *et al.* [76–78] and try to link it with the Fukui functions, it is appropriate to define a third Fukui function which corresponds to a radical attack as

$$f_N^0(\overline{r}) = \frac{f_N^+(\overline{r}) + f_N^-(\overline{r})}{2}. \tag{2.37}$$

It can be noticed that equation 2.37 is nothing but the average of electrophilic and nucleophilic FFs [72].

By means of the finite difference approximation shown in the above equations, the charge densities are converged to self-consistency for the neutral molecule, the cation and the anion. That is, the FFs are computed using the finite difference approximation and the self-consistent charge densities. Moreover, the FFs are also defined in terms of the atomic charges for an atom α as

$$\begin{aligned} f_N^{+,\alpha} &= q_N^\alpha - q_{N+1}^\alpha, \\ f_N^{-,\alpha} &= q_{N-1}^\alpha - q_N^\alpha. \end{aligned} \tag{2.38}$$

Here, the q_N^α are atomic-centered charges that are computed by means of Mulliken population analysis or by means of numerical integration procedure as Hirshfeld analysis.

In equations 2.38 there might be errors that could affect somewhat the results of the calculation. In the first place, there is an issue regarding the mathematical problem using a value of $\Delta N = 1$. It has been said that for small molecules—when using the DFT

approach—it is convenient to use $\Delta N = \pm 1$, rather than infinitesimal dN changes; in large molecules an approach with a fractional number of electrons should best fit with the problem. Special attention should be paid in using the DFT approach since the exchange-correlation functional has to be chosen carefully, that is to say, a functional that rigorously treats and behaves correctly upon handling fractional number of electrons. Most exchange-correlation functionals that were not designed for this particular scenario usually tend to overstabilize subsytems with fractional numbers of electrons, thus favoring FF delocalization over the molecular system [79].

Instead of using a value of 1 for δN as in conventional FF computations where one full electron is removed or added for the calculation of the charge density of the ions, DMol^3 can use fractional charges which yields faster SCF convergence.

Due to all this theoretical foundations, we decided to use FFs as reactivity indicators for reactions where electron-transfer effects make the dominant energetic contributions and "control" reactivity. However, up to now there have been no experimental or theoretical results where FFs are used beyond the conventional small-molecule systems, apart from the works reported by Santiago [80] and Romero [81], where the reactivity of amorphous porous Ag and amorphous porous C were studied using FFs, respectively.

Chapter 3

Methodology

Now that we have taken a glimpse into the background of metallic amorphous and liquid alloys and the theoretical approach that underlies the work of the present dissertation, the models, methods, parameters and all concerning the simulations will be exposed in the following.

3.1 Supercells

To simulate the amorphization and liquefaction of the Cu-Zr alloys we built the structural models based on a 108-atom cubic copper supercell. To get the desired concentrations, Cu atoms were randomly substituted by Zr atoms followed by a variation of the cell edges in order to obtain the experimental density.

It is noteworthy that the experimental densities of the concentrations Cu_xZr_{100-x} with $x = 64, 50, 36$ were reported by Mattern *et al.* [31]; however, since there are no experimental values for the concentrations $x = 80, 20$, we used the reported values (for $x = 64, 50, 36$) as well as the pure elements' densities to perform a quadratic fit (Fig. 3.1). Moreover, since the calculation of the density of the liquid is not a trivial task, we used the same density values for both amorphous and liquid samples as well as the same initial structural model. In Table 3.1, we report the concentrations with the corresponding densities. Once we had all five supercells we proceeded to the amorphization process.

3.2 Simulation processes

3.2.1 Amorphous and liquids

One of the most common computational processes to amorphize a material is the one that involves the melting from the crystalline phase. Usually the system temperature is raised above the *liquidus* and equilibrated for a certain time. After that, the sample is rapidly cooled down to the undercooled region and again equilibrated at the corresponding temperature. In this work we used a different approach.

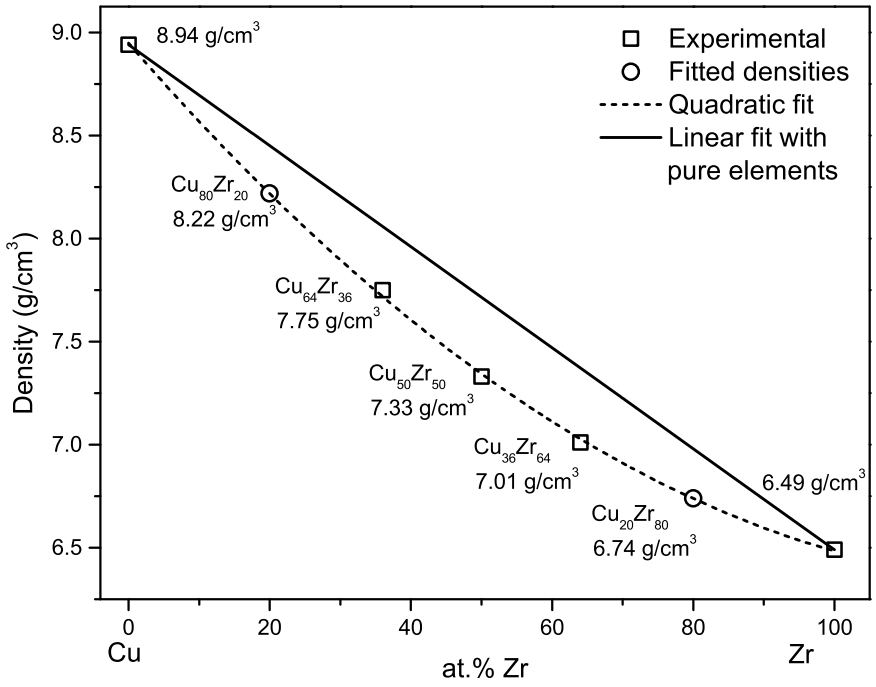

Figure 3.1. Quadratic density fit for $Cu_{80}Zr_{20}$ and $Cu_{20}Zr_{80}$ (circles) based on the experimental density values of pure Cu, Zr and Cu_XZr_{100-X} ($x = 64, 50, 36$) Ref. [31] (squares).

To amorphize the samples we used the *undermelt-quench* process. This process has proven to be very effective in the *ab initio* computer simulation of amorphous semiconducting structures and some metal-metalloid amorphous alloys [38, 82–89]. It involves a linear heating of the supercell from room temperature during 100 simulation steps up to a few kelvins below the *liquidus* [90]. Afterwards, the sample is linearly and rapidly cooled down to a few kelvins above absolute zero. The number of steps that it takes for each sample to be cooled down is defined by the initial heating rate, for the slope of the temperature vs simulation step in the heating stage is the same as in the cooling stage. We present schematically the amorphization process in Fig. 3.2.

As for the liquid samples, we used a similar heating stage as in the *undermelt-quench* process used for amorphous samples, but the maximum temperatures were 100 K above the corresponding *liquidus* [90], assuring the sample to be in the liquid phase. Then the samples were kept at their corresponding temperature for 500 steps. In Table 3.2.1 we present the maximum temperatures for amorphous and liquid samples and the corresponding cooling rates for each amorphized sample.

Sample	Cu atoms	ρ (gcm^{-3})
$Cu_{80}Zr_{20}$	86	8.22
$Cu_{64}Zr_{36}$	69	7.75
$Cu_{50}Zr_{50}$	54	7.33
$Cu_{36}Zr_{64}$	39	7.01
$Cu_{20}Zr_{80}$	22	6.74

Table 3.1. Concentration numbers of Cu atoms and corresponding densities of the Cu-Zr alloy models.

Since the amorphous phase is metastable, the resulting structures were subjected to a geometry optimization process after the thermal stage. This was performed in order to relax the emerging stresses in the atomic configuration and to lower the energy of the supercell, thus reaching the most metastale structure, from which the properties were calculated.

In the case of the liquid samples—contrary to the amorphous case—the geometry optimization was not carried out after the 500-step constant temperature *plateau*, because it would lead to a relaxed structure that would not correspond to a representative structure of the liquid. However, since the computer generation leads to several structures that would produce non-distinguishable PDFs, we averaged the last 15 steps of the *plateau* in order to have a better representation of the liquid [89].

It is worth to mention that for both amorphous and liquid samples we performed two sets of simulations and averaged them afterwards in order to avoid fortuitous results of a single set of simulations.

Sample	T_a (K)	T_l (K)	Cooling rate amor. (K/s)
$Cu_{80}Zr_{20}$	1100	1210	7.4×10^{14}
$Cu_{64}Zr_{36}$	1223	1333	8.6×10^{14}
$Cu_{50}Zr_{50}$	1198	1308	8.4×10^{14}
$Cu_{36}Zr_{64}$	1263	1373	9.0×10^{14}
$Cu_{20}Zr_{80}$	1275	1385	9.2×10^{14}

Table 3.2. Maximum temperatures for amorphous (T_a) and liquid (T_l) samples; cooling rate of the amorphous samples according to the *undermelt-quench* approach.

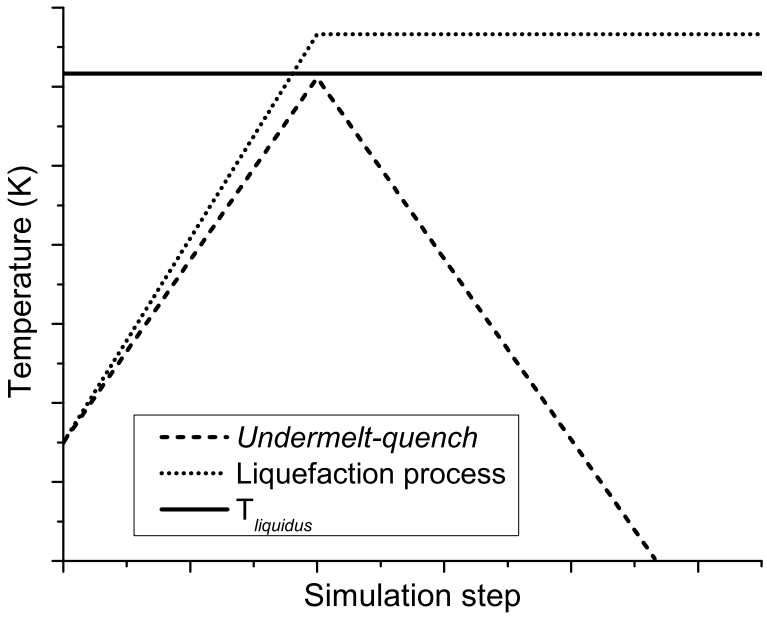

Figure 3.2. Schematic representation of the processes used to amorphize and melt the Cu-Zr alloys.

3.2.2 Porous structures

To generate the amorphous porous structures (BMGF) we chose the representative $Cu_{64}Zr_{36}$ concentration due to the many topological studies it has been subjected to, so that we can compare the structural results upon porosity. Furthermore, we also generated pure amorphous porous copper and zirconium based on the five Cu_XZr_{100-X} amorphous alloys generated with the *undermelt-quench* process. The processes employed to obtain such structures will be discussed in the following sections.

3.2.2.1 Expanding lattice

In the EL method the edge of the cubic supercell is increased and the atomic positions are varied proportionally so that the resulting structure has a larger volume, destabilizing the system. The porosity percentage of the system would depend on the increased size of the original length of the cell; thus, if for example the desired porosity is 50%, then the density of the system should be halved, therefore the relation between the original edge size l_1 and the expanded cell size l_2 would be $l_2 = 2^{1/3}l_1$. The interatomic distances should

be proportionally changed.

This method was applied to both crystalline and amorphous structures to see how the initial configuration influences the resulting amorphous porous structure. Moreover, in order to track the structural evolution of $Cu_{64}Zr_{36}$ glass upon porosity, we simulated the structure with 10% to 50% of porosity. Cell edges, densities along with porosity percentages are reported in Table 3.3.

Porosity	ρ (gcm^{-3})	Edge size (Å)
0%	8.06	11.7848
10%	7.25	12.2050
20%	6.45	12.6937
30%	5.64	13.2715
40%	4.84	13.9712
50%	4.03	14.8467

Table 3.3. Porosity percentage, density and edge size of the supercells subjected to the expanding lattice method (see Fig. 3.3).

We performed two sets of simulations where the difference relies in the initial configuration, i.e., one with the expanded crystalline supercell, and the other with the expanded amorphous supercell. This was done in order to investigate whether a correlation among the initial configuration, pore size and pore shape exists (Fig. 3.3). Along with this, each sample was subjected to a geometry optimization, which compared to an AIMD-plus-GEOPT its computational cost is lower, thus the resulting structures can be obtained more efficiently and more concentrations can be simulated. The simulation parameters regarding these two methods will be covered in Section 3.3.

3.2.2.2 Dealloying

Another approach to generate a porous material (as mentioned in Chapter 1) is the dealloying technique. We simulated chemical dealloying based on the generated Cu_XZr_{100-X} amorphous alloys.

Once the resulting amorphous structures were obtained by the *undermelt-quench* method, either copper or zirconium atoms were removed from the system in order to simulate the dealloying process. Then, the samples were subjected to *ab initio* molecular dynamics at constant room temperature during 250 steps to simulate the conditions that a system undergoes upon chemical attack when one of its atomic constituents is removed. By doing

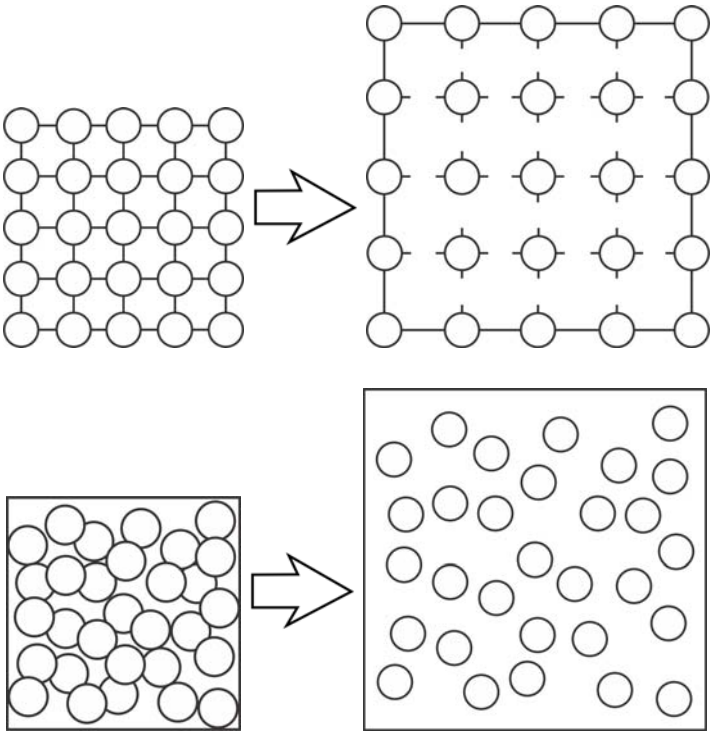

Figure 3.3. Schematic representation of the two initial configurations crystalline and amorphous, upon lattice expansion.

this, both the remaining atomic species and the 'vacancies' are rearranged, which leads to well-defined nano-sized pores and to the so-called *struts* or *backbones*. In Fig. 3.4 the dealloying technique is schematically represented; besides, the characteristics of each sample after the removal of atoms is shown in Table 3.4.

3.3 Simulation parameters

Now that the processes to generate all amorphous, liquid and amorphous porous structures have been addressed, the corresponding parameters for the simulation runs are covered in this section.

In order to computationally generate the samples we used DMol^3 [67], a DFT-based code included in the Materials Studio Suite. We used the local density approximation (LDA) and the exchange-correlation functional due to Perdew and Wang [59]. LDA was used since it is based on the homogeneous electron gas, and can be considered to fit the *homogeneous* environment of electrons in solid metals where directional bonding is not preponderant.

Spin-unrestricted calculations with a double-numerical basis set that include d po-

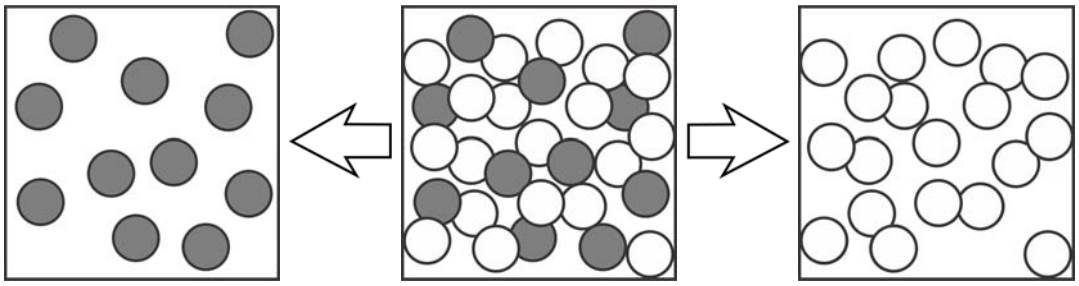

Figure 3.4. Simulated dealloying technique where one of the atomic constituents of the alloy is removed. In the left the atomic species A (white circles) was removed; in the right the atomic species B (grey circles) was removed.

Alloy	ρ_{old}	ap-Cu		ap-Zr	
		ρ	% Por.	ρ	% Por.
$Cu_{80}Zr_{20}$	8.22	6.01	26.8	2.21	73.2
$Cu_{64}Zr_{36}$	7.75	4.29	44.6	3.47	55.4
$Cu_{50}Zr_{50}$	7.33	3.01	58.9	4.32	41.1
$Cu_{36}Zr_{64}$	7.01	1.98	71.8	5.03	28.2
$Cu_{20}Zr_{80}$	6.74	1.02	84.9	5.72	15.1

Table 3.4. Density and porosity percentage of the supercells subjected to the dealloying method. ρ_{old} $[gcm^{-3}]$ is the density of the sample prior to removal of either atomic species.

larization functions (dnd) were employed [67]. In order to optimize the computational resources—inherent to first principles calculations—we used *dspp* (DFT Semi-local Pseudopotentials) which replaces the effects of core electrons by a simple potential adding a certain degree of relativistic effects [67]. Pseudopotentials allow us to reduce CPU time without compromising the quality of the calculations.

Cut-off distances were set at 4.4 Å for Cu and 5.3 Å for Zr, which takes into account up to third neighbor interactions for each atomic species, and an NVT Nosé-Hoover thermostat along with the Verlet velocity integrator algorithm was used. Periodic boundary conditions were also incorporated. Additionally, the orbital occupation was set as thermal smearing at 0.005 Ha.

In the molecular dynamics runs the time step employed was not the default one (DTS), which is proportional to $\sqrt{m_{min}/5}$ where m_{min} is the smallest mass in the system (Cu in this case): 3.57 fs; rather three times the default time step (3DTS) was used, since from previous studies it was shown that it reproduces the experiment better without the presence of errors in the algorithms or colliding atoms that destabilize the structure [**?**, 38, 91].

We must make clear that the process used here to generate the amorphous samples does not mimic the way an amorphous material is prepared or grown experimentally. Moreover, the use of the EL approach is intended to avoid manual carving of the structure to generate the pore; instead we are proposing a method to generate a BMGF whose porous topology would not be biased from the beginning; besides, the method could be transfered to other systems. Therefore, our methodologies have the purpose of generating structures that adequately represent the real ones whenever they exist.

Chapter 4

Amorphous alloys

In this chapter the results obtained for the amorphous alloys are presented and a detailed analysis of the structural, electronic and vibrational properties is made in order to deepen into the possible correlation they might hold.

4.1 Topology

In chapter one, the relevance of the PDFs in the analysis of the structure of a disordered material was discussed. Since it is a very powerful tool, herewith we present the total and partial PDFs of our simulations. For the sake of comparison, we plot all four curves of our generated amorphous strucutres along with the corresponding total or partial PDFs of the crystalline B2 $Cu_{50}Zr_{50}$ concentration (later in this chapter). We chose the B2 $Cu_{50}Zr_{50}$ crystal since it is the only crystalline concentration that counterparts exactly with one of the amorphous concentrations simulated in this work.

From the Cu-Cu partial PDFs (Fig. 4.1a) we see that the shape of the first peak, which is related to the first coordination shell, remains notably the same, and more important, the peaks do not change their position. This means that the local atomic environment around Cu is very similar; i.e., it seems that Cu first neighbors are slightly influenced structurally by the increasing number of zirconium atoms. One expects that the more Zr content present in the alloy, the lesser Cu neighbors around Cu atoms. A more interesting behavior is that between 3 and 4 Å (between first and second coordination shells), a small bump appears and becomes more prominent as the alloys become richer in zirconium content. We think that this is related to the difference in atomic sizes; lets say, the size of the atoms due to covalent radius. When Zr is added, the local geometry rearranges in order to let the Zr atoms be closed together near the crystalline equilibrium positions (3.18 Å). This reordering pushes the smaller Cu atoms far away to larger distances between the first and second coordination shells.

This behavior, in turn, affects the second coordination sphere, which can be seen in the PDFs in the range between 4 and 6 Å . It is observed that the second peak, besides

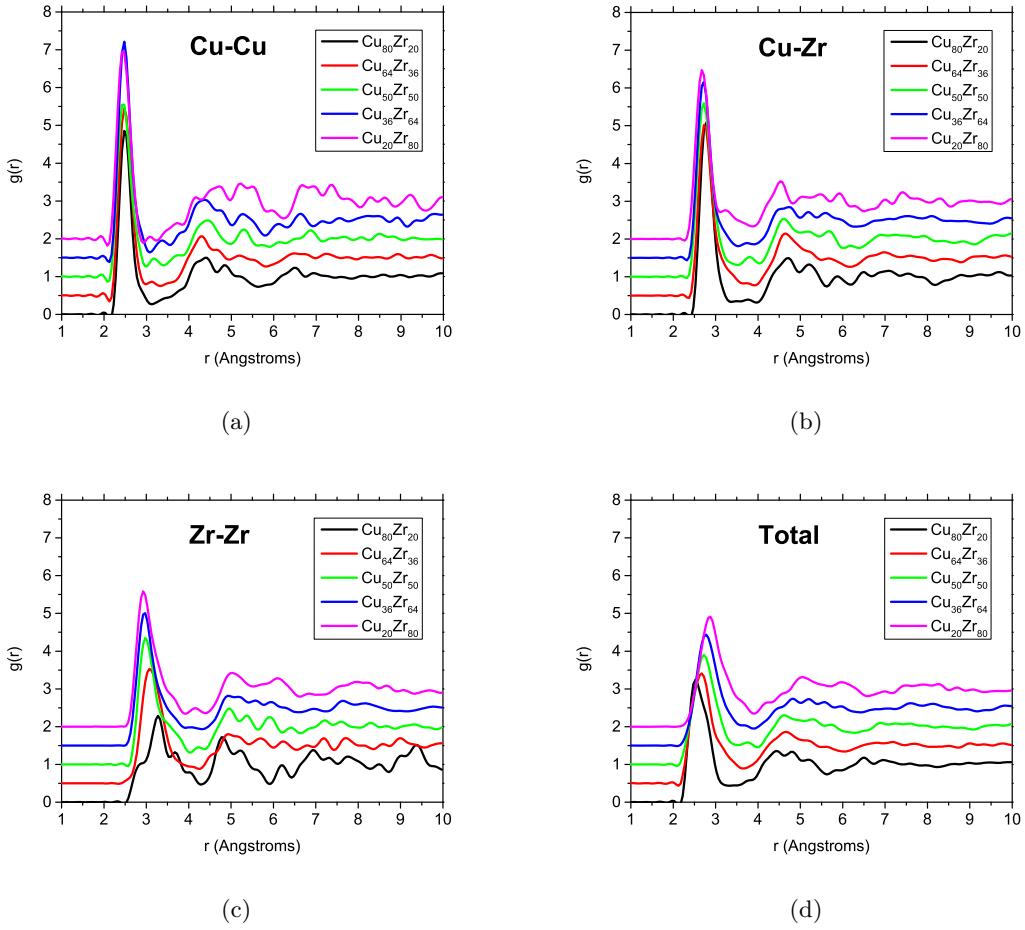

Figure 4.1. Partial and total pair distribution functions of the amorphous Cu_XZr_{100-X} structures. a) Cu-Cu partial; b) Cu-Zr partial; c) Zr-Zr partial; d) Total. The curves were displaced to better exhibit the evolution of the peaks with the concentration.

showing a bimodality, is shifted to larger distances upon Zr content is added.

The Cu-Zr PPDF (Fig. 4.1b) shares similarities with the Cu-Cu PPDF, in the sense that the asymmetry in the first peak and the small bump between the first and second coordination shells are present. The bimodality of the second peak turns into a multimodality, however a main sub peak in the second coordination shell prevails.

As it is noticed in both *i-i* and *j-j* PPDFs, the fluctuations observed at distances larger than 7 Å increase with the amount of the *j* and *i* atoms. This, contrary to the case of the *i-j* and total PDFs where the fluctuations are minimal due to the homogeneous environment. It is worth mentioning that in the Zr-Zr PPDF (Fig. 4.1c) two main features are noticed: a) a displacement to short distances of the asymmetrical first peak; and b) the bimodality

which turns into a multimodality for Cu-rich concentrations. Again, the bump between the first and second coordination shells is present.

The first neighbor distance in Zr-Zr tends to lower below the crystalline equilibrium position due to the fact that the increasing number of Cu atoms let Zr atoms move close together. This behavior manifests again in the total PDF (Fig. 4.1d), where the more Cu content is present in the alloy, the closer the atoms tend to be together and *viceversa*. Moreover, this shift does not only manifests in the first peak but in the whole PDF. Due to this structural arrangements, the general behavior of the second peak is to become multimodal rather than bimodal, therefore we think that this has to do with the rather short-range inhomogeneous arrangement of atoms, then suggesting the presence of clustering in the alloys.

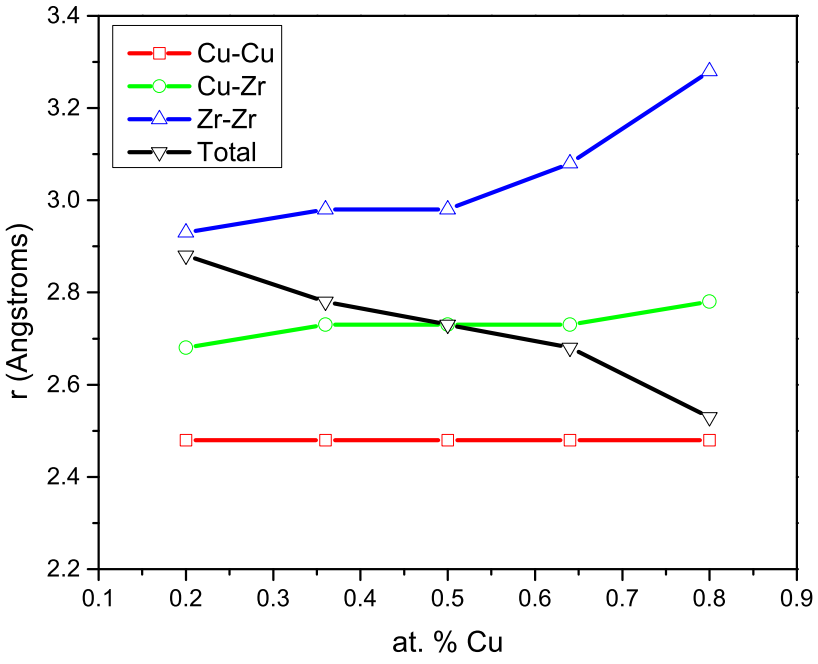

Figure 4.2. Nearest neighbor positions of the amorphous Cu_XZr_{100-X} structures.

In Fig 4.2, the behavior of the first neighbors is depicted. It can be noticed that the total PDF position for the alloy with the least Cu content ($Cu_{20}Zr_{80}$) has the same value as the Zr-Zr PDF with the same conditions. Likewise, the position of the total PDF with the highest Cu content has the same value as the Cu-Cu PDF with highest Cu content, that is, the $Cu_{80}Zr_{20}$ alloy. It also happens that the first neighbor positions for the Cu-Zr

and total PDF coincide. Nevertheless, the behavior is non linear (due to possible clustering which will be addressed later on this chapter).

By using the anaylsis presented in §1.1.1.3 with eq.1.6 and 1.7 the coordination numbers were computed, and are shown in Table 4.1 along with the first neighbor distances. Also in Fig. 4.3 we plot the partial and total coordination numbers in order to exhibit the non linear behavior in the local atomic environment of both Cu and Zr atoms.

at. % Cu	80	64	50	36	20	$83.\overline{3}^{\dagger *}$	$33.\overline{3}^{\dagger 1}$	$33.\overline{3}^{\dagger 2}$
r_{Cu-Cu}	2.48	2.48	2.48	2.48	2.48	2.43	6.03	4.23
r_{Cu-Zr}	2.78	2.73	2.73	2.73	2.68	2.83	2.88	2.78
r_{Zr-Zr}	3.28	3.08	2.98	2.98	2.93	4.88	3.03	3.13
r_{Total}	2.53	2.68	2.73	2.78	2.88	2.43	2.88	2.43
N_{Cu-Cu}	8.7	6.4	4.6	3.6	1.5	8.4	0	0
N_{Cu-Zr}	3.1	5.3	6.1	7.7	8.1	3.2	8.0	8.0
N_{Zr-Cu}	12.2	9.4	6.1	4.3	2.1	16.0	4.0	4.0
N_{Zr-Zr}	3.9	6.0	7.5	8.6	10.5	0	4.4	6.1
N_{Cu}	11.8	11.7	10.7	11.3	9.6	11.6	8.0	8.0
N_{Zr}	16.1	15.4	13.6	12.9	12.6	16.0	8.4	10.1
N_{Total}	12.5	13.0	12.2	11.8	12.0	13.9	10.4	10.9

Table 4.1. First neighbor distances r_{ij} [Å] and coordination numbers N_{ij} of amorphous Cu_XZr_{100-X} structures. †Crystalline values were calculated using the average cut-off radii used in the amorphous: *Ref. [92], [1]Ref. [93], [2]Ref. [94].

It is clear in Fig. 4.3 that there is no concentration-dependence linear behavior of the coordination numbers. Although Cu-Cu and Zr-Zr coordinations are the closest to a linear tendency, there are certain deviations from such trend. Additionally, it can be seen that the total number of neighbors around Cu (Cu-X) and around Zr (Zr-X) show the opposite behavior, i.e., for Cu-rich and Zr-rich concentrations, the coordinations tend to a total number of 12 which is the crystalline coordination of both Cu and Zr. This tendency is also shown for Cu-Cu and Zr-Zr partial coordinations. This is as expected when the amount of an atomic species is reduced far beyond the impurity level until the remaining material becomes pure.

Another interesting feature is the total coordination number. For Zr-rich concentrations it has a value around 12; however, in the Cu-rich side, it is equal or larger than 12.2. It has

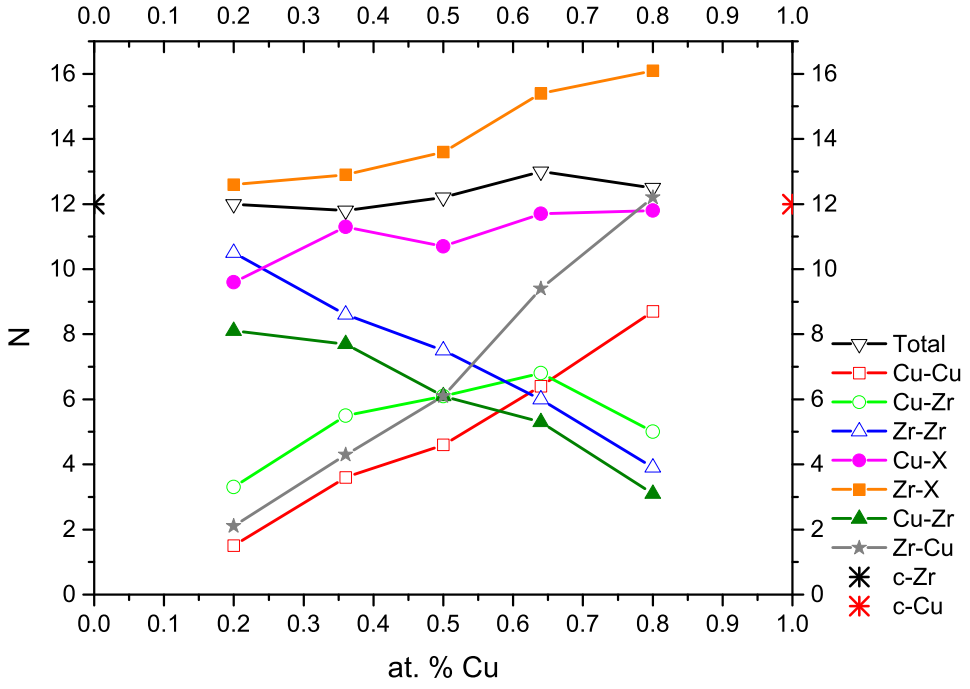

Figure 4.3. Coordination numbers obtained for the amorphous Cu_XZr_{100-X} structures.

often been addressed that the local geometry determines the stability of the amorphous phase in a transition metal-transition metal (TM-TM) alloy. As will be discussed below, the fact that the coordination number is higher than 12 is related to an icosahedron-like short-range ordering (ILSRO). Such geometry acts as a *phase-catalyst* which stabilizes the amorphous structure, thus fostering material growing.

Despite the PDF, and the information that can be extracted from it, provides valuable information about the short-range environment—as mentioned previously—, the data is limited and other tools are required to deepen into the structural analysis. Therefore, we calculated the bond-angle distributions (BADs). In Figs. 4.4 we show total and partial BADs since they give information on all the possible configurations that every triad of atoms can form. To compare between partial BADs, we normalized the curves so that all of them integrate to one.

There are very interesting features that are noteworthy. The fact that there is always a main peak between 50°-60° and a subpeak or bump around 110° in all partial BADs, is a typical behavior of short-range order in amorphous TM-TM alloys [95–97], which suggests a strong presence of ILSRO or other triangulated coordination shells [98, 99], where the

ideal Frank-Kasper (FK) polyhedra *Zn* (with n=13, 14, 15, 16, 17, 18) are built from equilateral triangles, whose angles are 60°. However, due to size disparity of Cu and Zr, such polyhedra are rather distorted, thus the peaks in the BADs are slightly broaden and displaced from the ideal icosahedron positions near 60°, 108° and 116°.

Recently, the short-range order in amorphous $Zr_{80}Pt_{20}$ was discussed *via* angstrom-beam electron diffraction [100]. It was reported that ILSRO is a metastable phase between ideal icosahedron geometry and the fcc crystalline structure. Moreover it is mentioned that in order to retain a dense atomic packing and a low-energy state, the icosahedral order is geometrically distorted and inclined to form a mixed configuration, partially icosahedral and partially fcc. Therefore, if that would be the case in Cu-Zr amorphous alloys, one would expect to find peaks at angles near 90° and 120°; however, apart from a couple of cases, as in the Zr-Zr-Zr partial of the $Cu_{80}Zr_{20}$ alloy, the Zr-Cu-Zr of the $Cu_{64}Zr_{36}$ alloy, the Cu-Cu-Cu of the $Cu_{50}Zr_{50}$ alloy, and Cu-Cu-Zr of the $Cu_{20}Zr_{80}$ alloy, the partial BADs do not exhibit such predominant peaks and neither do the total BADs show so.

Once we find in the BADs that there is no obvious sign of a preferential geometry related to an fcc configuration, to assert that the prevailing SRO geometry is icosahedron-like, a coordination number distribution (CND) analysis was performed by direct counting in the structure the number of nearest neighbors around every atomic species. Moreover, the CND—along with the coordination numbers—provides information on the compositions of the clusters that are present in the amorphous structures.

From Figs. 4.5 it can be observed that in Cu-rich alloys Cu tends to form clusters with 12 neighbors regardless the atomic species it bonds with. Zr, on the other hand, forms clusters with 15 neighbors preferably. In Zr-rich alloys the lack of Cu atoms makes this species to gather into clusters with 10 neighbors mainly, while Zr tends to be surrounded by 12 or 13 atoms. Thus, it is clear that in both Cu and Zr bonding with 12 neighbors is the preferred clustering configuration.

In order to determine the cluster compositions that are formed in our amorphous structures, we analyze Table 4.1, where we can find the following clusters that are formed in this phase, and which are shown in Table 4.2.

With the agreement among the coordination numbers, the BADs and the CNDs we can assert that the preferred local environment present in our amorphous Cu_XZr_{100-X} alloys is the ILSRO, which is more prominent in Cu-centered clusters than in Zr-centered ones. Moreover, a few Cu atoms along with many Zr atoms in Cu-rich alloys tend to form other variety of polyhedra characterized by distorted triangulated coordination shells: FK distorted polyhedra.

By plotting the percentage of atoms with 12 neighbors in every amorphous alloy (Fig.

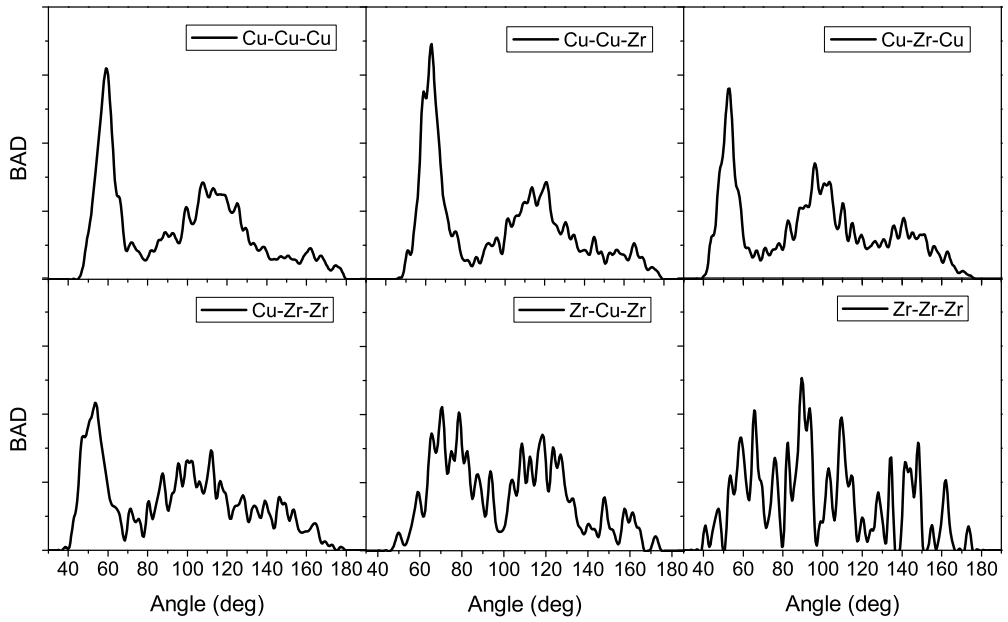

(a)

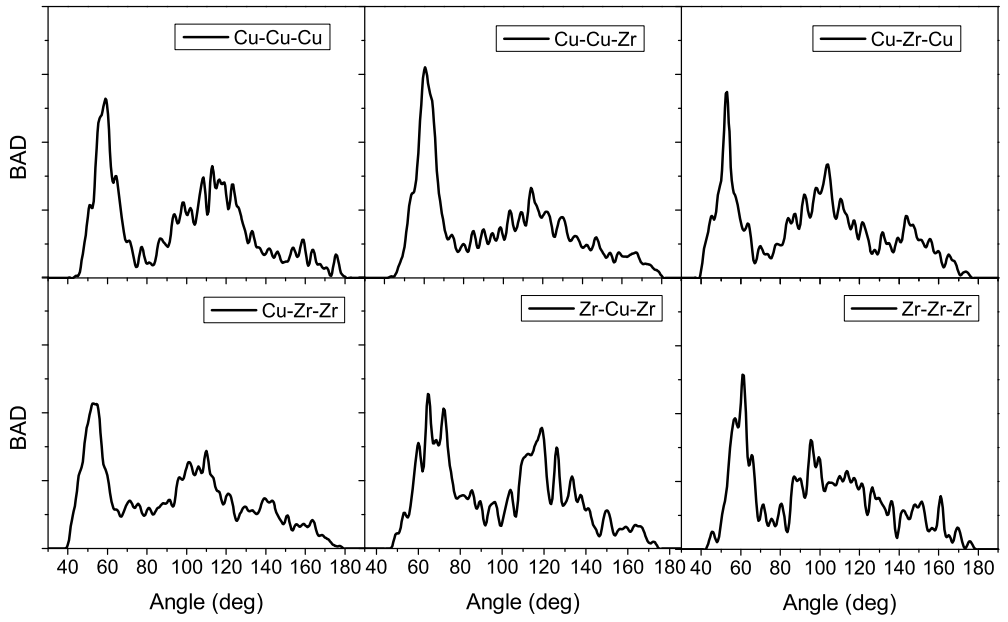

(b)

Figure 4.4. Partial and total bond-angle distribution functions of amorphous Cu_XZr_{100-X} alloys. a) $Cu_{80}Zr_{20}$; b) $Cu_{64}Zr_{36}$; c) $Cu_{50}Zr_{50}$; d) $Cu_{36}Zr_{64}$; e) $Cu_{20}Zr_{80}$; f) total BADs.

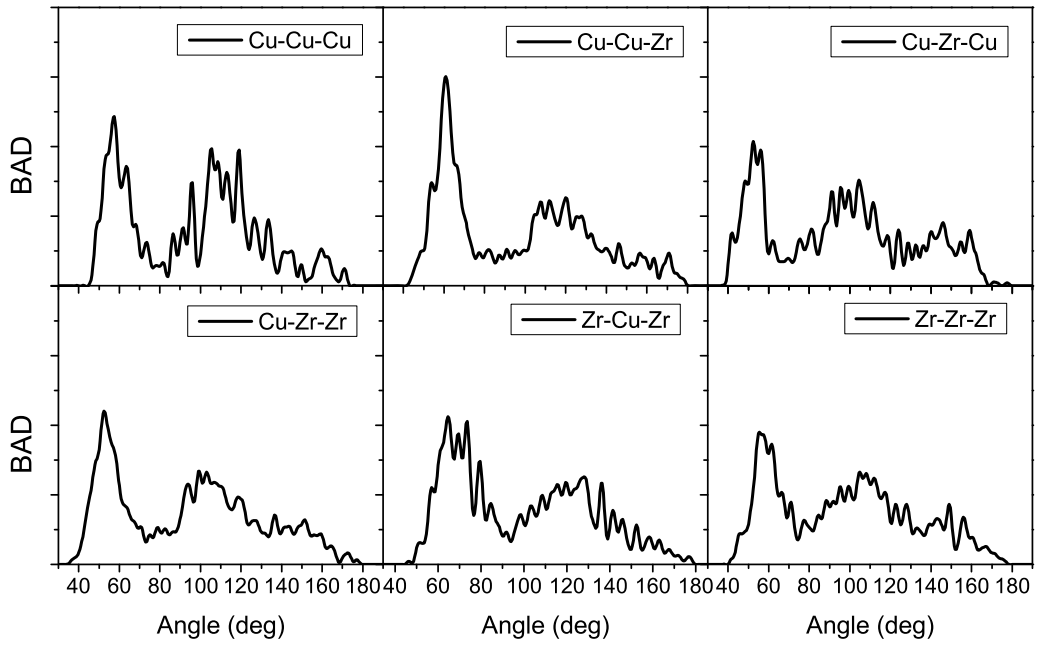

(c)

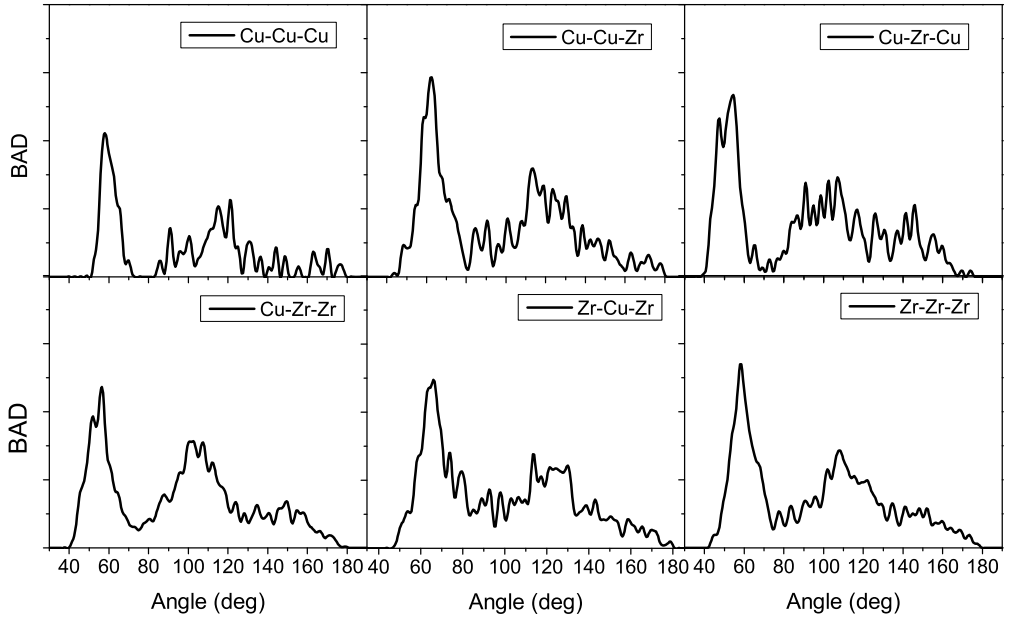

(d)

Figure 4.4. (Cont.) Partial and total bond-angle distribution functions of amorphous $Cu_mathrmXZr_{100-X}$ alloys. a) $Cu_{80}Zr_{20}$; b) $Cu_{64}Zr_{36}$; c) $Cu_{50}Zr_{50}$; d) $Cu_{36}Zr_{64}$; e) $Cu_{20}Zr_{80}$; f) total BADs.

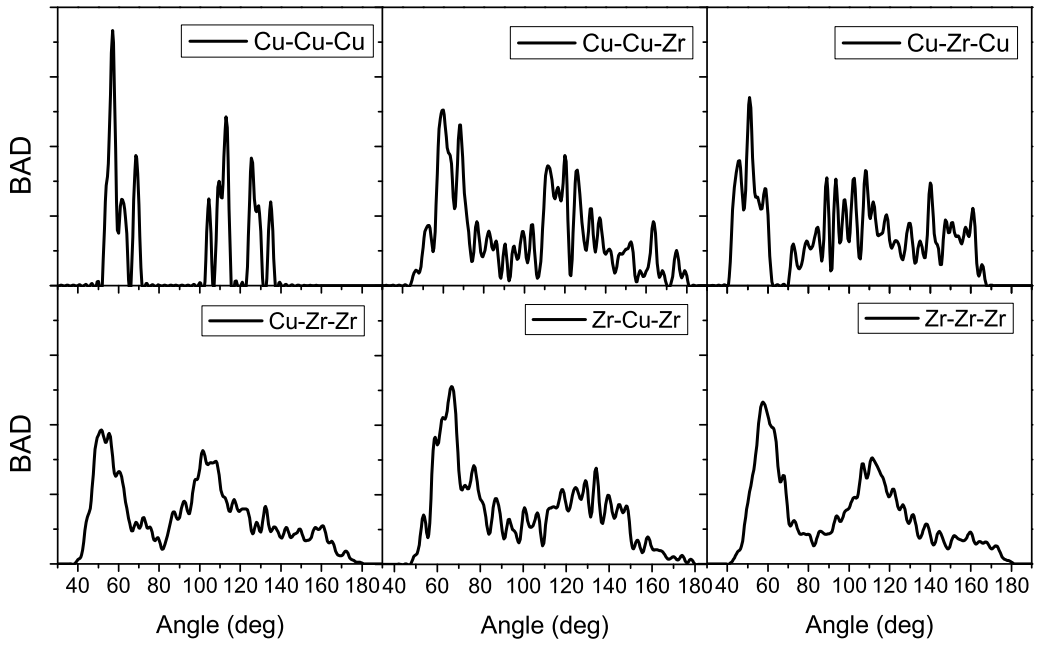

(e)

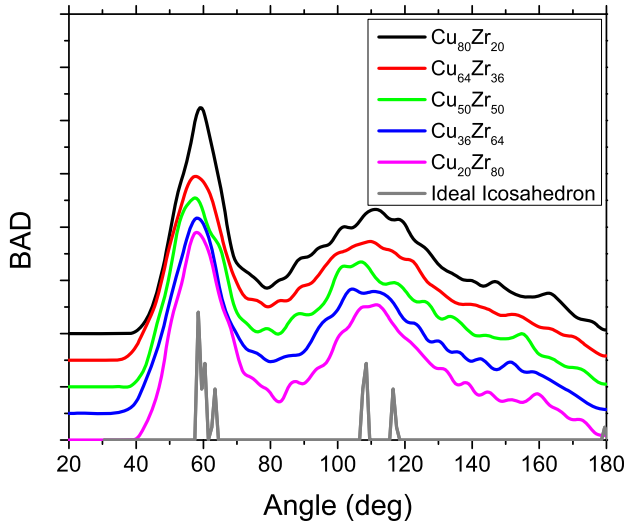

(f)

Figure 4.4. (Cont.) Partial and total bond-angle distribution functions of amorphous Cu_XZr_{100-X} alloys. a) $Cu_{80}Zr_{20}$; b) $Cu_{64}Zr_{36}$; c) $Cu_{50}Zr_{50}$; d) $Cu_{36}Zr_{64}$; e) $Cu_{20}Zr_{80}$; f) total BADs.

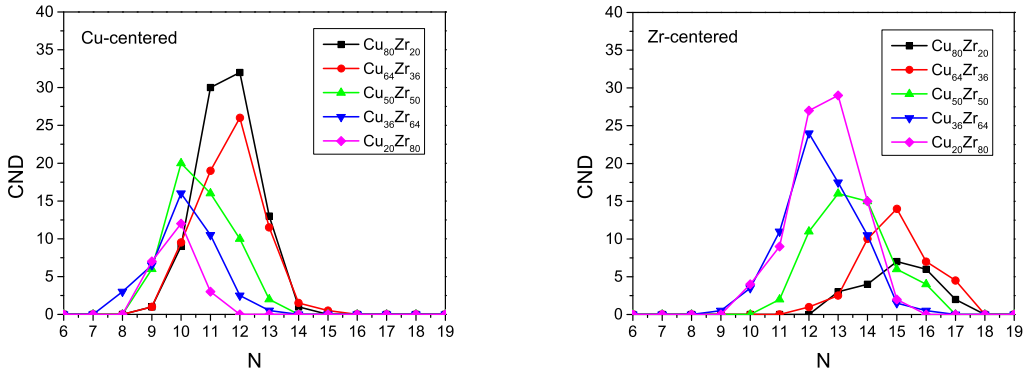

(a) (b)

Figure 4.5. Coordination number distribution for a) copper and b) zirconium in the amorphous Cu_XZr_{100-X} alloys.

	Cu-centered	Zr-centered
$Cu_{80}Zr_{20}$	$Cu_{9.7}Zr_{3.1}$	$Cu_{12.2}Zr_{4.9}$
$Cu_{64}Zr_{36}$	$Cu_{7.4}Zr_{5.3}$	$Cu_{9.4}Zr_{7.0}$
$Cu_{50}Zr_{50}$	$Cu_{5.6}Zr_{6.1}$	$Cu_{6.1}Zr_{8.5}$
$Cu_{36}Zr_{64}$	$Cu_{4.6}Zr_{7.7}$	$Cu_{4.3}Zr_{9.6}$
$Cu_{20}Zr_{80}$	$Cu_{2.5}Zr_{8.1}$	$Cu_{2.1}Zr_{11.5}$

Table 4.2. Cu-centered and Zr-centered average cluster stoichiometry present in our resulting amorphous Cu_XZr_{100-X} alloys.

4.6), we noticed that the $Cu_{50}Zr_{50}$ alloy has 5% lesser atoms bonded with 12 neigbors, which might be due to a phase competition the system undergoes; in other words, we know that our amorphous $Cu_{50}Zr_{50}$ concentration has a B2 stable crystalline counterpart characterized by a bcc configuration whose main angles are at 70° and 109.47°. These two peaks are clearly shown in Fig. 4.4f. First, a bump near 70°, located at 65°, as a right shoulder of the first peak which might occur due to distorsion, and second a shift to the left of the second peak in 107°. Furthermore, this phase competition is found in the total and partial PDFs when a comparison is made with the B2 crystalline phase of $Cu_{50}Zr_{50}$ (c-$Cu_{50}Zr_{50}$), as can be noticed in Fig. 4.7. In the Cu-Cu PPDF the peaks around 3.2 Å 4.5 Å fit with the crystalline case, besides the peaks in the Cu-Zr PPDF around 5.3 Å, 7

Å and 9.5 Å coincide. A noteworthy feature is that the Cu-Zr partial and total PDF of our simulated amorphous $Cu_{50}Zr_{50}$ concide with the first peaks of the crystalline counterpart up to a distance of 5.5 Å approximately.

This should not be thought as an error in the method of generating the amorphous structures, but rather as an sign showing that the system tends to reach the energetic minimum corresponding to the crystalline bcc phase, whose stability range is between 988 K and 1201 K according to the phase diagram of the alloy in Appendix A.

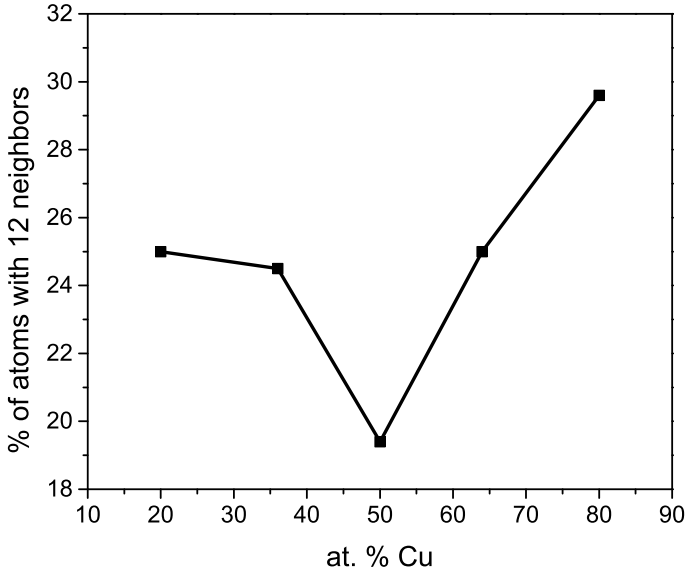

Figure 4.6. Percentage of atoms bonded with 12 neighbors in our resulting Cu_XZr_{100-X} amorphous alloys.

4.1.1 Comparison with experiment

So far, as previously mentioned in §1.4, experimental works regarding amorphous Cu-Zr alloys have been reported. However, only the work (both XRD and ND) from Mattern *et al.* [31] matches three of our simulated concentrations. The most reported PDFs belong to the $Cu_{65}Zr_{35}$/$Cu_{64}Zr_{36}$ alloy [28,29,31]. Moreover, there are cases where the $Cu_{36}Zr_{64}$ concentration or others close to this were reported [31], as well as the $Cu_{50}Zr_{50}$ concentration or simlar ones [31]. The Cu-rich and Zr-rich cases, $Cu_{80}Zr_{20}$ and $Cu_{20}Zr_{80}$ respectively, have only been reported using MD simulations [32,36]. Therefore, these two concentrations would be compared with other theoretical works only, rather than with experiment.

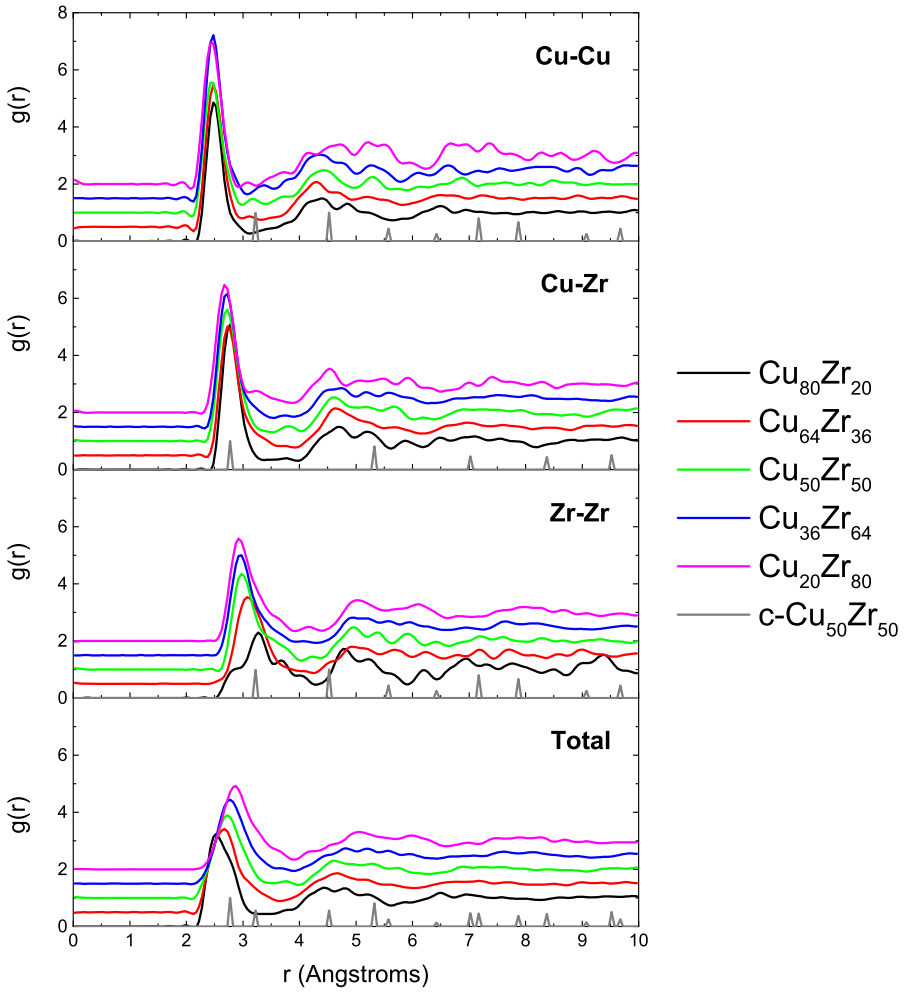

Figure 4.7. Comparison between the partial and total PDFs of our resulting amorphous structures and the stable B2 crystalline phase of $Cu_{50}Zr_{50}$ (c-$Cu_{50}Zr_{50}$).

For a proper comparison with the experiment we weighted our samples for both XRD and ND techniques using the following procedure. First, the total $g(r)$s were obtained as follows:

$$g(r) = w_{Cu-Cu}g(r)_{Cu-Cu} + 2w_{Cu-Zr}g(r)_{Cu-Zr} + w_{Zr-Zr}g(r)_{Zr-Zr}, \tag{4.1}$$

where the neutron dispersion and X-ray diffraction factors are respectively

$$w_{ij}^{ND} = \frac{c_{Cu}c_{Zr}b_{Cu}b_{Zr}}{\langle b_{ND}\rangle^2} \tag{4.2}$$

$$w_{ij}^{XRD} = \frac{c_{Cu}c_{Zr}f(q)_{Cu}f(q)_{Zr}}{\langle f_{XRD}\rangle^2}, \tag{4.3}$$

$g(r)_{Cu-Cu}$, $g(r)_{Cu-Zr}$ and $g(r)_{Zr-Zr}$ are the PPDFs without weight; c_{Cu} and c_{Zr} are the concentrations of copper and zirconium. Moreover $\langle b_{ND}\rangle^2 = (c_{Cu}b_{Cu} + c_{Zr}b_{Zr})^2$ and $\langle f_{XRD}\rangle^2 = (c_{Cu}f(q)_{Cu} + c_{Zr}f(q)_{Zr})^2$, where the f_is are the structure factors for X-rays with $q = 0$, while the b_is are the coherence lengths for neutron dispersion. $q = sen(\theta)/\lambda$, θ is the dispersion angle and λ the wavelength used in the diffraction experiments. Therefore the corresponding values used here were: b_{Cu}=7.72, b_{Zr}=7.16, $f(q = 0)_{Cu}$=29 and $f(q = 0)_{Zr}$=40 according to [101].

In Figs. 4.8a we show the comparison with both experiment and other simulations. From Fig. 4.8a, we notice that our XRD-weighted curve agrees very well with the experimental curves. Although it best matches Mattern and co-workers' results the disparities with Wang's and Mendelev's are a few. For example the case of the first peak where our curve exhibits a slight shift to shorter distances, and a less prominent right shoulder in the same peak, compared to Wang's and Mendelev's. In the second neighbor peak, the shortest subpeak decreases more than the experimental one, and the main subpeak is higher in our case. Again this has to do with the arrangement of atoms in the second coordination sphere, which in turn, is related with the interactions between nearest neighbors as discussed in the previous section.

In the case of the $Cu_{50}Zr_{50}$ alloy we notice a few discrepancies in the first peak mainly, that is to say, the right shoulder in the first peak. In Mattern's curve it is more prominent and it is located at 3.14 Å; however, in our non-smoothed PDF it is located at 3.1 Å, but it does not rise as in the experiment. We think that this difference is due to the contribution of the Zr-Zr PPDF, whose first coordination shell is at 2.98 Å; in other words, it happens that Zr atoms are closer in our simulated amorphous structure than they are in the experimental sample. It also might be due to the competence between crystalline B2

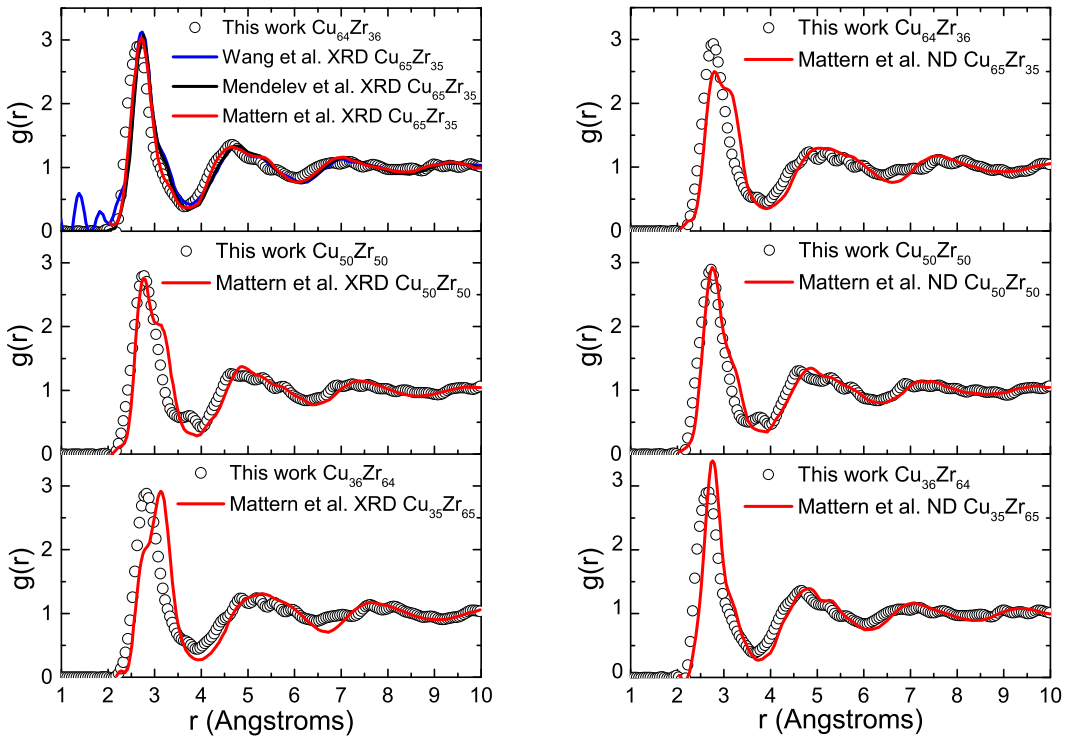

Figure 4.8. Total PDF comparison with the experimental concentrations $Cu_{65}Zr_{35}$, $Cu_{50}Zr_{50}$ and $Cu_{35}Zr_{65}$ of [31]: a) XRD; b) ND; and with the theoretical concentrations $Cu_{80}Zr_{20}$ and $Cu_{20}Zr_{80}$ from [36] c) MD.

phase and the amorphous one, which then favors the location of Zr-Zr atoms closer to the distance of 3 Å.

For the $Cu_{36}Zr_{64}$ concentration the discrepancy in the first peak again is clear. The experimental evolving shoulder prevails now and the main peak which is located near 2.75 Å in the $Cu_{65}Zr_{35}$ and $Cu_{50}Zr_{50}$ alloys now becomes a left shoulder. The position of this shoulder agrees with the first peak of our PDF. Nevertheless, despite the lack of prominency of this peak in our amorphous structure, from Fig. 4.8a it can be seen a clear asymmetry in the first peak and a small shoulder located at 3.08 Å, whereas the experimental main peak is at 3.13 Å. We think this differences arise from XRD weighting, which modifies the height of the peaks but it does not affect the positions.

Comparison with Mattern's ND results is shown in Figs. 4.8b. We see that there is a better agreement than with the XRD experimental curves. However, our $Cu_{64}Zr_{36}$ weighted PDF does not exhibit the right shoulder present in Mattern's. It is also noteworthy the fact that our curves are slightly shifted towards shorter distances. This behavior might be due

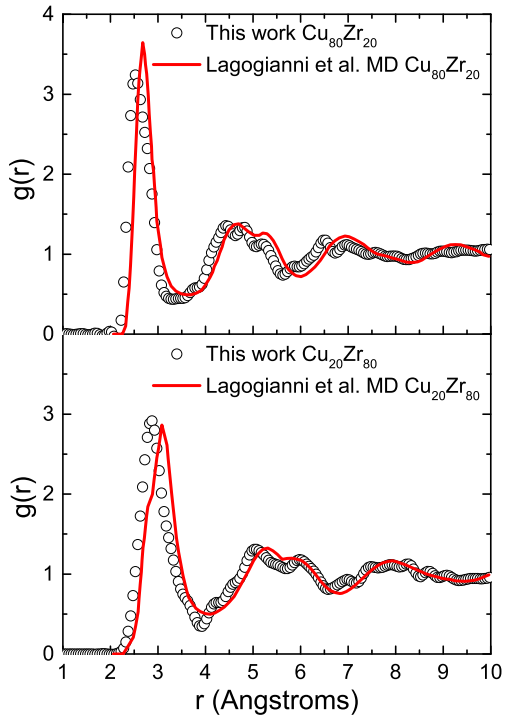

(c)

Figure 4.8. (Cont.) Total PDF comparison with the experimental concentrations $Cu_{65}Zr_{35}$, $Cu_{50}Zr_{50}$ and $Cu_{35}Zr_{65}$ of [31]: a) XRD; b) ND; and with the theoretical concentrations $Cu_{80}Zr_{20}$ and $Cu_{20}Zr_{80}$ from [36] c) MD.

to the fact that we generated an amorphous solid rather than a metallic glass where the initial configuration of the liquid phase, where interatomic distances are somewhat larger, prevails to some extent.

In both XRD and ND comparisons, we didn't notice the bump between the first and second coordination spheres which was mentioned in the previous section. We think that this bump appears in our simulations because during the cooling process, temperature decreases down to near 0 K. This then slows atomic dynamics which affects packing and clustering, thus preventing some atoms to either get closer to the first coordination shell, or to be pushed away to second neighbor distances.

As mentioned before, we compared $Cu_{80}Zr_{80}$ and $Cu_{20}Zr_{80}$ amorphous alloys with the work reported in [36]. From Figs. 4.8c we notice a slight shift to the left as in Figs. 4.8b. Lagogianni and co-workers generated the metallic glass by cooling from the melt to room temperature, thus the structure keeps information from the liquid state upon cooling, which is different than generating an amorphous solid as we do. So we have the same

case as with Mattern and co-workers results for $Cu_{65}Zr_{36}$, $Cu_{50}Zr_{50}$ and $Cu_{35}Zr_{65}$ metallic glasses. Additionaly, the fact that our curves exhibit fluctuations is a consequence of the number of atoms in our samples, an inherent disadvatage of the onerous computational calculations in AIMD. In spite of this, the results agree nicely with either the experiment and other simulations, which suggest that interactions among atoms, and therefore local atomic environment, are well represented.

We also compared the first neighbor distances and coordination numbers. In Table 4.3 we present a comparison with the experimental work of Mattern *et al.* and the simulations of Lagogianni *et al.* and Jakse and Pasturel [32].

Alloy	r_{Cu-Cu}	r_{Cu-Zr}	r_{Zr-Zr}	r_{Tot}	N_{Cu-Cu}	N_{Cu-Zr}	N_{Zr-Cu}	N_{Zr-Zr}	N_{Cu}	N_{Zr}	N_{Tot}
$Cu_{80}Zr_{20}$	2.48	2.73	2.83	2.48	8.7	3.1	12.2	3.9	11.8	16.1	12.5
$Cu_{80}Zr_{20}$ [a]	–	–	–	2.68	–	–	–	–	–	–	–
$Cu_{80}Zr_{20}$ [c]	2.44	2.70	3.26	–	8.9	2.2	8.8	2.3	–	–	–
$Cu_{64}Zr_{36}$	2.48	2.73	2.98	2.73*	6.4	5.3	9.4	6.0	11.7	15.4	13.0
$Cu_{64}Zr_{36}$ [b]	2.63	2.75	3.08	2.75*	7.8	4.6	8.6	6.0	12.5	14.6	13.2
$Cu_{50}Zr_{50}$	2.48	2.73	2.98	2.76*	4.6	6.1	6.1	7.5	10.7	13.6	12.2
$Cu_{50}Zr_{50}$ [b]	2.63	2.79	3.16	2.75*	5.9	6.0	6.0	8.0	11.9	14.0	12.9
$Cu_{36}Zr_{64}$	2.48	2.73	3.08	2.76*	3.6	7.7	4.3	8.6	11.3	12.9	11.8
$Cu_{36}Zr_{64}$ [b]	2.63	2.80	3.16	2.92*	4.6	6.9	3.7	9.4	11.5	13.1	12.5
$Cu_{20}Zr_{80}$	2.53	2.73	3.23	2.83	1.5	8.1	2.1	10.5	9.6	12.6	12.0
$Cu_{20}Zr_{80}$ [a]	–	–	–	3.08	–	–	–	–	–	–	–
$Cu_{28}Zr_{72}$ [c]	2.52	2.74	3.08	–	2.3	8.9	–	10.4	–	–	–

Table 4.3. Comparison of first neighbor distances r_{ij} [$\AA$] and coordination numbers N_{ij}. [a]Ref. [31]; [b]Ref. [36]; [c]Ref. [32]. *These values were calculated as the average from XRD and ND experiments.

Besides the obvious differences pointed out, we think that our resulting amorphous structures agree very well with the available experimental data generated with two different techniques. Then, we demonstrate that a variant of the San Diego method is realiable in the generation of amorphous alloys that resemeble the real ones. It might be added that the application of the original San Diego process is desirable since it envolves quenching stages which could lead to energetically lower and relaxed amorphous metallic structures as have been reported for amorphous semiconducting structures [86].

4.2 Properties

The atomic topology and chemical environment determines the properties of a material as discussed earlier in this work. Now the electronic and vibrational properties in our

generated amorphous alloys are presented. First, the electronic densities of states (eDOS) are reported, which have to do with how electrons behave in the material. In the last part of this section the phonon spectra or vibrational densities of states (vDOS) of each alloy are presented; these are related to the vibrational modes of atoms in every alloy. The two properties, particularly the vDOS, have been widely disregarded in the literature since all efforts have been focused on understading the generating processes that lead to these amazing materials.

4.2.1 eDOS and vDOS

Contrary to the widely reported topological analyses, properties of Cu-Zr alloys such as the electronic ones have been scarcely studied in recent years. Since in our models the number of electrons changes with concentration and a proper comparison of the available states must be done, the curves were not normalized. Instead, we show total and partial eDOS (peDOS) with their own scale to see how each orbital contributes to the eDOS at the Fermi level. In Figs. 4.9 we present the partial eDOS (peDOS) of the amorphous samples.

In Figs. 4.9a-b it can be observed the Cu and Zr partials. It is quite interesting to notice that in whatever atomic species the s orbital has a reduced number of states at the Fermi level. This is more evident in the case of Cu since its electronic configuration is $3d^{10}4s^1$ and Zr has a configuration $4d^2 5s^2$; so the latter contributes with a somewhat larger number of states.

Surprisingly, the p orbital contributes with a larger number of states in both Cu and Zr which increases as the concentration of Cu decreases. Since the occupied subshells in Cu and Zr are both s and d orbitals, the number of p states at the Fermi level could be understood in terms of the hybridization of 4p, 5s and 4d electrons of Zr; so, as the Zr content increases, more and more p orbitals take part in this hybridization mechanism that promotes the number of states. Of course, in transition-metal alloys the hybridization process is not trivial, however it is a possible explanation since several complex geometries are found in our simulated structures (See previous section).

As for the d orbitals, as it was expected, the do not play a major role in the case of Cu for it is a noble metal and has its d band full; contrary to the case of Zr whose d orbitals are barely occupied with electrons. Moreover, it is interesting to analyze the tendency of the eDOS at the Fermi level in both p and d orbitals; that is, as the Zr content increases so does the eDOS, but at 80% of Zr content the eDOS decreases. The low increment of the eDOS in the d orbitals compared to the trend in the p orbitals might be explained as a saturation of the bonds due to the combination of a reduced number of Cu atoms and a high number of Zr atoms in the sample (86 out of 108), so that the available states are

lesser than in the other four alloys.

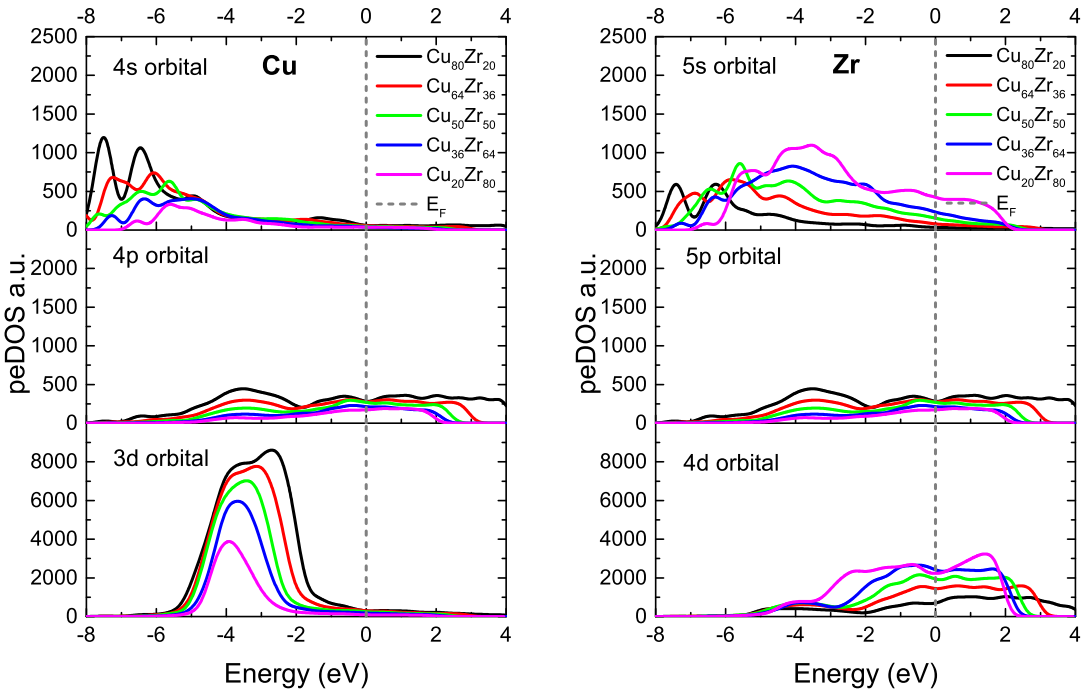

Figure 4.9. Partial eDOS of the amorphous samples. a) Cu partials; b) Zr partials; c) partial eDOS regardless of the atomic species. The Fermi level is indicated as a dashed vertical line.

Now, from Fig. 4.9c it can be noticed that the behavior of the partial eDOS (regardless of the atomic species) are completely influenced by the corresponding peDOS of the larger atomic species present in the alloy. Again the number of states at the Fermi level are dut to p and d orbitals.

Fig. 4.10 shows the total eDOS of all our generated alloys. Notice how the Fermi levels tend to larger energy values as the Zr content increases, besides the shape of the peak evolves from a bimodal profile to a single-peak behavior at about the enegry value of -5 eV as the amount of Cu atoms decreases. Once more, the shape of the $Cu_{80}Zr_{20}$ differs notably from the rest of the alloys, not only in the shape of the deep peak and its position, but in the height. This is a consequence of the d orbital which is mainly responsible for the shape of the total eDOS. In spite of this, the total eDOS of the five alloys exhibits a typical behavior of a transition metal which involves a main peak due to the d orbital, and a flat region somewhat like a plateau for energy values around the Fermi level.

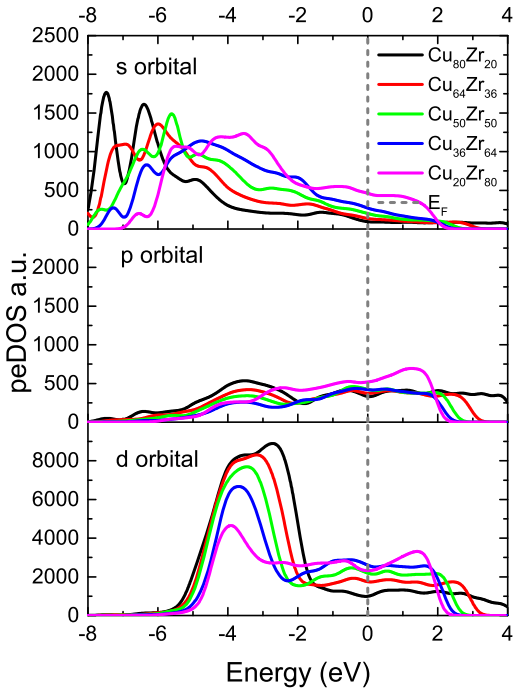

(c)

Figure 4.9. (Cont.) Partial eDOS of the amorphous samples. a) Cu partials; b) Zr partials; c) partial eDOS regardless of the atomic species. The Fermi level is indicated as a dashed vertical line.

Although the trend seems to follow the behavior of a transition metal, a comparison with experiment is necessary to validate our electronic structure calculations. For this purpose, in Figs. 4.11 the comparisons are shown, not only with the available experimental reports, but also with a recent simulational work from Hua *et al.* [47].

It is evident that the eDOS reported in this work do not clearly match the experimental ones. Notice that in Figs. 4.11a-b the reports from Fujiwara and Nguyen agree in the position of the main d-peak ($\sim$ -3 eV); however, they differ in shape and in the value of the eDOS at the Fermi level. Our eDOS match the reported ones of Oelhafen *et al.* in both $Cu_{64}Zr_{36}$ and $Cu_{36}Zr_{64}$ concentrations. In the case of the $Cu_{50}Zr_{50}$ concentration, it can be said that matching can only be observed with the theoretical curve reported in [47].

From this we can argue that, due to differences between the experimental reports in [41] and [42], our results agree with the experiment from Oelhafen *et al.* even though our simulated concentrations $Cu_{64}Zr_{36}$ and $Cu_{36}Zr_{64}$ differ in 6% with respect to the experiment, thus reproducing the electronic properties reasonably.

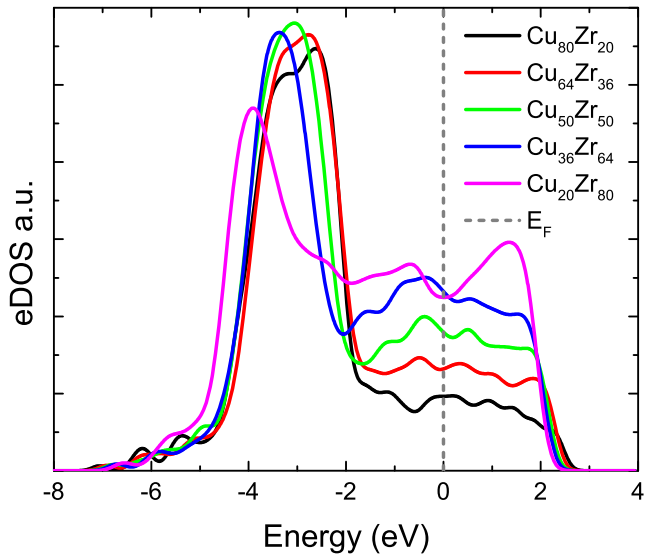

Figure 4.10. Total eDOS of the amorphous samples. The Fermi level is indicated as a dashed vertical line.

To double check the resulting electronic properties, in Fig. 4.12a a comparison of the Fermi levels of our generated amorphous samples and the reported works [41–43, 47] is made. It can be noticed that our results exhibit a linear behavior apart from the $Cu_{20}Zr_{80}$ alloy. This discrepancy has been discussed above.

Although the atomic species are electronically different, the graph suggests that when alloyed, the electronic properties from one concentration to the other evolve homogeneously. The Fermi levels reported in this work are similar to the experimental $Cu_{50}Zr_{50}$ value from Nguyen *et al.*, to the behavior of the two points reported from Oelhafen *et al.* and not quite different from the theoretical report from Hua *et al.*

In addition to this, according to the data available in [90] it is reported that amorphous Cu-Zr alloys exhibit superconductivity at temperatures below 4.5 K. As Zr content is added to the system the superconducting transition temperature (T_t) rises, so when the composition is at. 34% Zr the T_t is 0.3 K all the way to 4.1 K at a compositon of at. 80% Zr. Again, Zr plays a paramount role in the properties that amorphous Cu-Zr alloys.

In Fig. 4.12b we contrast the total eDOS of B2 crystalline $Cu_{50}Zr_{50}$ and the amorphous counterpart. For the sake of comparison both eDOS integrate to 1. First it is worth to mention that in the crystal a clear pseudogap is present at the Fermi level, which completely vanishes upon amorphization. By computing the ratio of the eDOS at the Fermi level of the

amorphous to the crystal we obtained a value of 3.18, which means that in the amorphous phase the material has more than three times the available states for electrons.

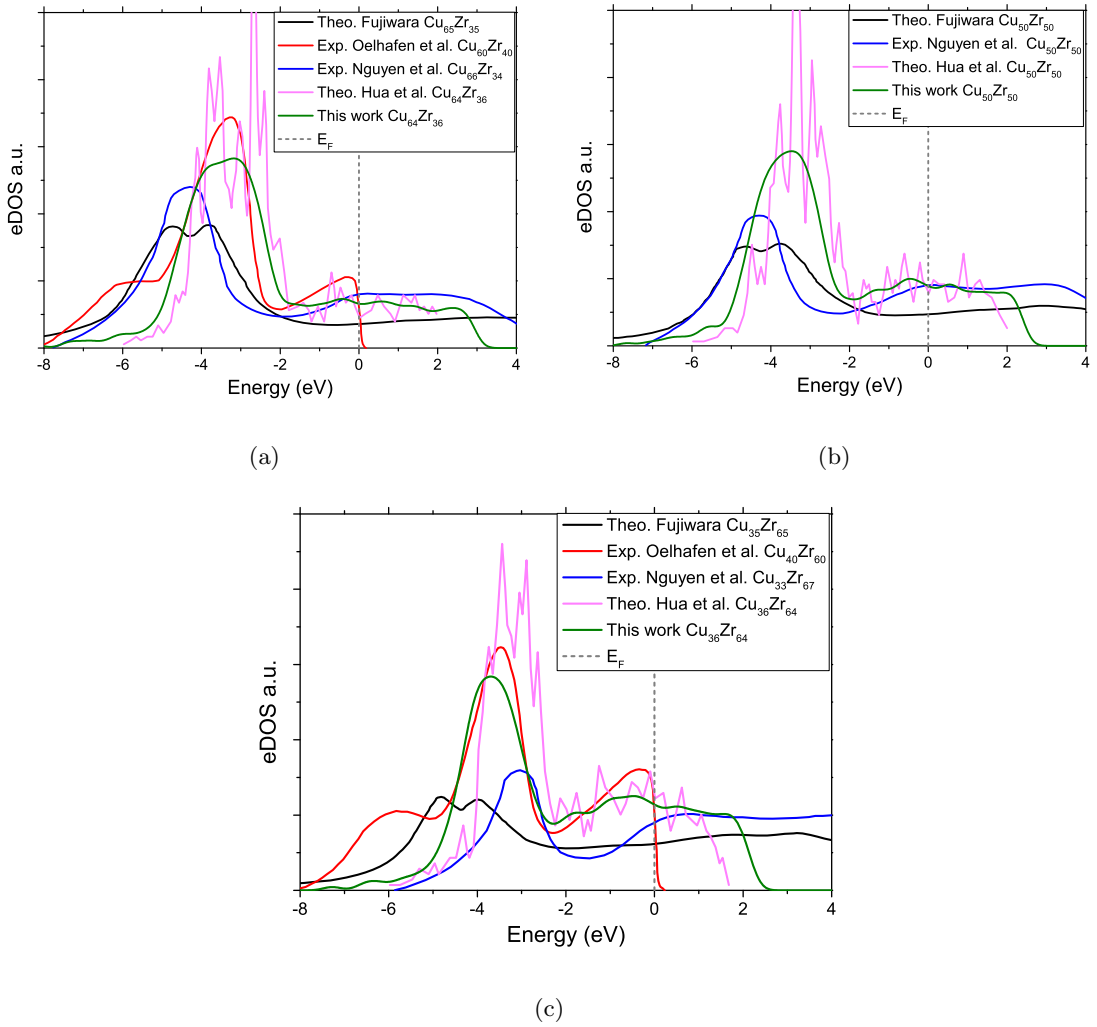

Figure 4.11. Comparison betweeen our eDOS results with reported experimental and theoretical results. There are minor disparities between the experiment [41, 42] and our concentrations for $Cu_{64}Zr_{36}$, $Cu_{50}Zr_{50}$ and $Cu_{36}Zr_{64}$. The Fermi level is indicated as a dashed vertical line.

Invoking the BCS theory to understand the notable disparity in the Fermi levels, we believe that the reason why there are many more electrons states available close to the E_F is that, at the right low temperature (0.7 K in this case according to [90]) electrons will form Cooper pairs fostering the superconductor state. Of course, this explanation is just a rough approximation since it is well-known that BCS has several limitations, i.e., it

does not properly describe superconductivity in alloys. However, the relation of eDOS to the superconducting state has been recently published for the case of amorphous Bismuth in [103].

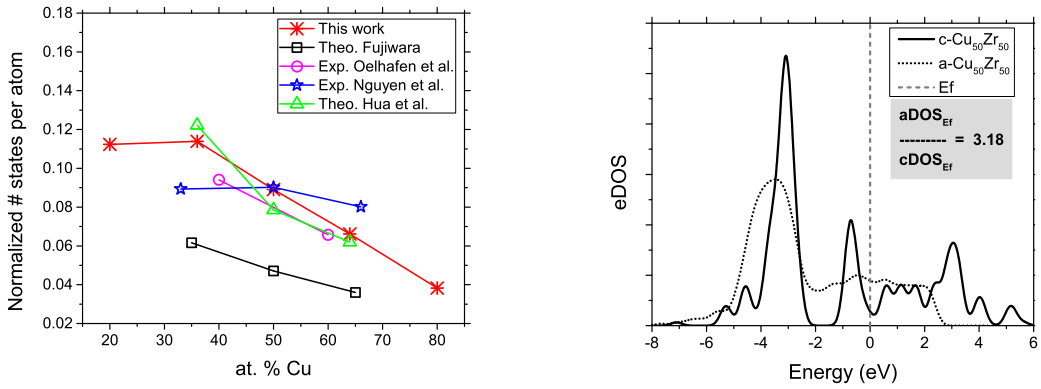

(a) (b)

Figure 4.12. a) Normalized number of states per atom at the Fermi level obtained from the eDOS calculation of our generated amorphous samples compared to experiment [41, 42] and theory [43, 47]; b) eDOS comparison of the stable B2 crystalline $Cu_{50}Zr_{50}$ and our generated amorphous $Cu_{50}Zr_{50}$ amorphous alloy.

As for the vibrational properties, in Fig. 4.13 the phonon spectra are depicted. The same data treatment as in the electronic properties was carried out for frequencies; that is, all curves integrate to 1.

It is interesting to notice how the five spectra exhibit a widespread bimodal spectrum contrary to amorphous semiconducting structures where acoustic and optic bands, or even bandgaps appear [86]. Moreover, a slight peak-position shifting toward low frequencies as Zr content increases stands out; that is, from 18.9 to 16.3 eV. This result is as expected since heavier Zr atoms vibrate at lower frequencies than ligther Cu atoms. For example, if attention is paid to the $Cu_{80}Zr_{20}$ alloy (which is the one with the largest amount of Cu) the height of the left side of the curve is the lowest from the five alloys, which reflects less low frequencies; correspondingly, the right side exhibits the largest amount of high frequencies.

As discussed above, the local atomic environment varies according to atomic content, and although the behavior is not very different it is clear that the arrangement of atoms in several geometries must impact the vibration modes of central atoms within a certain polyhedron (caging). For this reason, the bimodality can be understood in terms of the contributions from each atomic species. In other words, since there is Cu-centered and Zr-centered clustering exhibiting preferential local geometries in each alloy, then there would

be "main" or dominant vibration modes for Cu and Zr which lead to the bimodality in the phonon spectra.

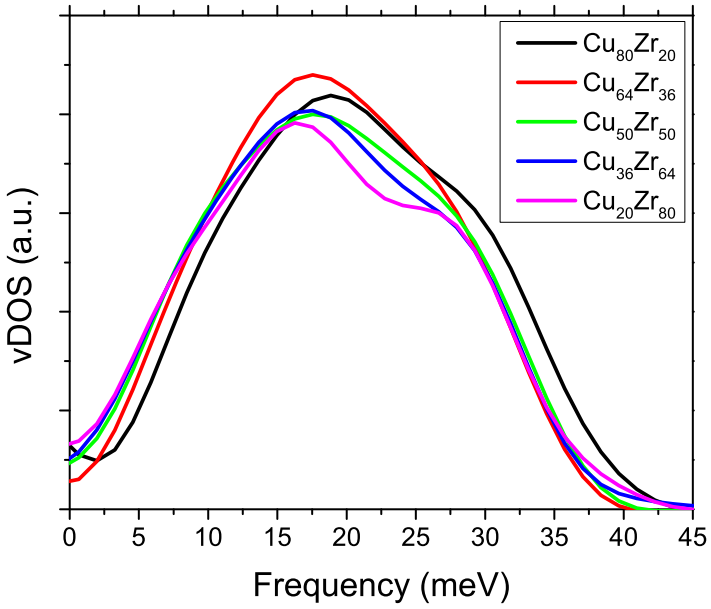

Figure 4.13. Total vDOS of our five generated amorphous samples.

In addition to this, we calculated the vDOS of the $Cu_{50}Zr_{50}$ B2 crystal and we compared it with our amorphous simulated $Cu_{50}Zr_{50}$ in order to analyze how the dominant vibration modes evolve upon amorphization. This comparison is presented in Figs. 4.14 where the most important frequencies are highlighted for both crystalline and amorphous samples. In the case of the amorphous spectrum a Gaussian deconvolution for three peaks was carried out to pinpoint the peak vibration modes.

It is observed that three peaks rule the behavior of the phonon spectrum in the crystalline $Cu_{50}Zr_{50}$. This suggests that the low frequency peak at 10.5 meV is related to the vibration modes of Zr atoms whereas the high frequency peak at 25.1 meV is related to Cu. These two peaks are well defined as a consequence of Cu-Cu, Cu-Zr and Zr-Zr bond lengths. On the other hand, in the amorphous case, these peaks get diffused to even lower or higher frequencies, correspondingly. This happens due to the variation of bond lengths since various distorted polyhedra are formed. For example, although the crystalline nearest neighbor position of Cu is 2.57 Å (3.5% larger that in the amorphous), bond length shortening tend to shift the high frequency peak to the right. For Zr, the bond length in the amophous is 6.3% shorter than in the crystal, this means that the vibration frequency

should increase instead of decreasing as depicted in the curve. However, the formation of several clusters must have to be taken into account (see Table 4.2), and with it, the various bond lengths. Let us remember that in the harmonic approximation the bonds can be visualized as springs attached to atoms.

The interesting peak is the one in the middle. In the crystal this peak might be due to the Cu-Zr bond lengths. In the amorphous counterpart, the peak around 17.2 meV arises due to the Cu-Zr bond length of 2.73 Å. This also explains why this is the lesser shifted peak, with respect to the crystal, with a variation of 13.6% in position.

Finally, if the electronic properties have been widely disregarded, vibration spectrum goes beyond that since the only experimental work is from Suck *et al.* 35 years ago. In this thesis we compare our phonon spectra with early reports found in [48,49] (See Fig. 4.15). Notice that our spectra agrees reasonably well with the experiment; however, the interval from 15 to 25 meV is not well reproduced where the experimental curve is more localized. Nonetheless it is remarkable that we reproduce the low and high frequency regions of the spectrum and also the the bumps.

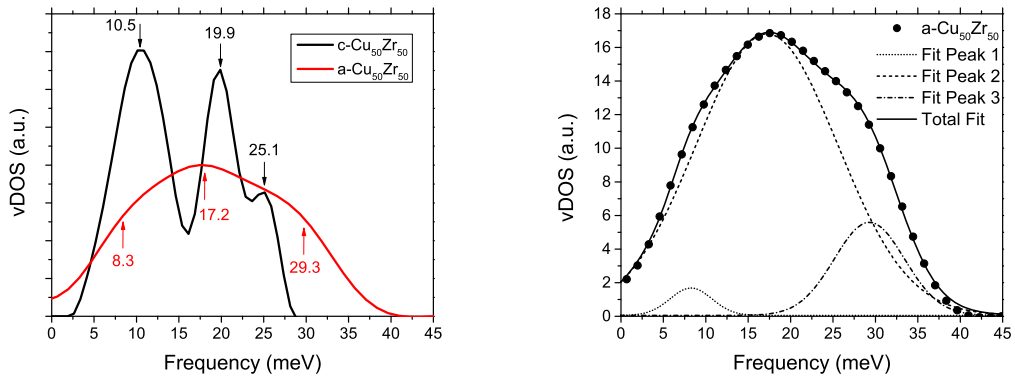

(a) (b)

Figure 4.14. a) Total vDOS of the $Cu_{50}Zr_{50}$ alloy compared to the B2 stable crystal; and b) vDOS deconvolution of the amorphous phonon spectrum. Relevant peaks of each distribution are highlighted.

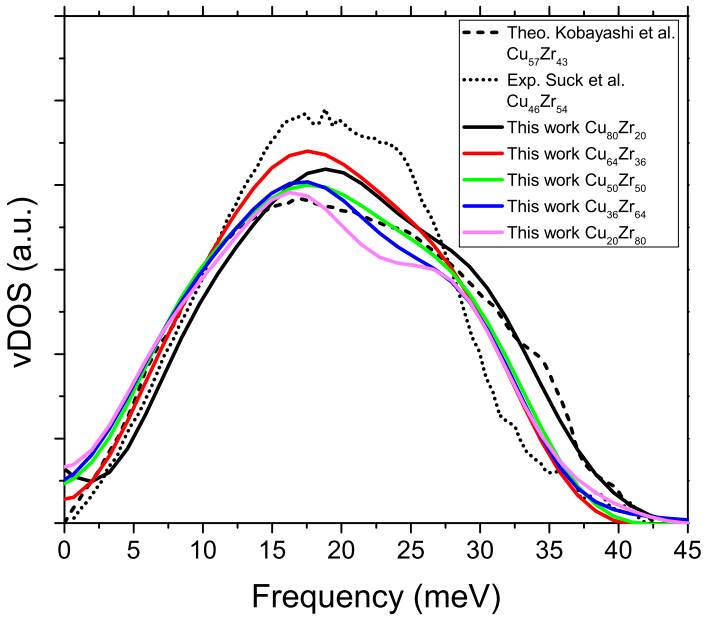

Figure 4.15. Total vDOS of the generated amorphous samples compared to the experimental vDOS in [48] and the modelled vDOS from [49].

Chapter 5

Liquid alloys

Once we have analyzed the topology of our simulated amorphous alloys, we now present also, the structural results of the liquid alloys; an analysis of the topology of such samples is made. At the end of the chapter, the electronic and phonon properties are presented.

5.1 Topology

From Figs. 5.1 the difference with respect to the amorphous PPDFs is evident (Figs. 4.1), since the liquid curves exhibit a lesser number of fluctuations. However, there are remnants which are related to the number of atoms in our simulation cells (108). Once again, a larger number of particles in the simulation would lead to smoother PPDFs; besides, fluctuations in our curves might be related also to the temperature at which the samples were kept; the higher the temperature in the liquid, the more diffuse the peaks will become and the lesser the number of fluctuations there would be. Lets not forget the fact that our simulation samples have a relative small amount of atoms, which also impacts the structure profile, and thus, the fluctuations in the PDFs. A wider and smaller first peak is consistent with the typical behavior of a liquid [3].

It is also interesting to note that if we compare the positions of the first coordination shell with the amorphous case (Table 4.1), there is a slight shift towards shorter distances, which means that neighbors tend to come from 2.48 Å in the amorphous to an average position of 2.43 Å in the liquid, representing 2% of the "initial" distance in the Cu-Cu case. It is almost the same case in the other PPDFs: for the Cu-Zr partial the average distance varies from 2.73 Å to 2.68 Å (1.5%); for the Zr-Zr partial, the reduction is from an average of 3.08 Å to an average of 3.05 Å (1%); and for the total PDF, from 2.72 Å to 2.71 Å (<1%) (Table 5.1, Fig. 5.2).

Since we used the same density for the amorphous and the liquid, a decrement in the first neighbor distances could be related to the fact that atoms have higher mobility due to temperature, thus the local arrangement is modified as a result of this energy difference. This is also evident in the partial and total coordination numbers whose overall tendency

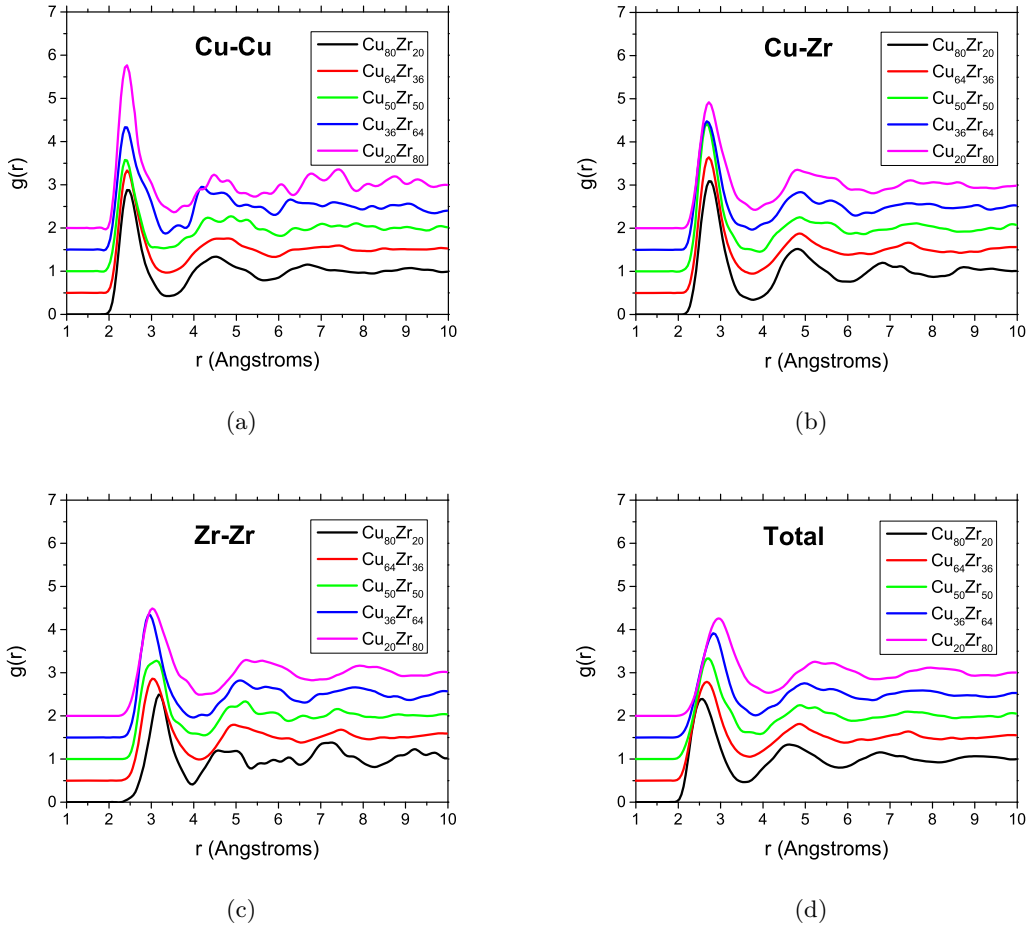

Figure 5.1. Partial and total pair distribution functions of the liquid Cu_XZr_{100-X} structures. a) Cu-Cu partial; b) Cu-Zr partial; c) Zr-Zr partial; d) Total.

is to decrease compared to the amorphous case (Table 5.1).

Another noteworthy aspect is the first neighbor position of Zr-Zr which in the amorphous case exhibits a tendency to increase, while in the liquid it remains almost constant. Perhaps, the fact that all three partial first-neighbor distances are almost constant could be related to a higher diffusion of atomic species in the liquid, which would make it more homogeneous than for the amorphous solid. This homogeneous behavior takes place only to some extent because, as will be discussed below, there is some sort of clustering depending on the concentration.

In the case of the total coordination numbers (Fig. 5.3), they tend to decrease as Zr content increases as mentioned above; again, higher atomic mobility involves a lesser number of nearest neighbors, which in any case implies longer bonds. This means that

the local atomic environment does change, making it temperature-dependent. Therefore, one would expect that the possible clustering in our liquid samples would be somewhat different to the amorphous ones where the atoms bonded to 12 neighbors represent about 25%. However the general behavior is similar to the amorphous case; the most evident differences are shown in the coordination of zirconium (Zr-Zr and Zr-X).

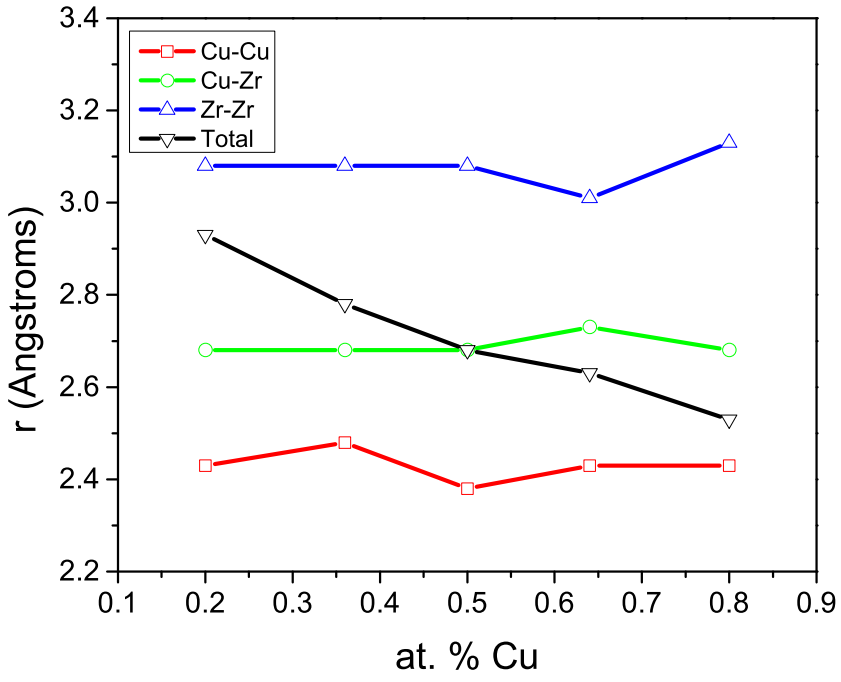

Figure 5.2. Nearest neighbor positions of the liquid Cu_XZr_{100-X} structures.

From Fig. 5.3, it is clear—as expected—that there is no linear behavior in the evolution of the coordination as the content of one atomic species increases. This tendency was present in the amorphous alloys as well, and this is a clear sign that the local atomic environment varies all along the structure, and most important, such variation means that there is clustering. By examining the BADs and the CNDs this statement should become clearer since the analysis of the percentages of coordinated atoms will show the preference of a particular local geometry which depends on the content of Cu and Zr atoms.

In addition, we notice that the tendency of the coordination numbers in the liquid is very similar to the amorphous one, however a prevalent behavior of having less nearest neighbors compared to the amorphous structures is evident. This trend might be related to the temperature difference between the liquid and the amorphous: 110 K in all cases.

at. % Cu	80	64	50	36	20
r_{CuCu}	2.48	2.43	2.38	2.48	2.48
r_{CuZr}	2.78	2.73	2.68	2.68	2.78
r_{ZrZr}	3.23	3.01	3.08	3.08	2.98
r_{Total}	2.53	2.63	2.68	2.78	2.98
N_{CuCu}	8.8	6.1	3.4	3.1	1.9
N_{CuZr}	3.2	5.1	6.5	7.3	8.6
N_{ZrCu}	12.4	9.0	6.5	4.1	2.2
N_{ZrZr}	3.4	6.1	8.2	8.9	10.8
N_{Cu}	12.0	11.2	9.9	10.4	10.4
N_{Zr}	15.7	15.1	14.6	13.0	13.0
N_{Total}	12.7	12.6	12.3	12.1	12.4

Table 5.1. First neighbor distances r_{ij} [Å] and coordination numbers N_{ij} of liquid Cu_XZr_{100-X} structures.

The evolution of the structure in the liquid as a function of the temperature has already been studied. It has been found that the structure of a liquid is strongly related to the temperature at which it is kept, then, if the temperature is near the melting point (within a 50 K range) it is expected that the PDF resembles the amorphous one.

The percentage variations between amorphous and liquid structures obtained from our samples are consistent with the behavior reported for some alloys by Jakse and Pasturel [32]. Nonetheless, a proper comparison cannot be made since they neither reported total PDF, nor the total nearest neighbor positions nor total coordination numbers for their simulated undercooled and liquid samples.

As in the case of the amorphous results, the BADs were calculated for the liquid samples in order to verify and to better understand the local environment present in the generated cells. It is worth mentioning that the BADs were also normalized so that the area under the curve is equal to one, this was done to properly compare them.

We observe surprisingly that all alloys exhibit an icosahedral-like short-range order (ILSRO) profile. From partial BADs (Figs. 5.4a-e) of Cu-rich ($Cu_{80}Zr_{20}$) and Zr-rich ($Cu_{20}Zr_{80}$) alloys a well-defined prominent two-bump structure appears. The first bump appears around 60° and the second one around 115°. This resembles the behavior of the

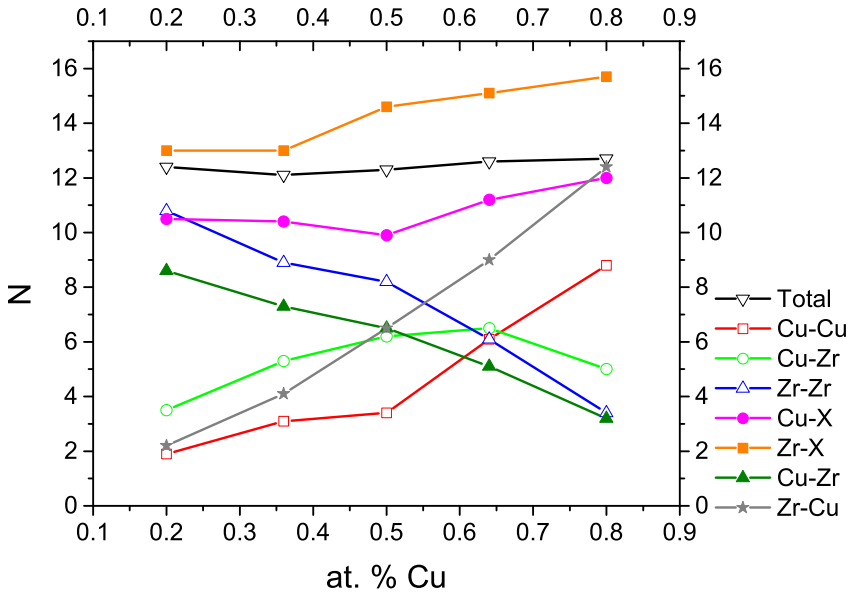

Figure 5.3. Coordination numbers obtained for the liquid Cu_XZr_{100-X} structures.

amorphous samples although the peaks are more diffuse in the liquids; this means that ILSRO geometry is still present in the liquid phase though not to the same degree. Since the structure is temperature-dependent, a rise in the temperature leads to more diffuse BADs, for bonds will tend to loosen as atoms gain more energy from the thermal bath.

When we compare all five total BADs (Fig. 5.4f), ILSRO is clearly the main tendency. What is worth mentioning is how in the main peak (around 60°) Zr content favors the formation of triads with 60° angles, contrary to the case of Cu-rich alloys that exhibit several bumps in the main peak. In the second peak (around 115°) we can notice that $Cu_{64}Zr_{36}$, $Cu_{50}Zr_{50}$ and $Cu_{36}Zr_{64}$ alloys have a more diffuse behavior, which means that at these concentrations ILSRO geometry fades out; it does not disappear completely, though.

The fact that alloys with higher Cu or Zr content have the largest decay between the two main peaks is strongly related to the SRO; this means that Cu-richer and Zr-richer samples tend to form ILSRO preferentially, on the other hand, $Cu_{64}Zr_{36}$, $Cu_{50}Zr_{50}$ and $Cu_{36}Zr_{64}$ concentrations show a slightly more widespread angle distribution. Particularly, the $Cu_{50}Zr_{50}$ alloy has the highest number of angles between the two main peaks. Moreover, this is linked with the amount of 12-coordinated atoms (Fig. 5.7), and is observed that the $Cu_{50}Zr_{50}$ alloy has the lowest amount of atoms with 12 neighbors, as mentioned in §4.

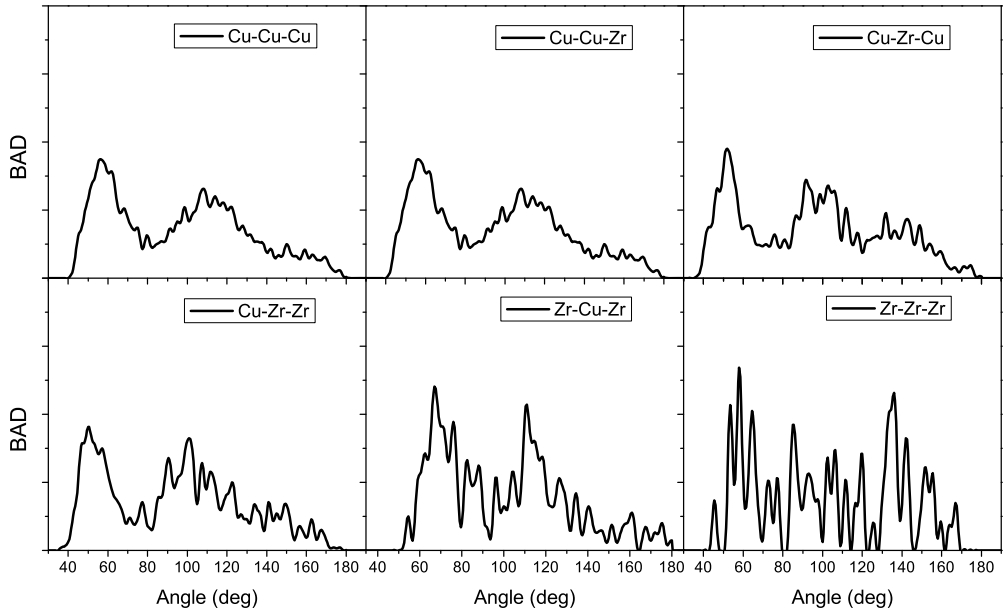

(a)

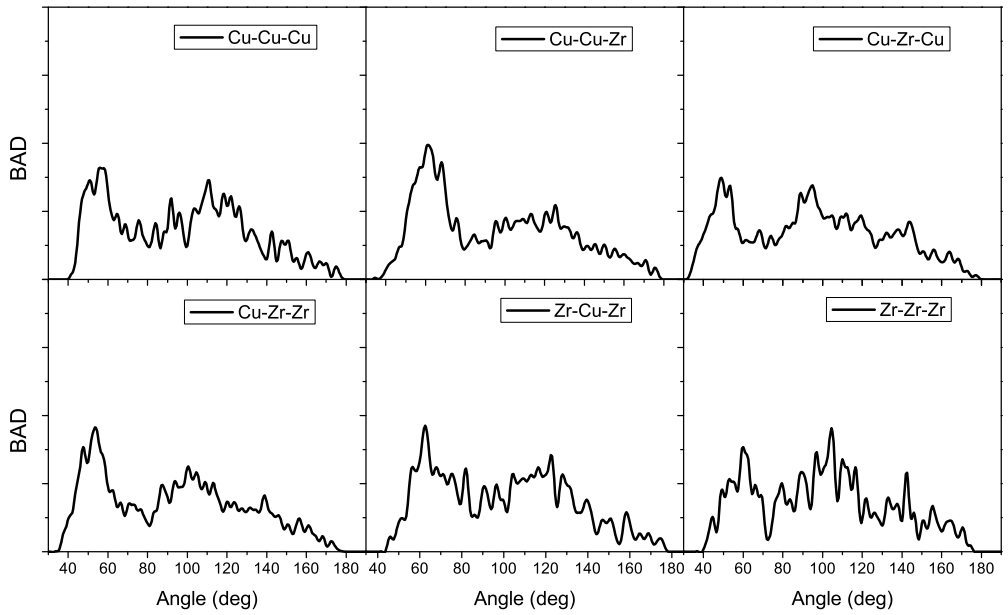

(b)

Figure 5.4. Partial and total bond-angle distribution functions of liquid Cu_XZr_{100-X} alloys. a) $Cu_{80}Zr_{20}$; b) $Cu_{64}Zr_{36}$; c) $Cu_{50}Zr_{50}$; d) $Cu_{36}Zr_{64}$; e) $Cu_{20}Zr_{80}$; f) total BADs.

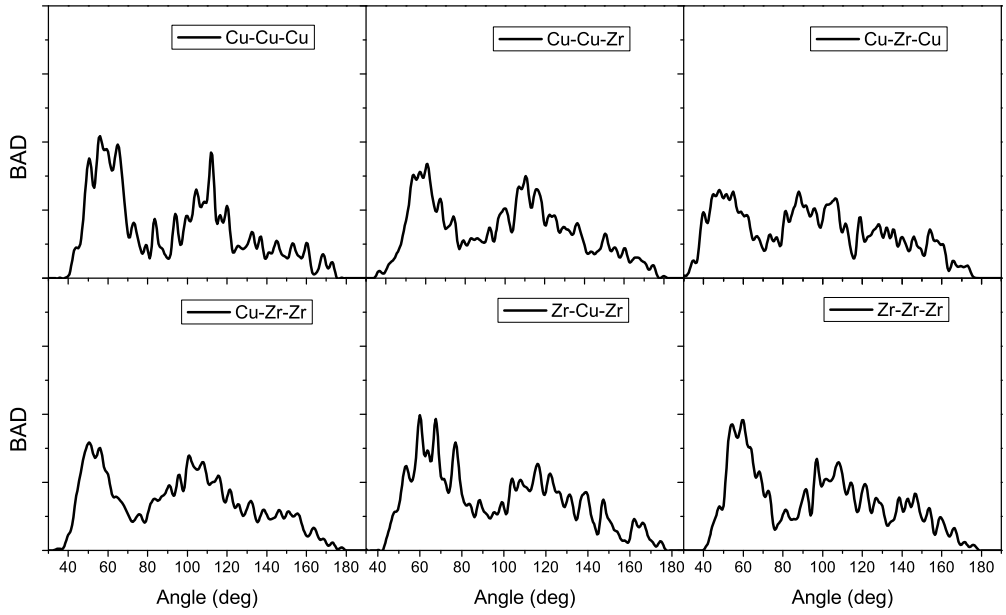

(c)

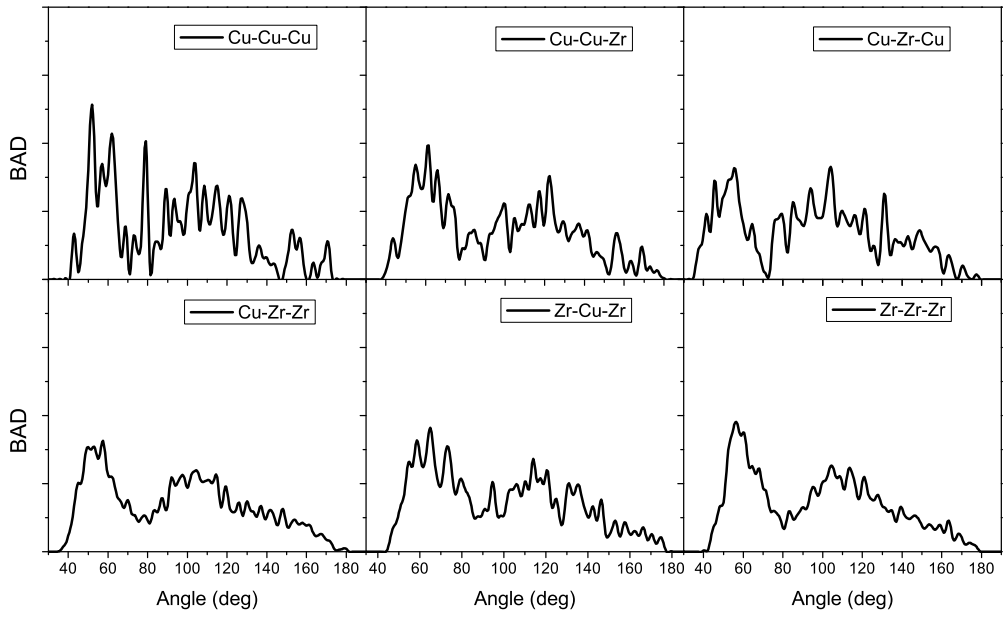

(d)

Figure 5.4. (Cont.) Partial and total bond-angle distribution functions of liquid Cu_XZr_{100-X} alloys. a) $Cu_{80}Zr_{20}$; b) $Cu_{64}Zr_{36}$; c) $Cu_{50}Zr_{50}$; d) $Cu_{36}Zr_{64}$; e) $Cu_{20}Zr_{80}$; f) total BADs.

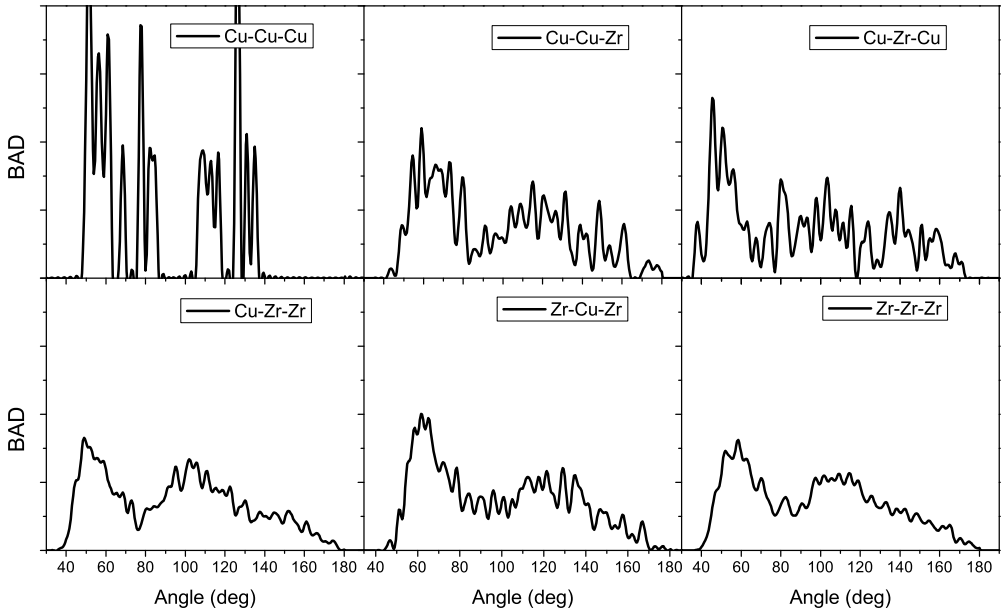

(e)

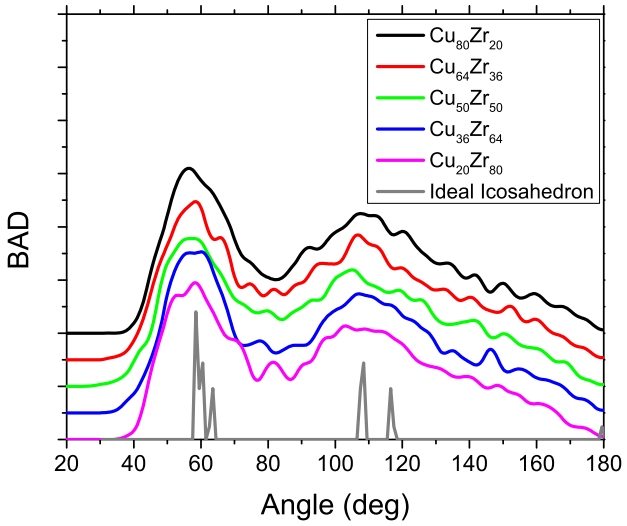

(f)

Figure 5.4. (Cont.) Partial and total bond-angle distribution functions of liquid Cu_XZr_{100-X} alloys. a) $Cu_{80}Zr_{20}$; b) $Cu_{64}Zr_{36}$; c) $Cu_{50}Zr_{50}$; d) $Cu_{36}Zr_{64}$; e) $Cu_{20}Zr_{80}$; f) total BADs.

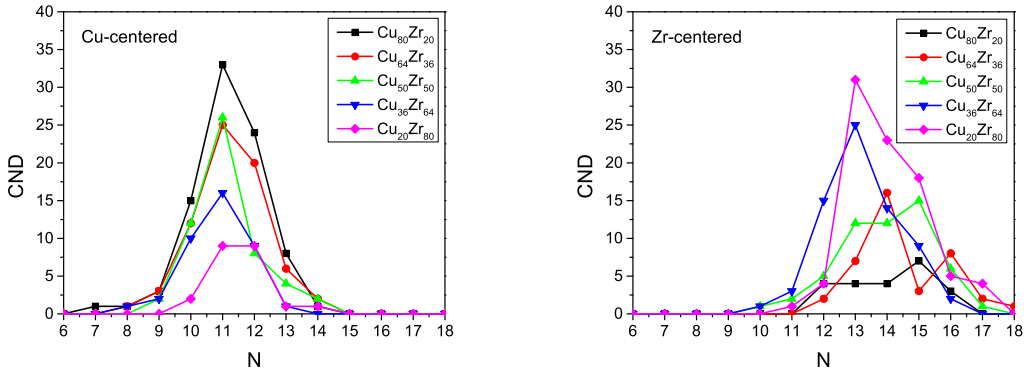

(a) (b)

Figure 5.5. Coordination number distribution for a) copper and b) zirconium in the liquid Cu_XZr_{100-X} alloys.

From Fig. 5.5 we conclude that upon melting Cu atoms tend to be sorrounded mostly by 11 neighbors, contrary to the case of the amorphous phase (Chap. 4) where the coordination varies depending on the concentration. Zr exhibits a similar behavior as in the amorphous case, that is, in general the preferred coordination decreases as zirconium content increases.

To verify the previous idea about clustering, and based on Table 5.1, in Table 5.2 the average clusters in our simulated liquids are presented. As Zr is added, Cu-centered clusters vary from icosahedron-like clustering to groups with less than 12 atoms, while Zr-centered clusters vary from FK polyhedra with more than 16 atoms to groups closer to icosahedron-like clustering. This behavior is very similar to the one observed in the resulting simulated amorphous structures (See Table 4.2).

	Cu-centered	Zr-centered
$Cu_{80}Zr_{20}$	$Cu_{9.8}Zr_{3.2}$	$Cu_{12.4}Zr_{4.4}$
$Cu_{64}Zr_{36}$	$Cu_{7.1}Zr_{5.1}$	$Cu_{9.0}Zr_{7.1}$
$Cu_{50}Zr_{50}$	$Cu_{4.4}Zr_{6.5}$	$Cu_{6.5}Zr_{9.2}$
$Cu_{36}Zr_{64}$	$Cu_{4.1}Zr_{7.3}$	$Cu_{4.1}Zr_{9.9}$
$Cu_{20}Zr_{80}$	$Cu_{2.9}Zr_{8.6}$	$Cu_{2.2}Zr_{11.8}$

Table 5.2. Cu-centered and Zr-centered average cluster stoichiometry present in our resulting liquid Cu_XZr_{100-X} alloys.

In Figs. 5.6 we show a couple of examples of the clusters found in our simulated liquids. They correspond to the Cu-centered Cu_7Zr_6 and Zr-centered Cu_9Zr_6 ideal stoichiometries.

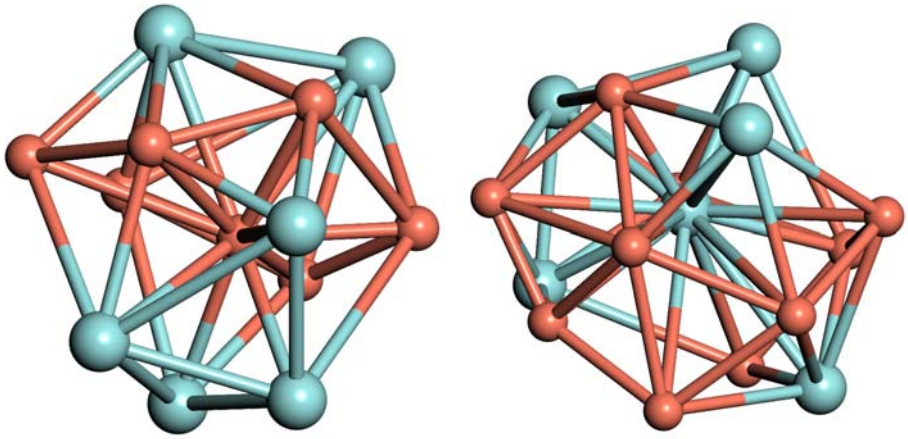

(a) (b)

Figure 5.6. Examples of the clusters found in our simulated liquid structures. Cu atoms are represented as red balls and Zr atoms as blue balls. Extracted from the $Cu_{64}Zr_{36}$ liquid alloy. a) Cu-centered Cu_7Zr_6; b) Zr-centered Cu_9Zr_6.

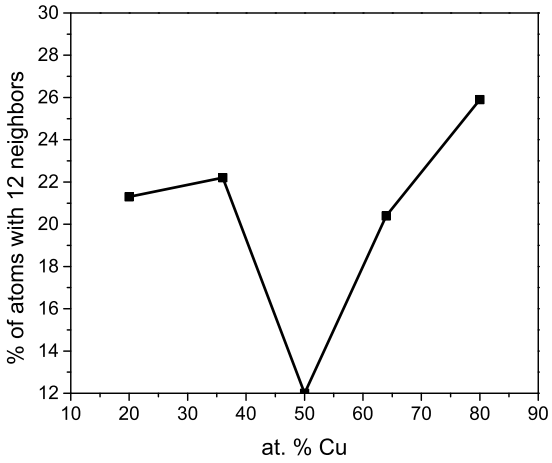

Figure 5.7. Percentage of atoms bonded with 12 neighbors in our resulting Cu_XZr_{100-X} liquid alloys.

It is interesting to compare Figs. 4.6 and 5.7 because the tendency of 12-coordinated atoms in both amorphous and liquid samples is remarkably similar, even for the alloys with the largest amount of Cu atoms. However the amount of 12-coordinated atoms reduces

from amorphous to liquids; this trend can be understood recalling the fact that in liquids bonds tend to loosen due to temperature. Therefore, the coodination agrees very well with the results from Table 5.1, the PDFs, BADs and CNDs.

At this point it is important to contrast our results with other theoretical results, that is, with those of Jakse and Pasturel [32]. In Fig. 5.8 the three PPDFs for the $Cu_{64}Zr_{36}$ alloy are shown. An appropriate comparison with the total PDF is not possible since Jakse and Pasturel did not report it, which is very uncommon for a study based on molecular dynamics. A fairly good agreeement can be observed despite some disparities that appear after the second peak. We believe that Jakse's results are smoother than ours due to the temperature difference (167 K), thus affecting the SRO structure of the liquid, as well as to the number of atoms in the simulation.

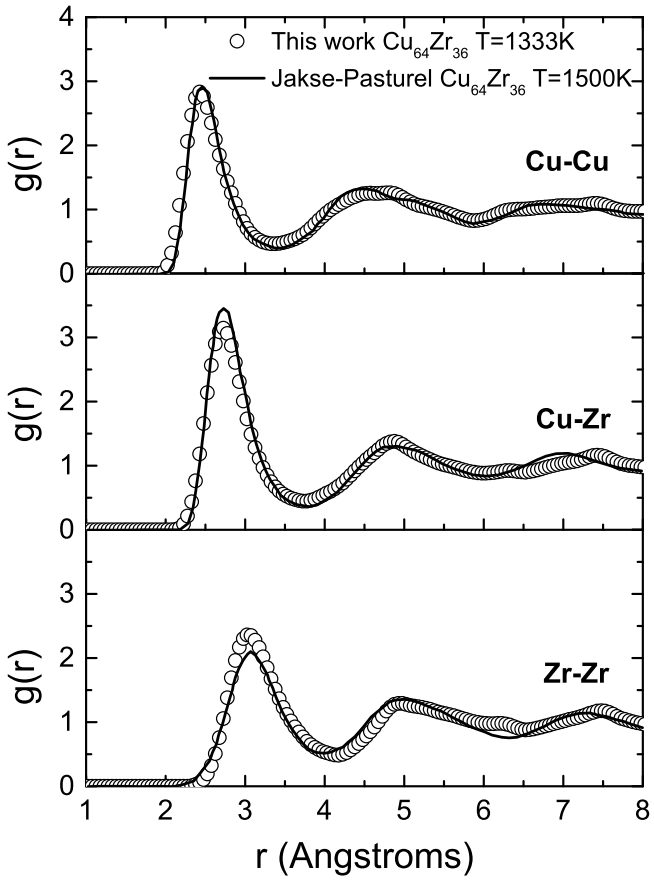

Figure 5.8. PPDF comparison with other *ab initio* simulation reported in [32].

In addition to the comparison made above, we show Bathia-Thornton (BT) partial and total structure factors, which are very useful in the structural analysis of liquids since they provide valuable information regarding the SRO of binary alloys (See Sec. 1.1.1.1). Let us mention the following relevant features:

- The S_{CC} partial is related to fluctuations in the concentration and it oscillates around the value of the corresponding alloy concentration $c_A c_B$ [3]; such values for our Cu_XZr_{100-X} (with $X = 80, 64, 50, 36, 20$) alloys are: 0.16, 0.23, 0.25, 0.23 and 0.16, correspondingly; thus, the small amplitudes of oscillations suggest that the atomic sizes of Cu and Zr in our generated liquid alloys are not very different;

- The S_{NC} partial typically oscillates around zero and vanishes for random mixtures where the local number density of A and B atoms around an A-type atom is the same as that around a B-type one [2, 3], so we observe that in the long-wavelength limit ($q \to 0$) there are peaks in our five alloys which denote number density variations, i.e., chemical SRO arising from the chemical order between Cu and Zr atoms for the height of these peaks is reduced as the Zr content increases; again—as previously discussed—Zr size is very relevant in the topological properties not only of Cu-Zr amorphous alloys, but in the liquids as well, thus we expect that it would also influence importantly other properties as the electronic and vibrational ones;

- Since the S_{NN} partial describes the mean square fluctuations in the particle number, i.e., topological short range order, it is relevant to mention the variation in the positions of the two main peaks as the concentration changes; this differences are related to the evolution of atomic density;

- No significant change in the shape of the S_{NN} is observed apart from the second peak which widens as Zr is removed; the bimodality is still present, indicating the presence of ILSRO as we confirmed in the previous analysis of the BADs.

From the total BT structure factors (Fig. 5.10), as in the S_{NN} partial, the first peak shifting is observed along with the bimodality in the second peak, which also exhibits a widespread profile as Zr decreases. It is important to mention that the observed fluctuations in the long-wavelength limit appear due to the FFT from the PDFs. Later on, a comparison with the available experimental results from Ref. [39] will be made to validate the topology obtained in our simulations.

Now we will discuss an important dynamic property of atoms during the simulation: the mean square displacement, which will let us calculate the diffusion coefficients so that we can better understand the dynamics process in the liquid as a function of the concentration.

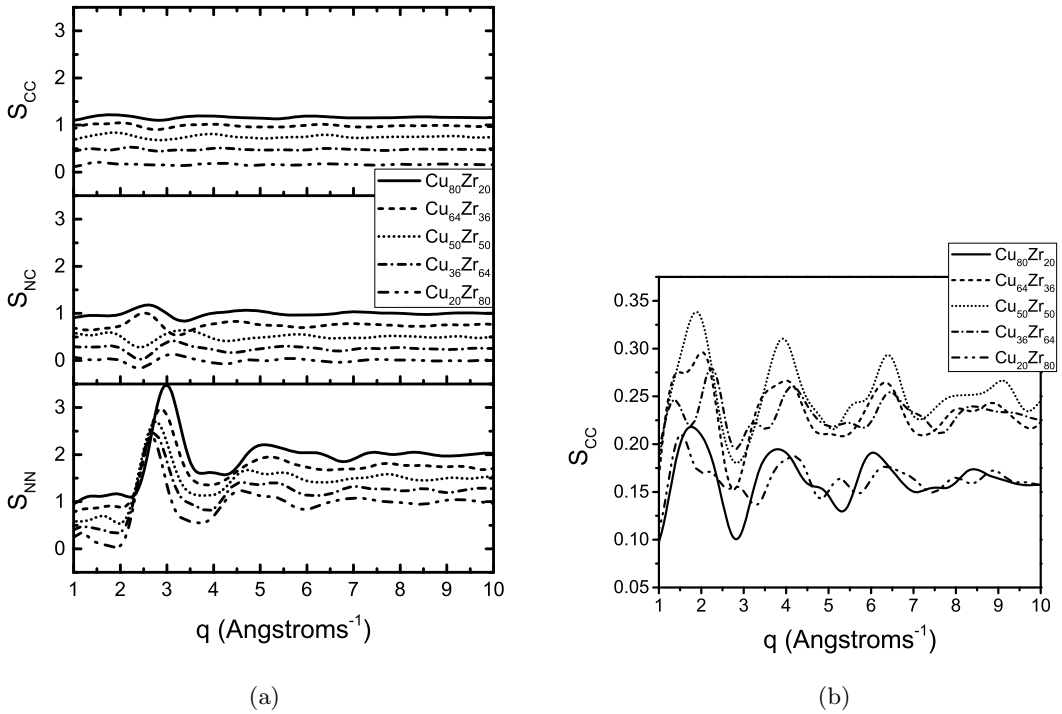

Figure 5.9. Partial Bathia-Thornton structure factors. a) S_{CC}, S_{NC}, and S_{NN}; b) S_{CC} partial structure factor amplification to show how it varies around $c_{AC100-A}$: 0.16, 0.23, 0.25, 0.23 and 0.16 for A= 80, 64, 50, 36 and 20, respectively. Curves were displaced for a better comparison.

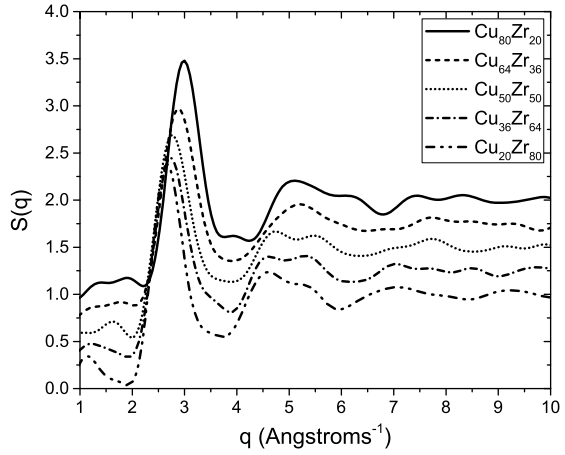

Figure 5.10. Total Bathia-Thornton structure factors of our simulated liquid Cu-Zr alloys. Curves were displaced for a better comparison.

5.1.1 Mean Square Displacement

The mean square displacement (MSD) denotes the dynamical behavior of atoms during the simulation process. By knowing how much every atomic type moves we can better understand the interaction of particles during the stabilization phase in the liquid, as well as how they diffuse all over the material.

In Figs. 5.11 the partial and total MSD are shown. From the partial MSD curves it can be observed how displacement grows as Zr content increases up to the concentration $Cu_{20}Zr_{80}$ where if falls to approximately the value of the $Cu_{64}Zr_{36}$ alloy; this is so for both Cu and Zr. The same trend is present in the total MSD. In general Cu atoms move more than Zr.

It is interesting to note that for the case of the $Cu_{20}Zr_{80}$ alloy, whose MSD drops, up to the first picosecond time of the dynamics, atoms tend to move more that the previous alloy ($Cu_{36}Zr_{64}$); such difference might be related to a caging mechanism that prevents both species from moving may arise as the structure stabilizes in the constant temperature stage of the dynamics.

In order to calculate the diffusion, a linear fit was performed for every MSD curve only for the steps beyond the first half of the dynamics process; the validation of this procedure was discussed and addressed by Cortés elsewhere [80].

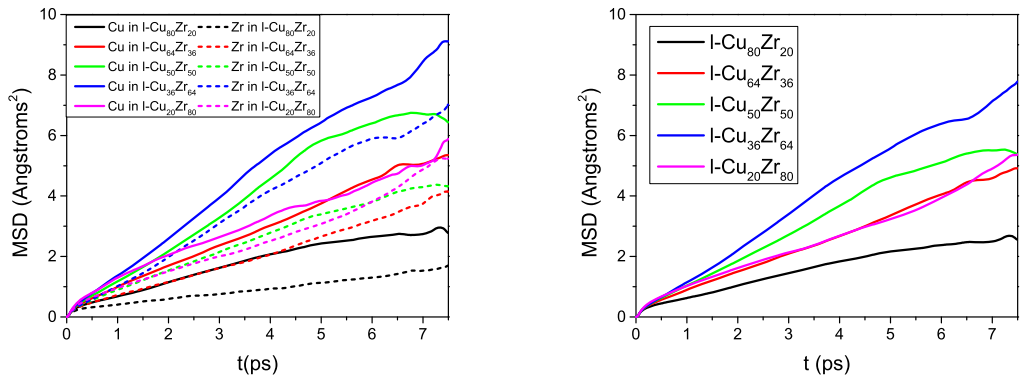

Figure 5.11. Mean square displacements of Cu and Zr in the simulated Cu-Zr liquid alloys. Cu MSD is represented by solid lines and Zr MSD by dashed lines. a) MSD for atomic species; b) total MSD of atoms.

In Fig. 5.12 the diffusion coefficients are plotted as a function of the concentrations. The lowest values correspond to the $Cu_{20}Zr_{80}$, $Cu_{64}Zr_{36}$ and $Cu_{80}Zr_{20}$ alloys. It is understood

that the $Cu_{64}Zr_{36}$ alloy has a very low diffusion value since it has been reported that collective motion of atoms tend to foster metallic glass formation upon quenching [104]. However, in the extreme cases, Cu-rich and Zr-rich concentrations, the low value of MSD can be explained due to the value close to the values of pure elements, i.e., although no pure bulk metallic glasses have been reported experimentally we can say that there would not be atomic mobility due to the crystal stability.

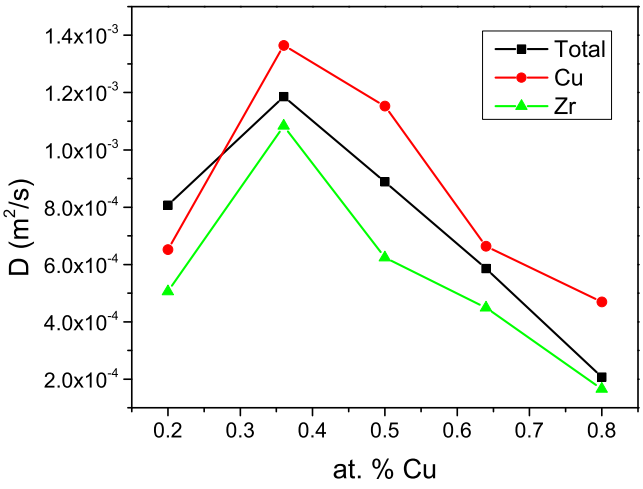

Figure 5.12. Diffusion coefficients of our simulated Cu-Zr liquid alloys calculated from the MSD data.

5.1.2 Comparison with experiment

Since in the last part of section §5.1 we contrasted our results with the simulations reported in [32], a comparison with the experiment is in order. So far, we have the work reported by Holland-Moritz *et al.* [39] where they discussed the topology of some liquid Cu-Zr alloys. In Figs. 5.13 we test the validity of our simulations by comparing them not only with the experimental BT structure factors but with the work reported in [32] as well. Unfortunately, the available results let us only contrast our $Cu_{50}Zr_{50}$ and $Cu_{36}Zr_{64}$ alloys.

First, from Fig. 5.13a it is observed that our calculated S_{NN}s exhibit a slight displacement to higher q values; however, for the $Cu_{50}Zr_{50}$ case we notice a better agreement with experiment [39] than the work reported in [32] for the $Cu_{46}Zr_{54}$ liquid alloy. Moreover, in both of our alloys the second peak bimodality is more prominent and matches better the $Cu_{50}Zr_{50}$ experimental structure factor, which is not the case in the $Cu_{36}Zr_{64}$ case. Despite the arising disparities, our simulations resemble the experiment.

Finally, in Fig. 5.13b the right shifting of our simulated $Cu_{50}Zr_{50}$ $S(q)$ is present again, however, from this comparison where the temperature differs only by 2 K, the first peak match is much better although our second peak still differs in position from the experimental behavior; however, our second peak does exhibit the three bumps present in the curve from Holland-Moritz *et al.* This suggests that the SRO in our simulated $Cu_{50}Zr_{50}$ liquid alloy indeed reproduces the real liquid local atomic environment. This confirms the validity not only of our results, but of the method used herewith to generate reliable liquid samples that resemble the real ones.

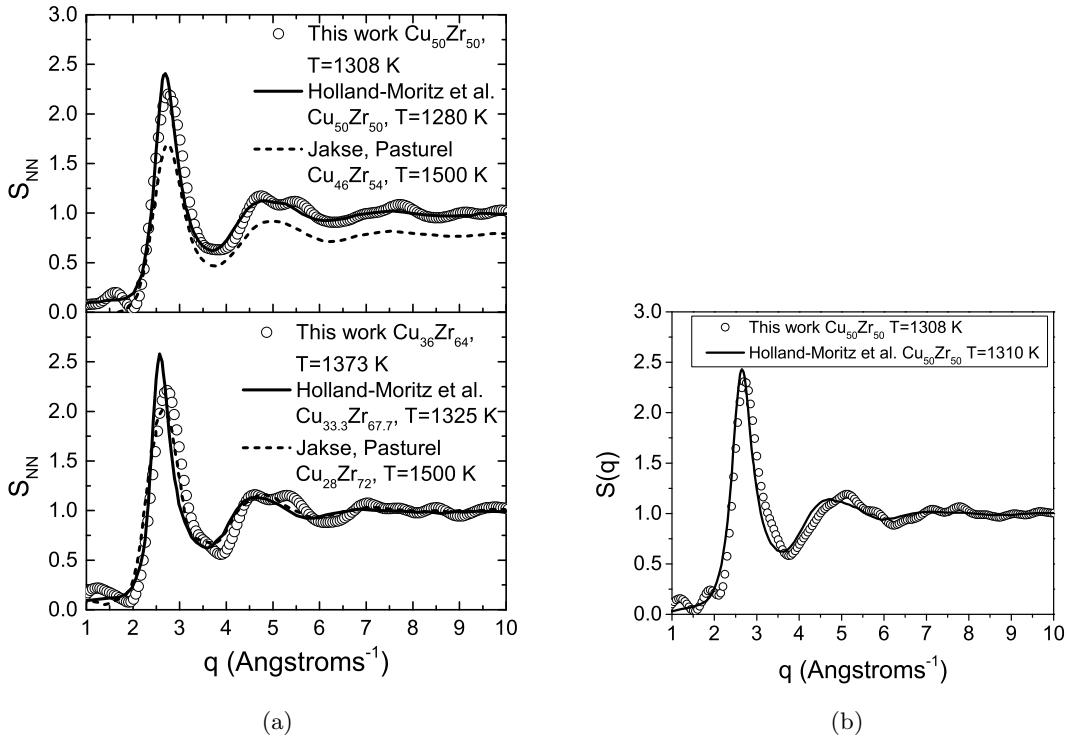

(a) (b)

Figure 5.13. Bathia-Thornton structure factors: a) partial S_{NN} comparison with the AIMD from [32] and the experiment from [39]; and b) total $S(q)$ comparison with experiments reported in [39].

5.2 Properties

Next a discussion on the electronic and vibrational properties of the liquid alloys is presented. Perhaps it might not be surprising that the molten alloys would be also metallic; however, the analysis will be focused on how metallic they are for it is known that in the

liquid state overcoordination or subcoordination exist due to the thermal energy of the system.

5.2.1 eDOS and vDOS

In this section the results of partial and total electronic densities of states are presented. As in the amorphous case, a normalization of the integral to 1 of the peDOS and eDOS was performed for a proper comparison since there are disparities in the number of electrons from one alloy to the other.

First, in Figs. 5.14 similar trends for the peDOS are observed, that is, s orbitals do not exhibit an important contribution as p orbitals in the case of Cu and Zr, and d orbitals in the case of Zr. d orbitals of the alloy seem to be ruled at low energies by Cu due to its filled d band and by Zr near the Fermi level due to the almost empty d band. At this point, it is interesting to notice that as in the amorphous case, the eDOS at the Fermi level increases as Zr is added to the alloy which might be understood in terms of the previous explanation in §4.2.1.

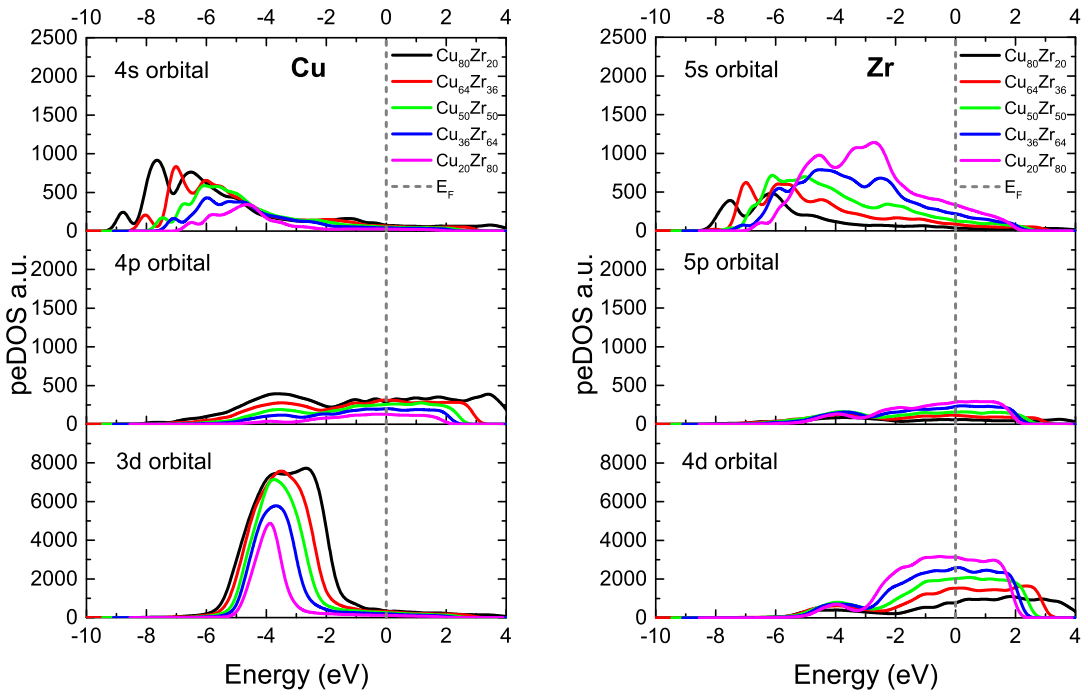

(a) (b)

Figure 5.14. Partial eDOS of the liquid samples. a) Cu partials; b) Zr partials; c) total partial eDOS regardless the atomic species. The Fermi level is indicated as a dashed vertical line.

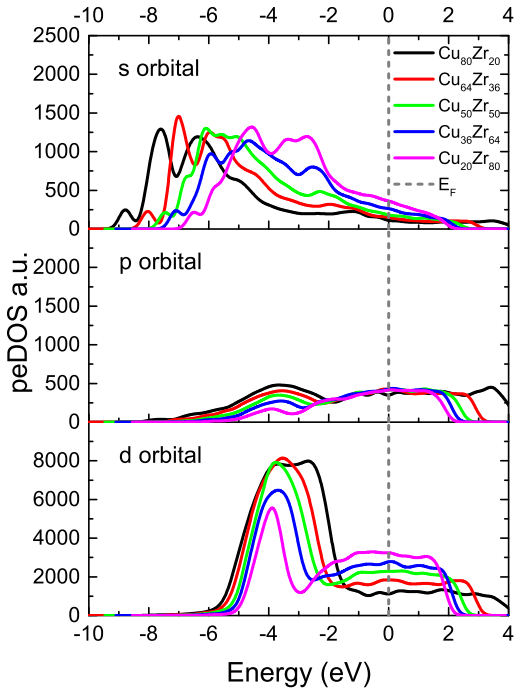

(c)

Figure 5.14. (Cont.) Partial eDOS of the liquid samples. a) Cu partials; b) Zr partials; c) total partial eDOS regardless the atomic species. The Fermi level is indicated as a dashed vertical line.

In the total eDOS (Fig. 5.15) it can be observed that the main peak due to Cu d orbitals tends to shift toward deep energies and the bump region near the Fermi level due to Zr d orbitals appears to increase linearly with Zr content. In our simulated liquids, the anomalous case of amorphous $Cu_{80}Zr_{20}$ alloy where the eDOS at the Fermi level remains the same as amorphous $Cu_{64}Zr_{36}$ is present, but the opposite happens, that is, the largest increment of the number of states at 0 meV. A rather quadratic eDOS at the Fermi level trend instead of a linear one can be verified in Fig. 5.16.

On the whole, the eDOS results confirm a more metallic behavior of our liquids than in the amorphous. This is due to the local atomic arrangement which fluctuates more as a consequence of bond loosening. In addition, since the structure is temperature dependent also the Fermi level should change with it, so a study where the electronic properties of a certain concentration are mapped as a function of temperature in the liquid is a must.

Another relevant property that is intrinsically related to the structure of the samples is the vibration spectrum. In spite of the wide-spread existence in nature of amorphous

solids, glassy solids, etc., their vibrational properties have been largely disregarded by experimentalists. Some theoretical efforts that involve the calculation of vibrations in simple liquid metals have been carried out [105–107].

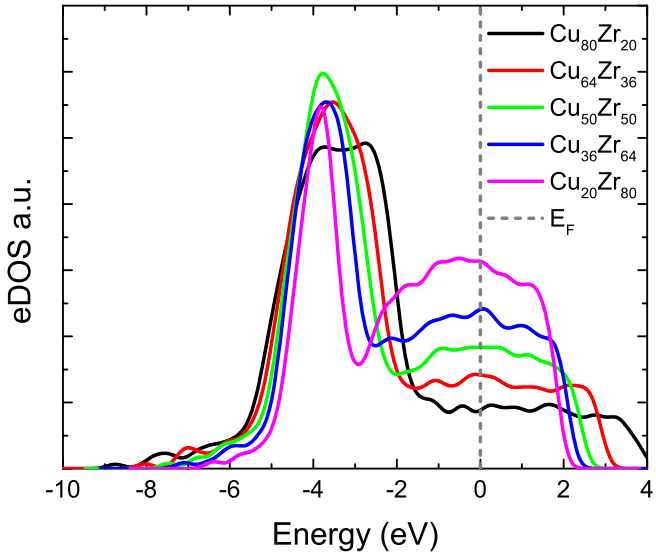

Figure 5.15. Total eDOS of the liquid samples. The Fermi level is indicated as a dashed vertical line.

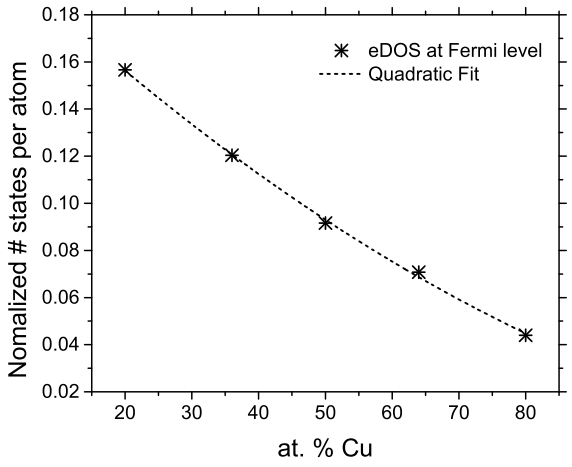

Figure 5.16. eDOS at the Fermi level. Evolution from the total eDOS of our generated liquid samples.

The phonon spectra of our liquids exhibit a rather similar tendency as in the amorphous (Fig. 5.17), for the widespread bimodal profile is present. However, in the amorphous phase the bimodality was in the range of 15-28 meV for the liquid; whereas prominent frequencies are located in the range of 10-28 meV; this means that more low frequencies appear and a slight shift towards the main peak in the liquid is observed.

In the phonon spectra we observed that there were contributions of negative vibration modes (not shown), this emerges as a consequence of stabilization issues of the structure. In other words, since the systems were kept at 100 K above their corresponding *liquidus* for 500 steps, these 5.4 ns were not enough to "relax" the structure in the liquid phase so that negative modes would vanish. Moreover, negative frequencies might be nulled by taking smaller displacements in the harmonic approximation when the modes are calculated; another approach to properly describe vibrations in liquids could be to damp the modes via a friction constant and external driving forces instead of the harmonic approximation as suggested in [108]. Because of this and due to the lack of experimental reports of the phonon spectra, our qualitatively vDOS results should be considered as predictive.

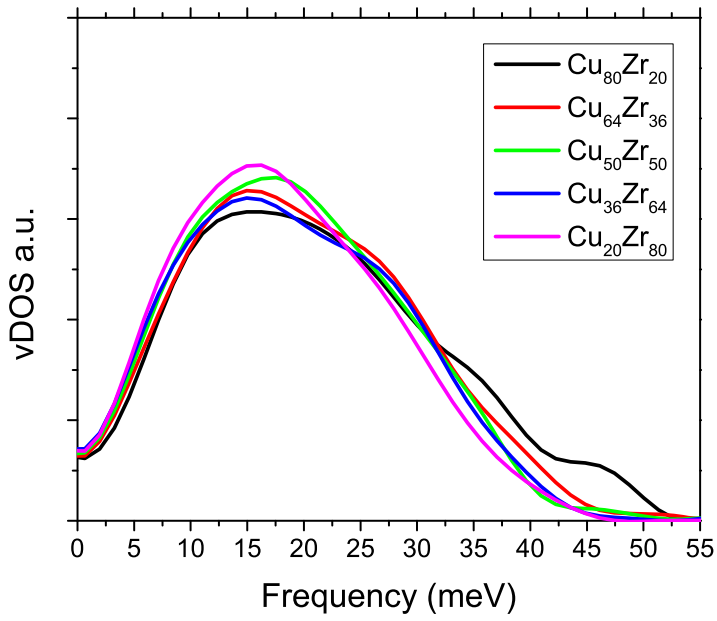

Figure 5.17. Total vDOS of our five generated liquid samples.

Chapter 6

Amorphous porous alloys

Once the results of the amorphous and the liquids have been analyzed, herewith the resulting amorphous porous $Cu_{64}Zr_{36}$ structures are presented using the expanding lattice method. Likewise, the generated amorphous porous Cu and Zr structures are shown, which were generated using the dealloying technique. At this point it is important to remember that only the amorphous concentration $Cu_{64}Zr_{36}$ was chosen since its topology has been widely studied in the literature; therefore, the amorphous structure can be compared with the amorphous non-porous one.

6.1 Expanding Lattice

In Figs. 6.1-6.5 the generated porous samples using an initial unstable "crystalline" supercell (c-$Cu_{64}Zr_{36}$) are presented exhibiting different porosities in the range of 10-50%, whereas the ones generated from the amorphous supercell (a-$Cu_{64}Zr_{36}$) are presented in Figs. 6.6-6.10, for the same range. We show the supercells from the three spatial views in order to make explicit the directions in which the pores grow whenever it applies. Bonds were calculated according to the ratio of the minimum of the corresponding total PDF to the covalent bond distance [71].

In the case where the initial configuration is a "crystalline" unstable supercell (Figs. 6.1-6.5), explicit pore formation in the y axis rather than in the other two directions is observed. These pores are "through pores" which are formed all along the material considering periodic boundary conditions.

When the initial structure was first amorphized, and then expanded, results are somewhat different from the previous case because in the y spatial direction pore formation is not so evident; pores grow systematically with no preferential direction as porosity increases up to the point of 50% of porosity where "through pores" are present in all spatial directions. In addition, at the highest porosity level we observe an interesting feature: inside the backbone (strut) there is a small pore besides the larger one which can be noticed in the x direction only (Fig. 6.10a).

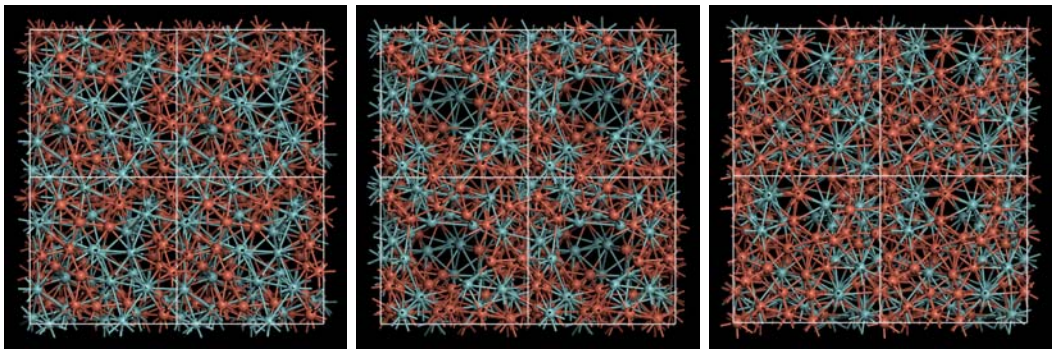

(a) (b) (c)

Figure 6.1. Ball-and-stick resulting amorphous nanoporous sample with initial c-$Cu_{64}Zr_{36}$ structure with 10% of porosity: a) x axis view; b) y axis view; c) z axis view.

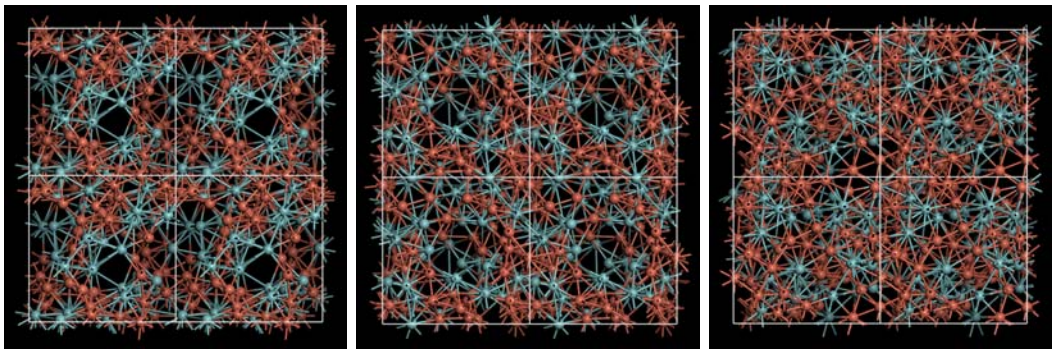

(a) (b) (c)

Figure 6.2. Ball-and-stick resulting amorphous nanoporous sample with initial c-$Cu_{64}Zr_{36}$ structure with 20% of porosity: a) x axis view; b) y axis view; c) z axis view.

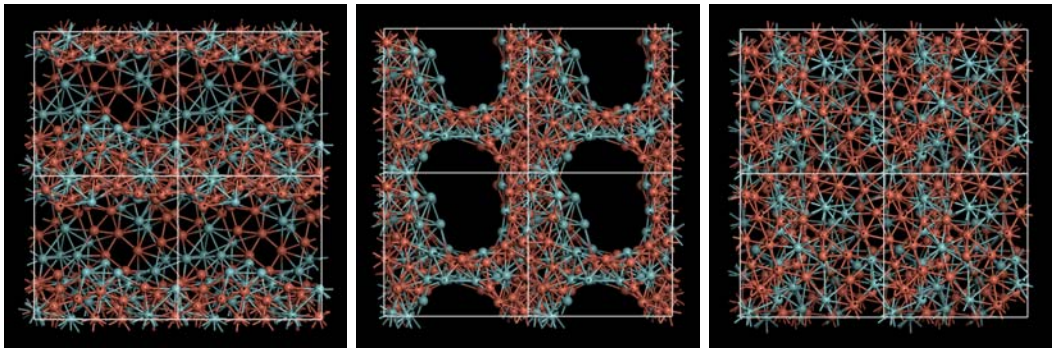

(a) (b) (c)

Figure 6.3. Ball-and-stick resulting amorphous nanoporous sample with initial c-$Cu_{64}Zr_{36}$ structure with 30% of porosity: a) x axis view; b) y axis view; c) z axis view.

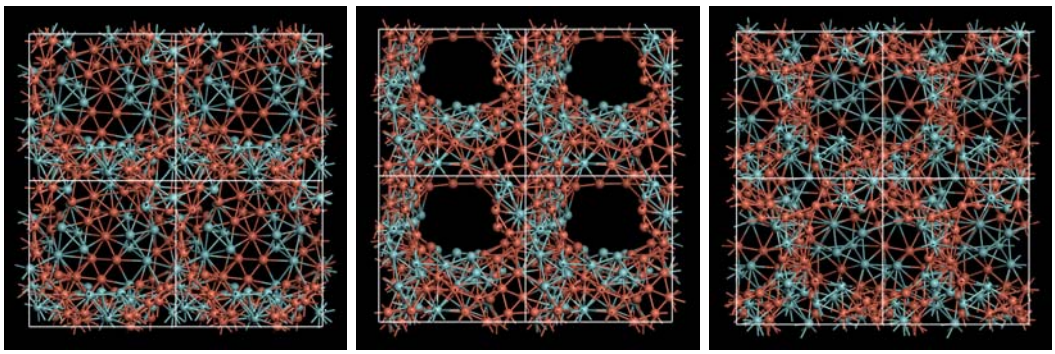

(a) (b) (c)

Figure 6.4. Ball-and-stick resulting amorphous nanoporous sample with initial c-$Cu_{64}Zr_{36}$ structure with 40% of porosity: a) x axis view; b) y axis view; c) z axis view.

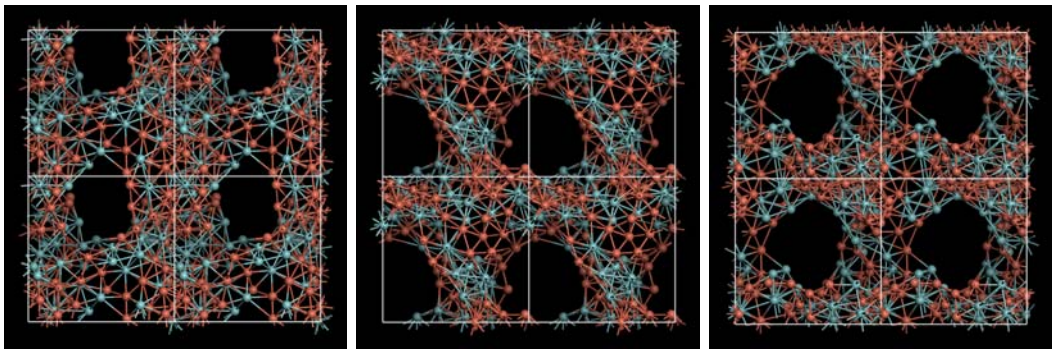

(a) (b) (c)

Figure 6.5. Ball-and-stick resulting amorphous nanoporous sample with initial c-$Cu_{64}Zr_{36}$ structure with 50% of porosity: a) x axis view; b) y axis view; c) z axis view.

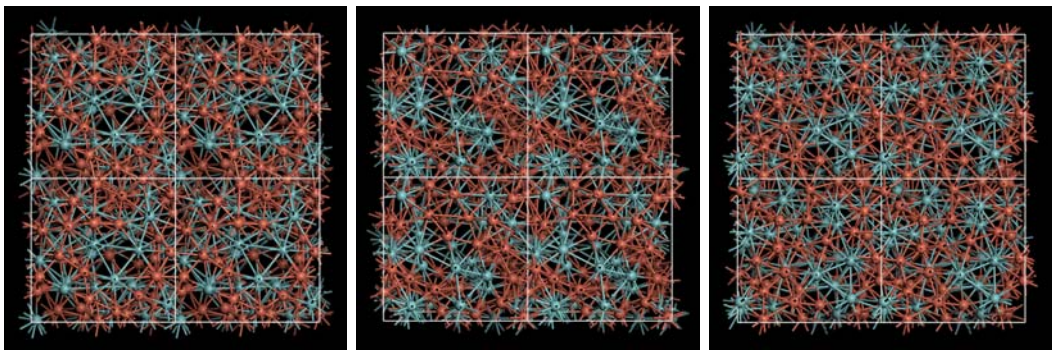

(a) (b) (c)

Figure 6.6. Ball-and-stick resulting amorphous nanoporous sample with initial a-$Cu_{64}Zr_{36}$ structure with 10% of porosity: a) x axis view; b) y axis view; c) z axis view.

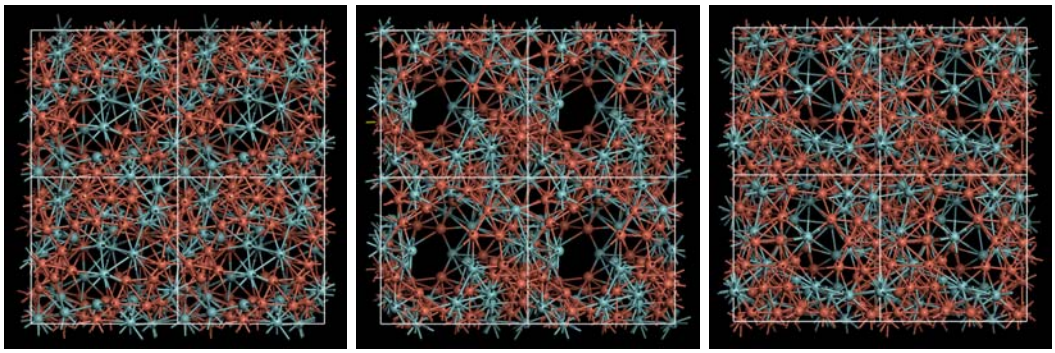

(a) (b) (c)

Figure 6.7. Ball-and-stick resulting amorphous nanoporous sample with initial a-$Cu_{64}Zr_{36}$ structure with 20% of porosity: a) x axis view; b) y axis view; c) z axis view.

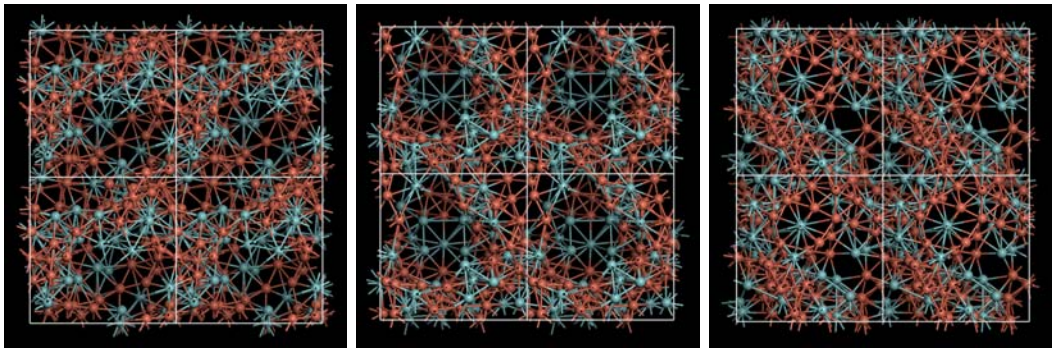

(a) (b) (c)

Figure 6.8. Ball-and-stick resulting amorphous nanoporous sample with initial a-$Cu_{64}Zr_{36}$ structure with 30% of porosity: a) x axis view; b) y axis view; c) z axis view.

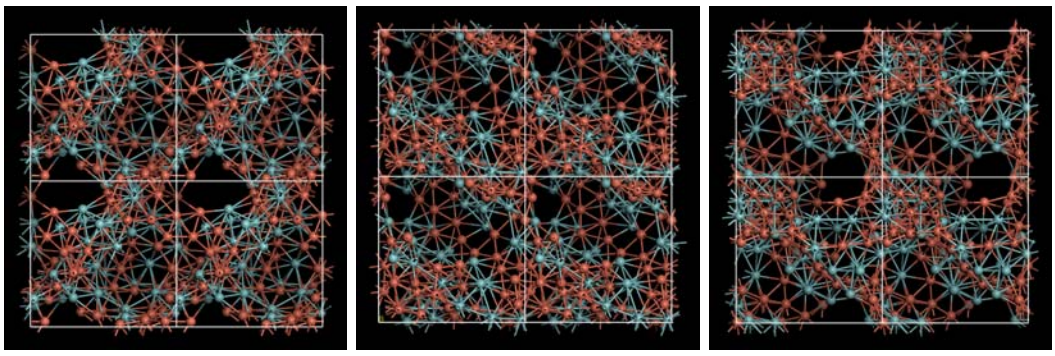

(a) (b) (c)

Figure 6.9. Ball-and-stick resulting amorphous nanoporous sample with initial a-$Cu_{64}Zr_{36}$ structure with 40% of porosity: a) x axis view; b) y axis view; c) z axis view.

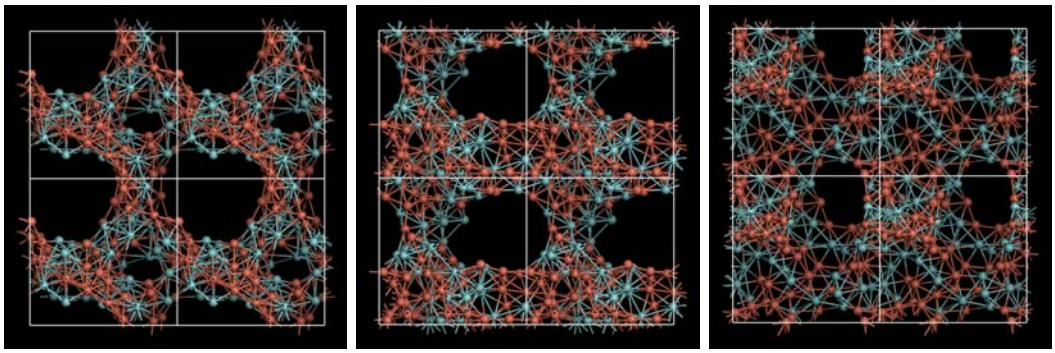

(a) (b) (c)

Figure 6.10. Ball-and-stick resulting amorphous nanoporous sample with initial a-$Cu_{64}Zr_{36}$ structure with 50% of porosity: a) x axis view; b) y axis view; c) z axis view. Notice the additional small pore along the x axis.

We might add that, although the initial structure is the same, the only prevailing feature of our porous samples is the through pore evolution in the y axis. Such behavior suggest that the final amorphous porous samples are very sensitive to the expansion process applied, i.e., to the free volume introduced because atoms will rearrange in different directions depending on the space they have and the local atomic environment.

We think that these discrepancies in pore growth from the initial unstable crystal or from the inital amorphous sample, are a consequence of the stability of each system. While the crystal is unstable to start, according to the phase diagram [90], this instability fosters larger motion of atoms to rearrange into a completely different order. The initial amorphous system will not rearrange easily since it would require more energy to break the stable amorphous local order at which the temperature of the simulation was run.

To compare the SRO in the amorphous porous with respect to the amorphous non-porous alloy we obtained the PPDF and the total one, these are shown in Figs. 6.11 for the initial "crystalline" sample. We observe the interesting feature that in all PDFs the trend is to increase the first peak. Although the bimodality appears in the second peak, indicating an ILSRO, it is rather a multimodal profile which suggests that other geometries are present in our structures. Moreover, the extent of the first and second peaks remains with no change as porosity changes. As previously mentioned in §4.1, the fluctuations that appear in the Zr-Zr partial are due to the number of atoms in our simulations, that is, 39 Zr atoms.

In the amorphous-based samples, Fig. 6.12,it can be noticed that the first peaks become higher than in the crystalline-based case when porosity increases, in part from the Cu-Zr partial. Furthermore, we observe an interesting contraction of the second peak in Cu-Zr

partial and total PDFs, as well as a small bump between the first and the second peak in all partials which was not present in the crystalline-based case. These features indicate a clear rearrangement of atoms when free volume is added to the system, i.e., they tend to get close together and shrink, a behavior that could be possible if there is enough space for atoms to move to or if there is something that "pushes" into the backbone: the pore. This is just a first-approximation explanation of the phenomenon since further investigations should be carried out by letting the simulation cell to be optimized in order to study how the system behaves when density changes, and also by increasing the number of atoms in the simulation cell.

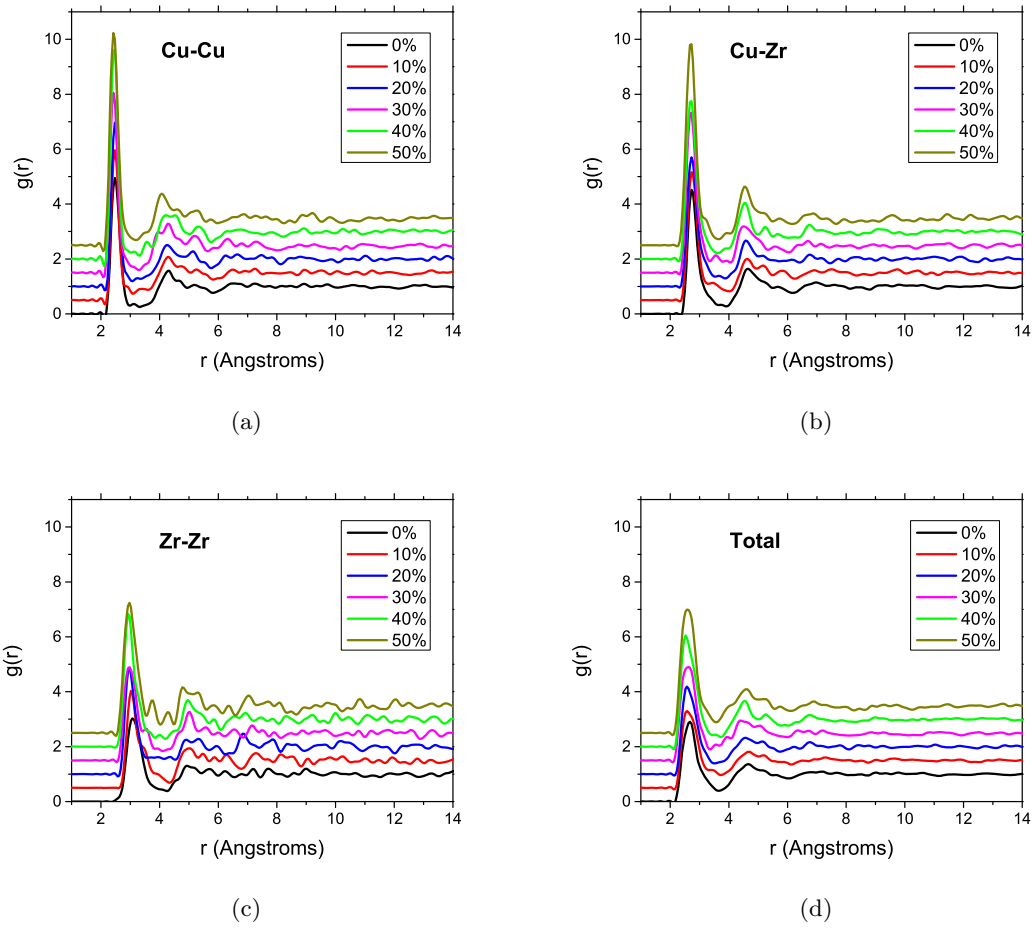

Figure 6.11. Partial pair distribution funcions of the porous samples generated using the EL method on a unstable "crystalline" initial configuration: a) Cu-Cu; b) Cu-Zr; c) Zr-Zr; d) Total. For a proper comparison, the curves were displaced.

To further analyze the topology of the amorphous porous samples, in Figs. 6.13 and 6.14

the graphs of the nearest neighbors position and the coordination numbers as a function of porosity are presented.

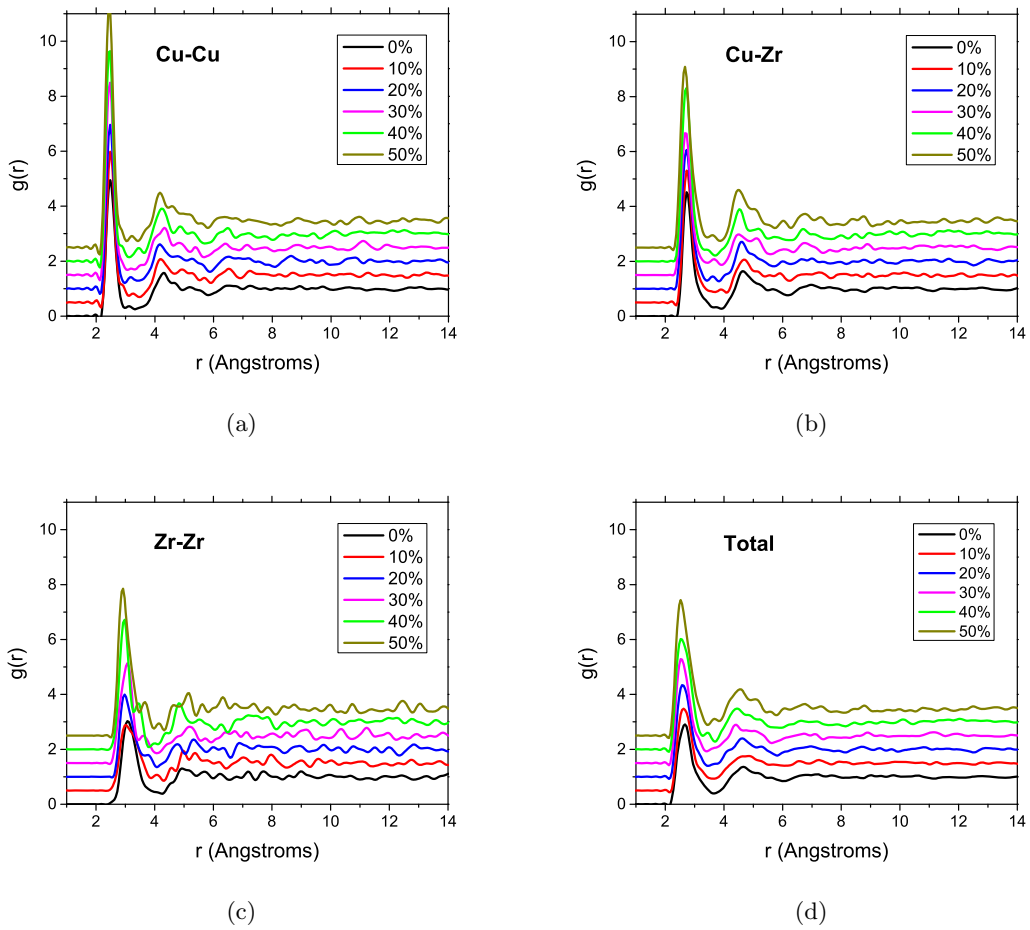

Figure 6.12. Partial pair distribution functions of the porous samples generated using the EL method on a amorphous initial configuration: a) Cu-Cu; b) Cu-Zr; c) Zr-Zr; d) Total. For a proper comparison, the curves were displaced.

Comparing the nearest neighbor positions (Fig. 6.13a) it is clear that Cu-Cu and Cu-Zr do not vary significantly. On the other hand, both Zr-Zr and the total are more affected by porosity. This reticency of Cu to modify its position can be understood in terms of bonding due to its electronic configuration; since it is a noble metal, Cu tends to keep the same bond length with other Cu atoms despite the free volume added to the simulation cell due to the cell expansion and the energy gained by the unstable initial configuration. Although the bond is metallic, the orientation of nearest Cu atoms may change but the bond length will remain the same. Likewise, this behavior is present in the Cu-Zr bond

length. However, for Zr-Zr the tendency is that atoms get closer together about 3%. So, we can say that the samples undergo a slight shrinkage as the porosity increases.

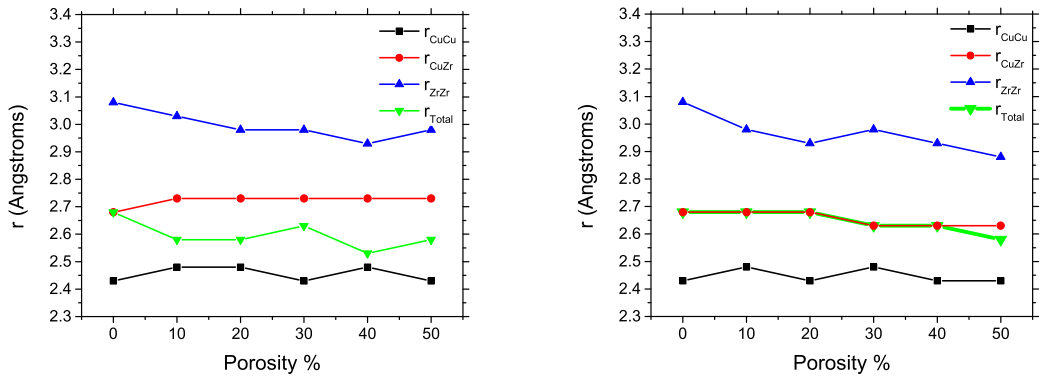

Figure 6.13. Calculated nearest neighbor positions for a) crytalline-based, and b) amorphous-based porous samples using the EL method.

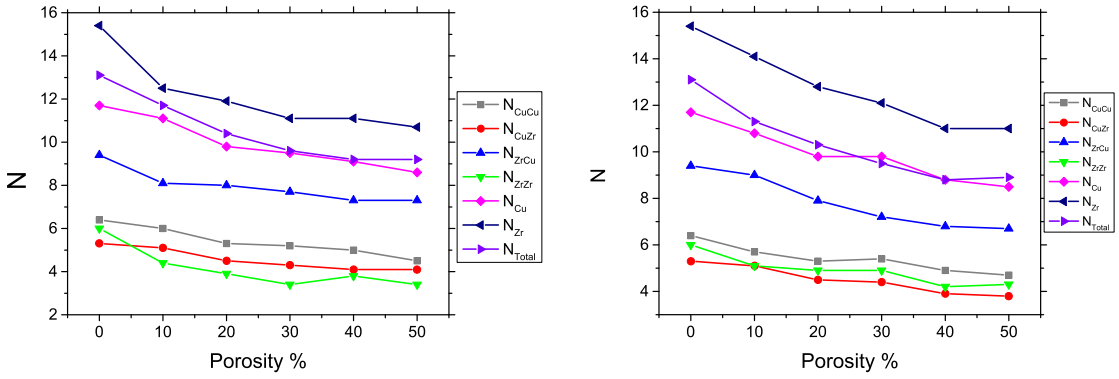

Figure 6.14. Calculated coordination numbers for a) crystalline-based, and b) amorphous-based porous samples using the EL method.

In the amorphous structures several trends arise (Fig. 6.13b) First, we observe that Cu-Cu partial nearest neighbor positions vary somewhat; Zr-Zr positions exhibit a similar behavior to the crystalline-based behavior; Cu-Zr and total positions have technically the same values; this last feature strengthens the idea that the stability due to the chemical environment of the initial amorphous sample constrains the porous-making process to some

extent, at least when it is compared to the crystalline-based samples, thus, the backbone in the amorphous-based sample will resemble the non-porous material.

In addition to the way the first neighbor positions vary, all partial and total coordination numbers exhibit a clear trend to decrease as porosity increases (Fig. 6.14a). We understand this as a competition between the backbone atoms and atoms located in the vicinity of the pore. In other words, as the pore grows a large number of atoms tend to be near the surface (which increases with porosity) rather than in the backbone; therefore, the contribution of these undercoordinated atoms dominate. On the other hand, the amorphous-based samples show larger variations of the coordination numbers (Fig. 6.14b). The relevant feature that contrasts with the crystalline-based samples is N_{Cu-Zr} for it lies below N_{Zr-Zr}.

A clear indication of pore growth can be verified in the behavior of the total PDFs at medium range order (MRO), within 7-14 Å (Figs. 6.15). As previously reported by Santiago-Cortés *et al.* [27], a drop in the PDF appears due to the absence of atoms at a certain distance which depends on the size of the simulation box and the pore shape. In our samples, we notice that the PDFs that exhibit the largest drop is the 50% porosity in both cases. If this drop had systematically the same shape, then a rough estimate of the pore size could be obtained by measuring the range in which the PDF remains below 1. We might add that in the amorphous-based samples the depletion of the PDF is more noticeable, suggesting that pores are better formed in all spatial directions than in the crystalline-based case where the y axis was the preferred direction.

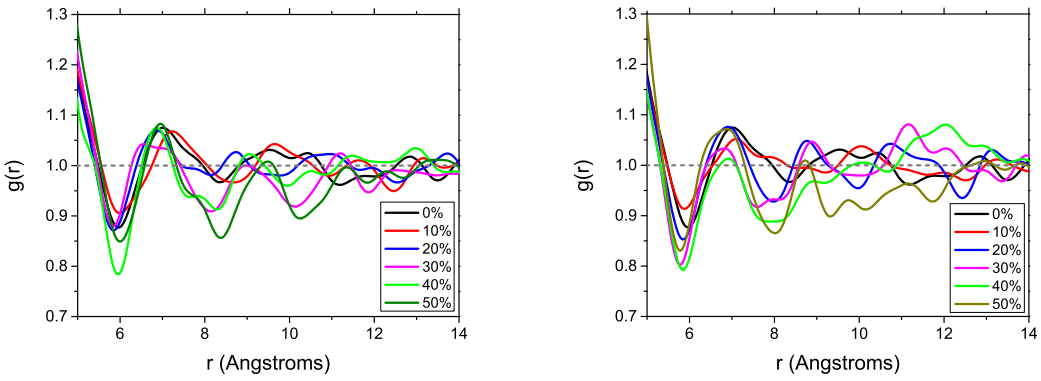

Figure 6.15. Smoothed total PDFs to show the depletion below the average value of 1 in the amorphous porous samples with a) an initial "crystalline" configuration, and b) an amorphous configuration.

Finally, in Figs. 6.16 the bond angle distributions are presented. Surprisingly, the

profiles exhibited are very akin to the non-porous counterpart. A remarkable feature that appears in both BADs is the bimodal profile of the first peak in the range 10-50% of porosity, suggesting the clear presence of distorted icosahedra (58.5°, 60° and 63.5°), up to the 40-50% of porosity range where it vanishes. This may be a consequence of the excess of free volume which affects the local order of atoms letting them move to icosahedron positions. As the free volume increases with the expansion, the number of angles near 60° increases as well as the ones near 108° and 116.5°; the gap between the first and second peak tends to decrease as porosity increases in both cases.

The enhanced characteristic icosahedron-like profile that all five porous samples exhibit regardless of the initial structure, reveals that the role of distorted icosahedra and distorted complex FK polyhedra is relevant in the stability of the backbone in the porous material for the number of those geometries seem to be boosted by the free volume.

The fact that the BAD with 50% porosity in both cases lies below the 40% porosity one in the first and second peaks, and above the gap between them in the crystalline-based sample could be explained in terms of the surface. As mentioned above, the amorphous-based porous sample does not show the same size of pores in all spatial directions as the crystalline-based does; so, if surface increases, more atoms will be near it affecting the geometrical local ordering tending to distort it although keeping the basic ILSRO profile of the amorphous non-porous case.

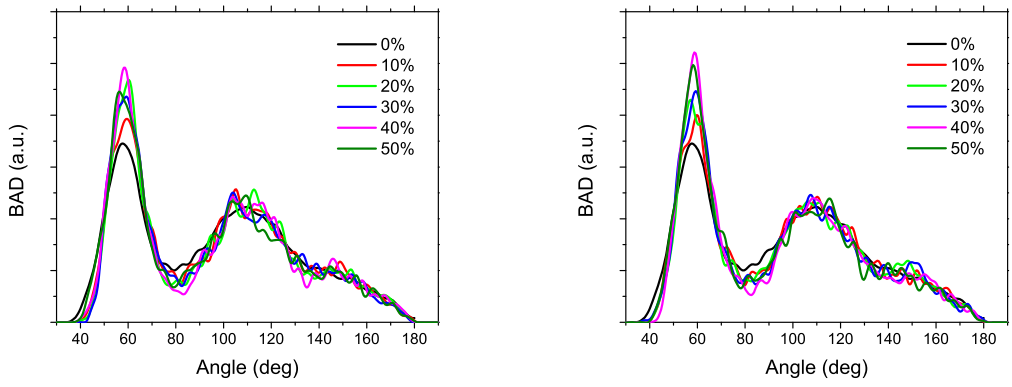

(a) (b)

Figure 6.16. Bond angle distributions of the amorphous porous structures generated with the expanding lattice method; a) initial unstable crystal and b) initial amorphous cell.

The idea of binary BMGFs is very attractive due to their simple composition and the potential applications. However, the difficulties that arise in the experimental generation of

these materials has driven investigations to multicomponent alloys. From this section and the previous results of the amorphous and liquid samples, we can tell that the prevailing icosahedron-like and FK polyhedra geometries are so energetically stable that, even if the simulation box undergoes an expansion up to a point where the density halves, the structure would endure as a backbone which might behave as the bulk material. This conclusion is based on the fact that, in the literature, it has been argued extensively that ILSRO fosters the stability of BMGs which directly impacts on their extraordinary mechanical properties [109]. Although further investigations are needed to verify the influence of cell optimization in the amorphous porous samples, the results presented here provide insight into the field of this amazing materials.

6.2 Dealloying

Once we have presented the results of the porous alloys, in this section we now study a new approach to simulate the generation of amorphous porous pure metals: Cu and Zr.

Although the dealloying technique was used before to generate amorphous porous Cu, Ag and Au [27], the simulation procedure differs somewhat from ours. In this work we base the generation of amorphous porous pure metals on previously generated amorphous $Cu_{64}Zr_{36}$ alloy (Chap. 4), rather than a previously dealloyed unstable crystal as Santiago-Cortés *et al.* We first discuss the resulting atomic structures followed by the PDFs, nearest neighbor positions, coordination numbers and BADs, to understand the topology of the systems as a function of porosity. The behavior of each element is expected to vary due to atomic sizes, that is, Cu's atomic (covalent) radius is about 20% smaller than Zr [110].

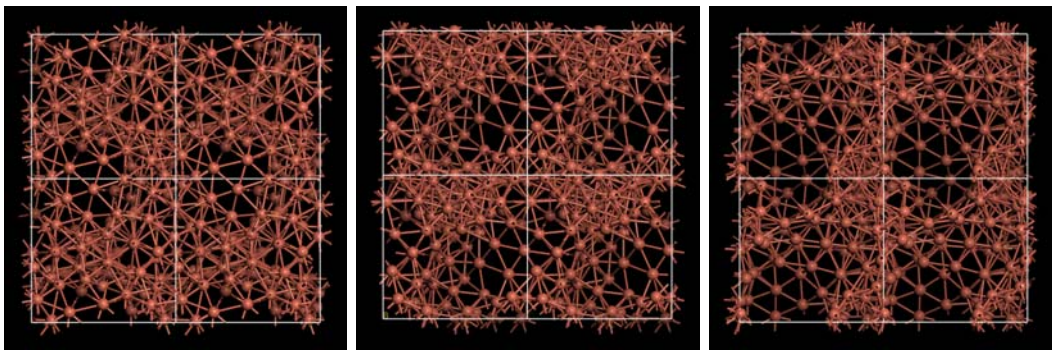

(a) (b) (c)

Figure 6.17. Ball-and-stick resulting amorphous nanoporous Cu with 26.8% of porosity: a) x axis view; b) y axis view; c) z axis view.

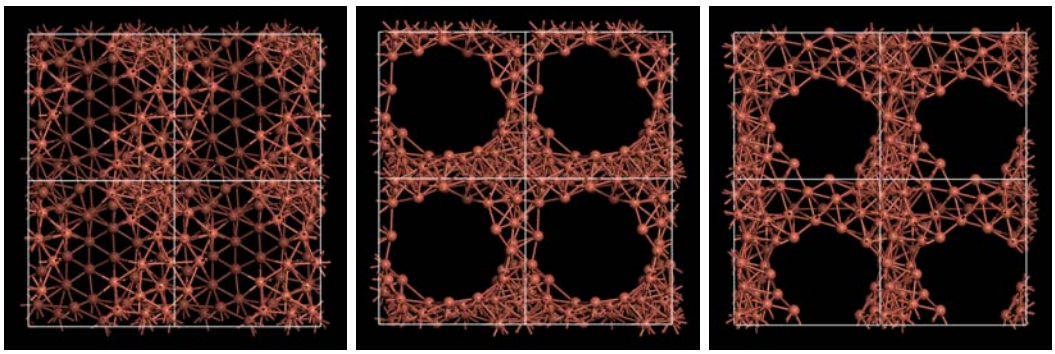

(a) (b) (c)

Figure 6.18. Ball-and-stick resulting amorphous nanoporous Cu with 44.6% of porosity: a) x axis view; b) y axis view; c) z axis view.

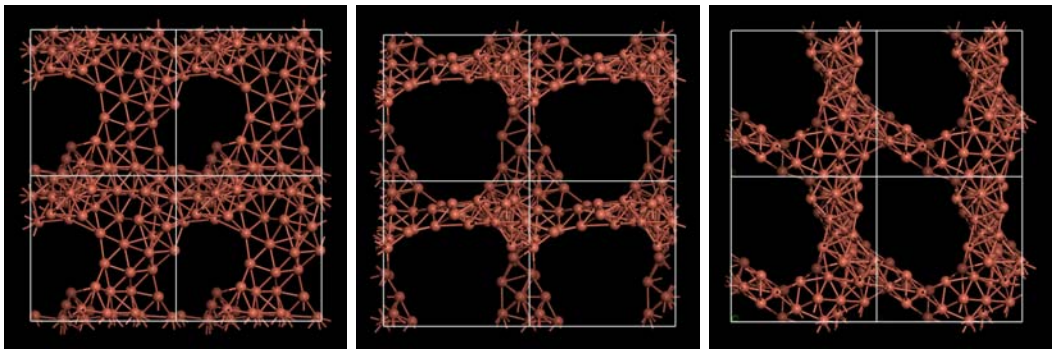

(a) (b) (c)

Figure 6.19. Ball-and-stick resulting amorphous nanoporous Cu with 58.9% of porosity: a) x axis view; b) y axis view; c) z axis view.

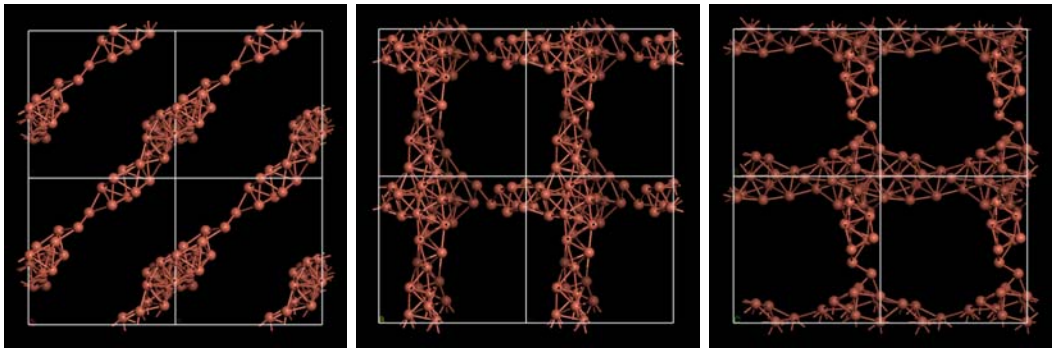

(a) (b) (c)

Figure 6.20. Ball-and-stick resulting amorphous nanoporous Cu with 71.8% of porosity: a) x axis view; b) y axis view; c) z axis view.

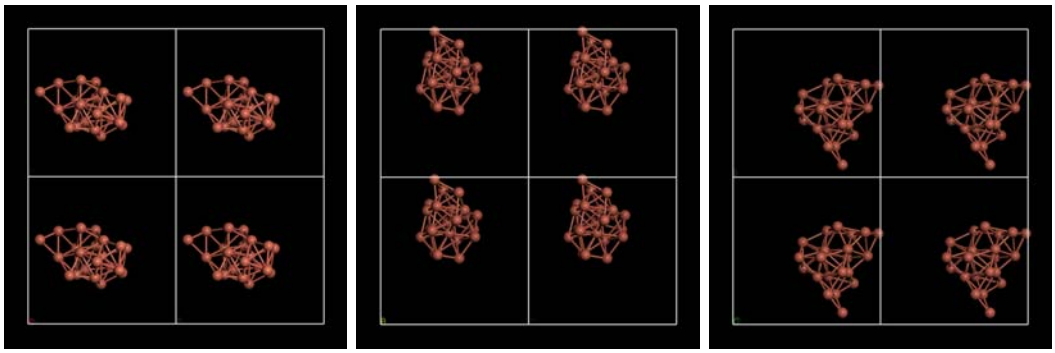

(a) (b) (c)

Figure 6.21. Ball-and-stick resulting amorphous nanoporous Cu with 84.9% of porosity: a) x axis view; b) y axis view; c) z axis view.

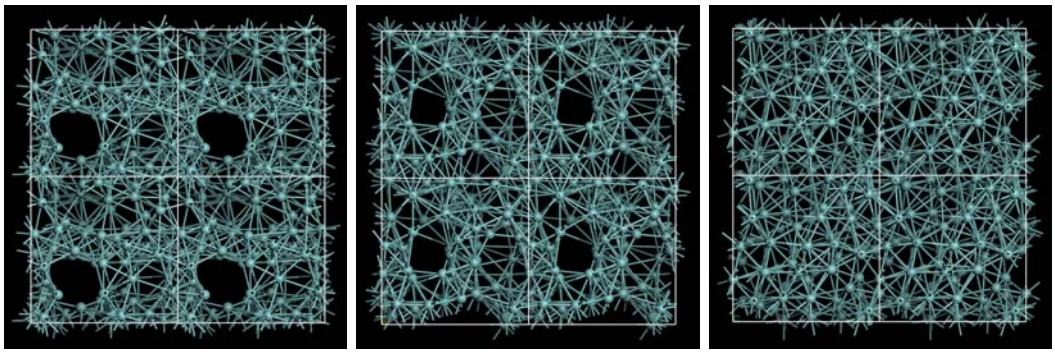

(a) (b) (c)

Figure 6.22. Ball-and-stick resulting amorphous nanoporous Zr with 26.8% of porosity: a) x axis view; b) y axis view; c) z axis view.

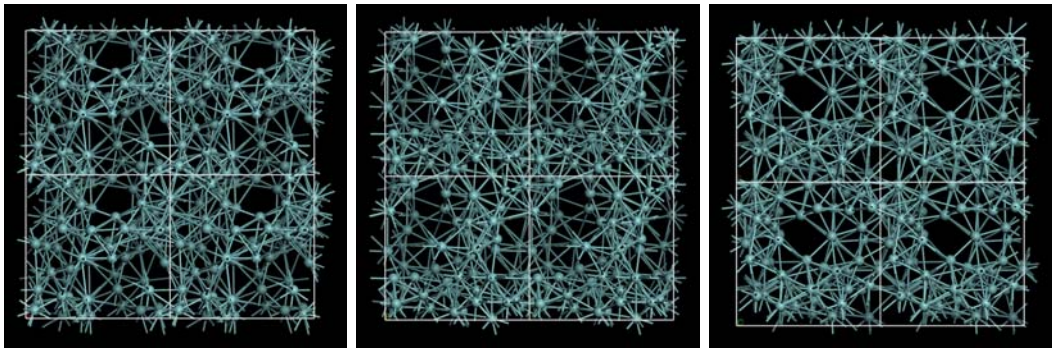

(a) (b) (c)

Figure 6.23. Ball-and-stick resulting amorphous nanoporous Zr with 44.6% of porosity: a) x axis view; b) y axis view; c) z axis view.

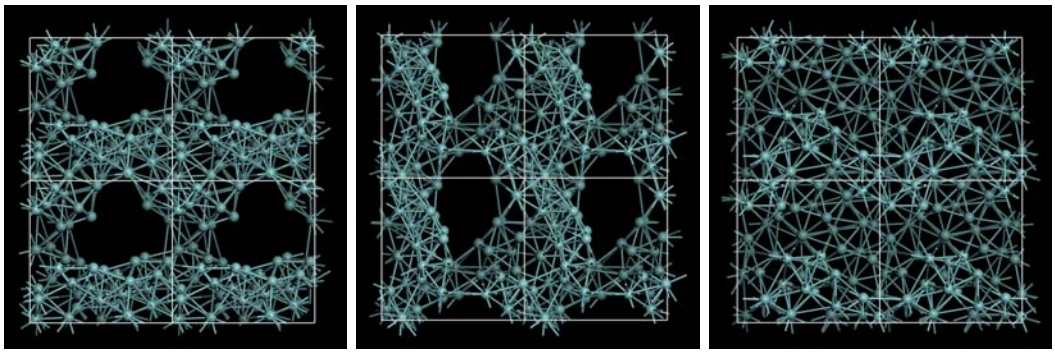

(a) (b) (c)

Figure 6.24. Ball-and-stick resulting amorphous nanoporous Zr with 58.9% of porosity: a) x axis view; b) y axis view; c) z axis view.

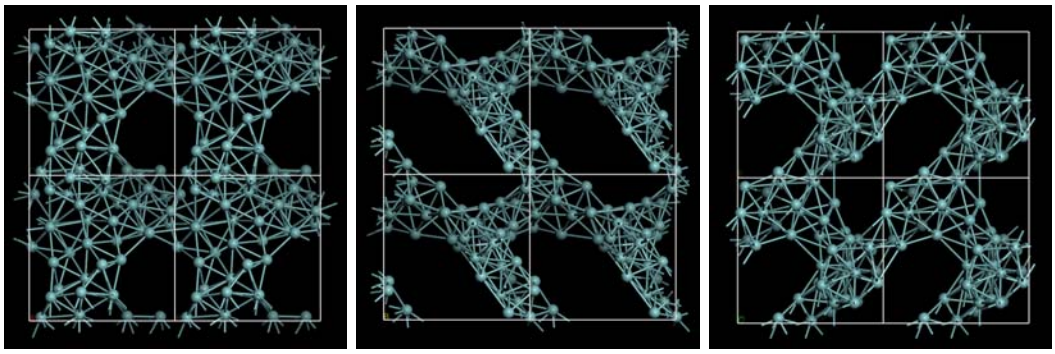

(a) (b) (c)

Figure 6.25. Ball-and-stick resulting amorphous nanoporous Zr with 71.8% of porosity: a) x axis view; b) y axis view; c) z axis view.

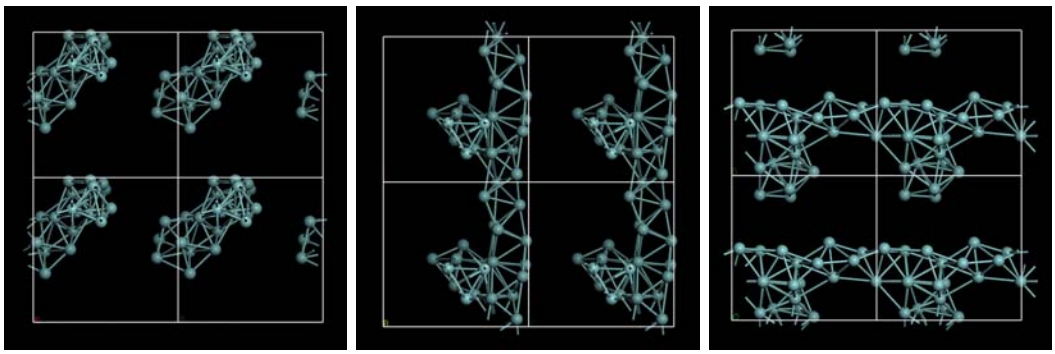

(a) (b) (c)

Figure 6.26. Ball-and-stick resulting amorphous nanoporous Zr with 84.9% of porosity: a) x axis view; b) y axis view; c) z axis view.

In Figs. 6.17-6.26 we present the resulting amorphous porous structures of Cu and Zr after being subjected to AIMD at constant room temperature.

From the resulting structures we observe that Cu exhibits a higher tendency to form pores compared to Zr. While big pores easily appear at 26.8% in Cu (Fig. 6.17), in Zr relatively big pores are present at 58.9% of porosity (Fig. 6.19). Although the idea of directional bonds in metals may not be adequate for obvious reasons, we think that variations in pore size arise as a consequence of bond lengths since bonds lengths in Zr are larger than in Cu (Table 4.1). Therefore, Zr atoms quickly bond and rearrange despite the vacancies of Cu, and the backbone does not narrow as fast as Cu backbone when porosity increases.

Another interesting result in the case of Cu is that at 71.8% of porosity (Fig. 6.19) a layered or laminar structure arises in the x direction besides the y- and z-axis through pores present. At this porosity the backbone is so fine that the structure is joined in its weaker zones by two atoms only, which puts forward the idea that if the free volume increases further, the backbone will collapse and the remaining structure will be somewhat clustered as observed at 84.9% of porosity (Fig. 6.20).

A similar thing is present in Zr at 84.9% of porosity (Fig. 6.26), although not as drastic as in Cu. When we have the top porosity value the structure becomes laminar in y and z directions, however the backbone in the x direction breaks down and it turns into clusters. Accordingly, it can be inferred that the threshold of amorphous porous Zr to remain with a backbone is larger than in Cu, provided that the generation of amorphous porous Cu and Zr by dealloying does not involve cell optimization.

To better understand the changes in the structure, in Figs. 6.27 we show the PDFs, where it is clear that the backbone is amorphous. In Cu we observe that, regardless the porosity, the split of the second peak is always present; we have to remember that this bimodality is related to ILSRO as discussed in [2, 3]. However an atypical PDF for the 84.9% of porosity can be noticed which corresponds to the case where no backbone exists, but clusters. At this level of porosity the height of the PDF is so large compared to the other PDFs because the remaining 22 atoms are located near the center of the simulation box. The contrasting height of the PDFs in Cu with respect to Zr PDFs is due to the fact that the most abundant atomic species is Cu, besides it can be observed that Cu PDFs present a depletion in the medium range (6-12 Å) that is clearer in the samples with higher porosity.

In Zr, the second peak bimodality is not so clear and a small bump between first and second neighbor distances emerges. As metallic bonds allow atoms to rearrange easily, this bump around 4 Å might be a consequence of the surface when the pore is growing, i.e.,

atoms near the surface should make the backbone more stable by bonding with atoms at 4 Å, instead of second neighbors that are further apart.

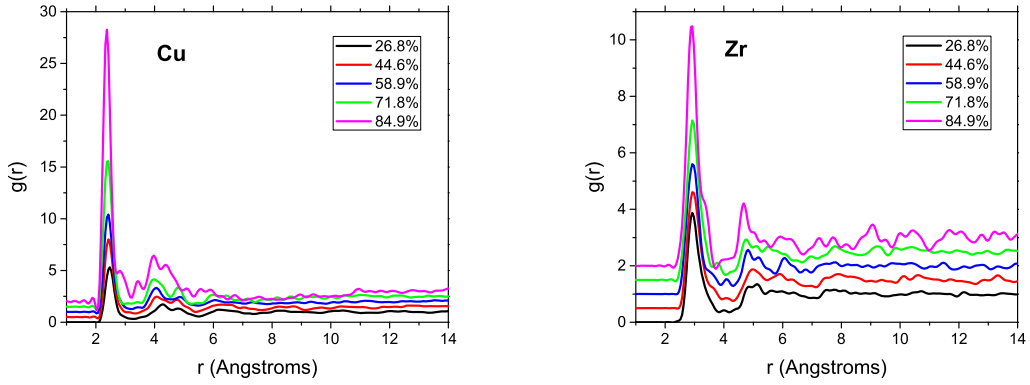

(a) (b)

Figure 6.27. Pair distribution functions of the porous samples generated using the simulated dealloying technique: a) Cu; b) Zr. For a proper comparison, the curves were displaced.

Furthermore, from the analysis of the nearest neighbor positions and the coordination numbers, surprising trends appear (Fig. 6.28). For Cu a decrement of the first neighbor distance is noticeable, while for Zr there is neither an increment nor a decrement. The almost no variation in the position indicates that, although amorphous, the backbone is built up by atoms whose local environment is homogeneously distributed regardless of the porosity. We believe that since there is only one atom type the spatial distribution is not influenced by atomic sizes; the void from the pore will not affect the SRO either because atoms rearrange more efficiently.

As for the coordination numbers, we observe a completely different behavior from one atom type to the other. On one hand, Cu coordination tends to increase as porosity does, and on the other hand, Zr coordination decreases as porosity increases.

This opposite tendencies may be due to the excess free volume in each simulation cell since the response of each atom to the free volume is different. In other words, in the case of Cu, when porosity is low the number of Cu nearest neighbors is large, thus we believe that the system finds its stability by keeping an expanded hexagonal-like network that encloses the pore (See Fig. 6.17); as porosity increases, more surface appears so that Cu atoms tend to come closer and closer to stabilize the backbone, until the point at which that backbone disappears and the remaining atoms must stay as close as possible to minimize the energy of the system. Now, in the case of Zr, from the results of the amorphous samples (Chap.

4) we know that Zr tends to be surrounded by 12 atoms or more (See Fig. 4.3). So, in the case of the lowest porosity, the absence of Cu atoms makes the coordination to fall below 10, and not beyond that value as in Cu, because the bond length of Zr is larger than in Cu, therefore Zr atoms will efficiently fill the vacancies of Cu. At the highest value of porosity (84.9%) Zr does not present clustering as Cu for the same reason, the bonds spatially extend far beyond those of Cu and that is what provides stability to the laminar backbone profile.

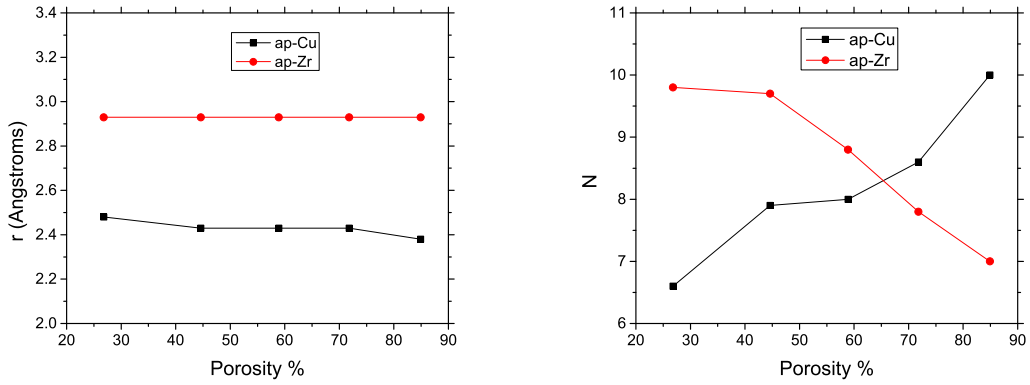

(a) (b)

Figure 6.28. Calculated a) nearest neighbor distances; and b) coordination numbers of the porous samples using the simulated dealloying technique.

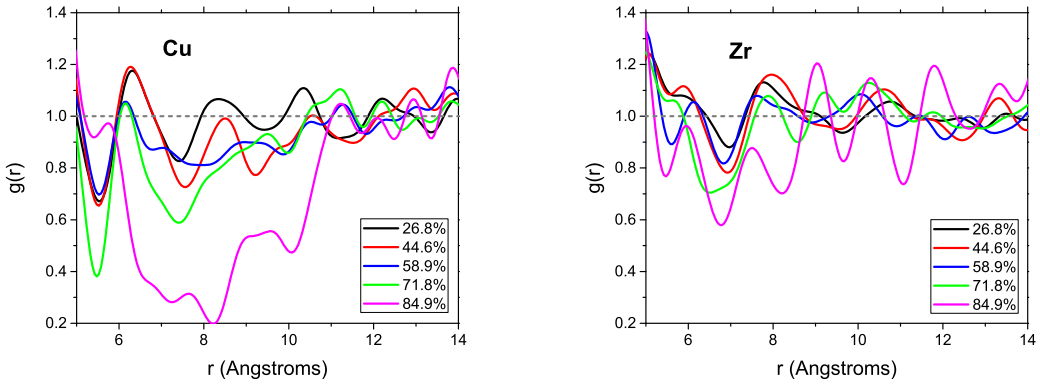

(a) (b)

Figure 6.29. Smoothed total PDFs of the generated samples using the dealloying technique to show the depletion below the average value of 1; a) amorphous porous Cu, b) amorphous porous Zr.

As in the EL results (Sec. 6.1), in Figs. 6.29 we present an amplified graph of the region in which the PDF drops below its average value of 1. As previously mentioned, this depletion is associated with the size of the pore because a rough estimation can be calculated from it.

In the case of Cu the depletion is more evident for all curves apart from the the 26.8% sample, contrary to Zr where the depletion is not useful to estimate the pore size. In this case, a graphic approach could be used to measure the size of the pore, however, the problem of delimiting the surface/pore is not straight forward, thus resulting in an onerous endeavor.

Finally, we present the BADs where, as in all our results so far, the preferred ILSRO profile prevails in both amorphous porous Cu and Zr. It is amazing to see that as porosity increases the number of angles associated to an icosahedron-like form does as well. Again, distorted or rather truncated icosahedra seem to be the building blocks in our simulated amorphous porous pure metals.

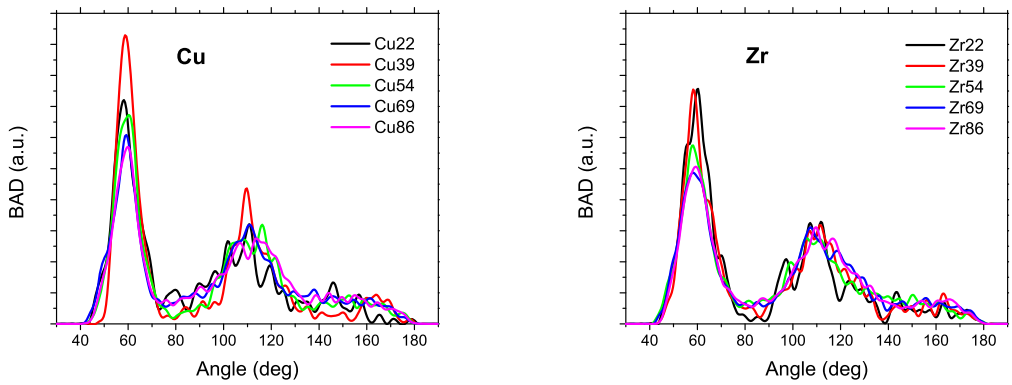

(a) (b)

Figure 6.30. Bond angle distributions of amorphous porous a) Cu, and b) Zr; all samples exhibit an icosahedron-like angle distribution.

Although the results presented in this final chapter might be taken as predictive due to the lack of experimental counterparts to compare with, we believe that they would contribute to the understanding of the possible mechanisms and processes that may underlie the generation of this promising materials, since our comparison is based on the results for the amorphous samples which have been already validated with experiment.

6.3 Reactivity

In this last section we present some results related to the reactivity of the amorphous porous $Cu_{64}Zr_{36}$ alloy in terms of the Fukui Function (FF) (Sec. 2.4). We chose the crystalline- and amorphous-based samples with 50% porosity as representative of the set of results since they exhibit the largest pores, and one of the ideas of porous materials is to study whether it is feasible to either adsorb or absorb any chemical element.

From Figs. 6.31 and 6.32 the FFs of both the crystalline-based and amorphous-based ap-$Cu_{64}Zr_{36}$ alloy are presented. In the electrophilic cases (Figs. 6.31a and 6.32a) we see that the highest values of the function (which are negative) are located at the boundary between the backbone and the pore, while the lowest are mainly around Zr atoms; this means that the system would not lose stability upon electron removal near the surface of the backbone. In the nucleophilic representation the highest values of the FFs are not near the backbone boundary, but instead near Zr atoms, which is opposite to the electrophilic behavior (Figs. 6.31b and 6.32b), besides there are no negative values of the FF. This result suggests that the surface turns into a donor surface where electrons of an external chemical agent might interact with the backbone by removing electrons from the surface up to some extent, while Zr atoms play the role of acceptor centers of electrons which may be due to the relative low energy cost of 4d electrons to move and to form bonds with other Zr or Cu atoms. Roughly, a straightforward result is that we can neither claim nor turn down the possibility that our simulated ap-$Cu_{64}Zr_{36}$ is capable of storing gases such as H; the lack of a criterion to discern the limits of the surface is crucial.

Since radical FFs (Figs. 6.31c and 6.32c) are the average of the eletrophilic and nucleophilic contributions, they exhibit small negative values compared to the eletrophilic FFs. With this, we assert that nucleophilic contribution is quantitatively larger than the electrophilic one; so, despite its presence, negative FF values are not preponderant in either crystalline- or amorphuos-based ap-$Cu_{64}Zr_{36}$.

The existence of negative values of the FF have been discussed in the literature. As a first approximation this case was not believe to be possible in molecules because it had no physical meaning at all. However, this phenomenon has been understood in terms of asymmetric configurations in molecules [111] and by taking into account orbital relaxation effects, for removing an electron from the HOMO deshields the remaining occupied orbitals, allowing them to contract toward the atomic nuclei [74, 75, 112]; in our case, electrons that belong to Zr. So, since our generated amorphous porous structures exhibit a high asymmetric environment due to structural disordering and expansion, the existence of negative values is rather *natural*. A somewhat similar situation was reported by Santiago-

Cortés *et al.* for amorphous porous Cu, Ag and Au, because the negative values were symmetrically located opposite to the largest values of the FF: inside the backbone [27].

Although these qualitative ideas rely on the electronic behavior of Cu and Zr, further studies must be carried out in order to quantify the energetic cost of absorption on the surface or adsorption in the material [22].

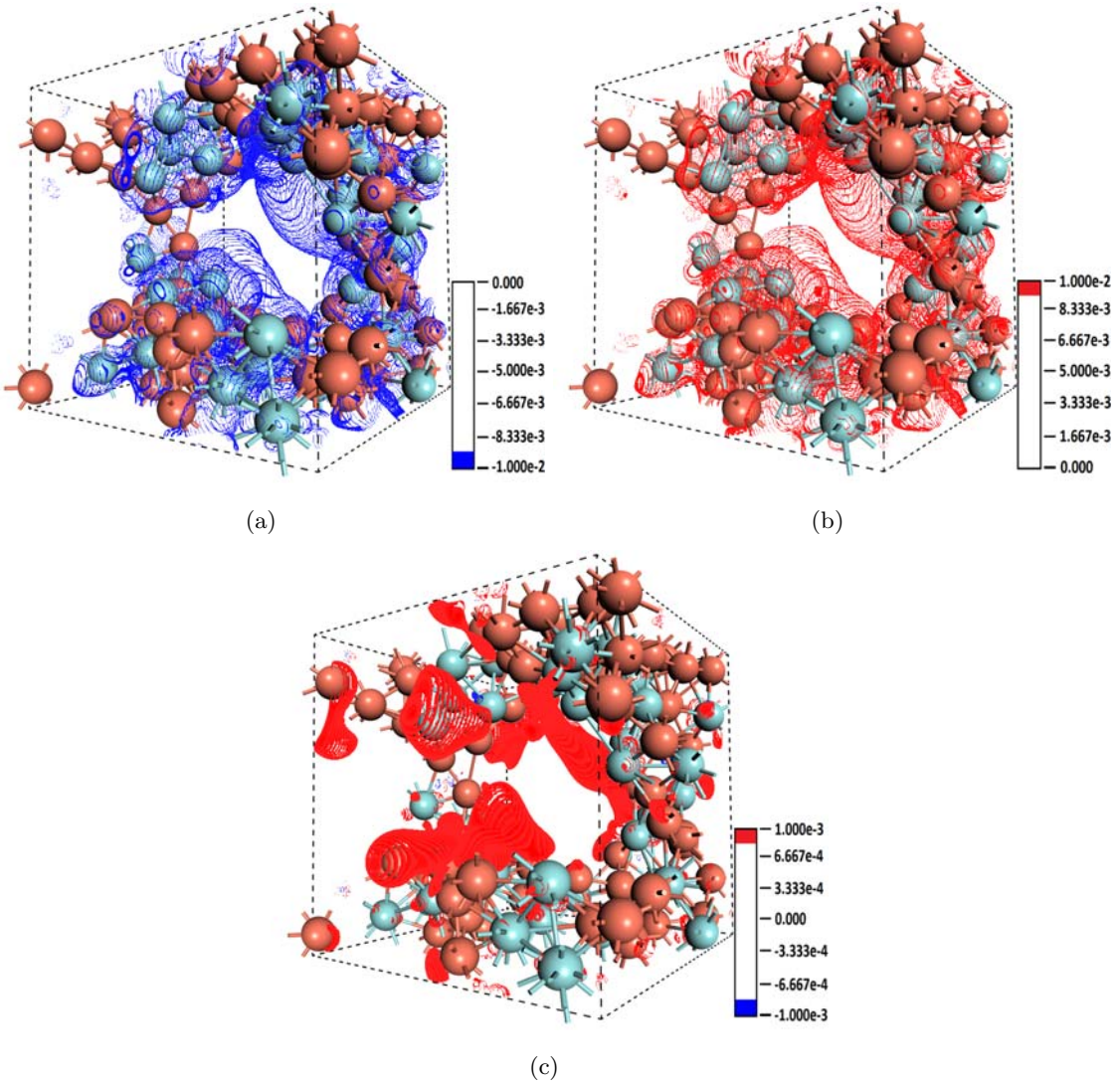

Figure 6.31. Fukui functions calculated for the crystalline-based ap-$Cu_{64}Zr_{36}$ represented as field isosurfaces; a) electrophilic (f_N^-; highest eletrophilic sites are marked in blue); b) nucleophilic (f_N^+; highest nucleophilic sites are marked in red); c) radical (f_N^0; highest radical sites are marked in red). The units of the field are Ha/Å^{-3}.

In the case of dealloyed Cu and Zr, we chose to calculate the FFs of the samples at

58.9% and 71.8% porosity correspondingly; this, because we think that at this porosity values the largest backbone to pore ratio takes place, i.e, the pore is big enough to let a chemical reagent to come inside and the backbone is thick enough to stabilize the dendritic struts. Then, in Figs. 6.33 and 6.34 we present the three FFs calculated for ap-Cu and ap-Zr.

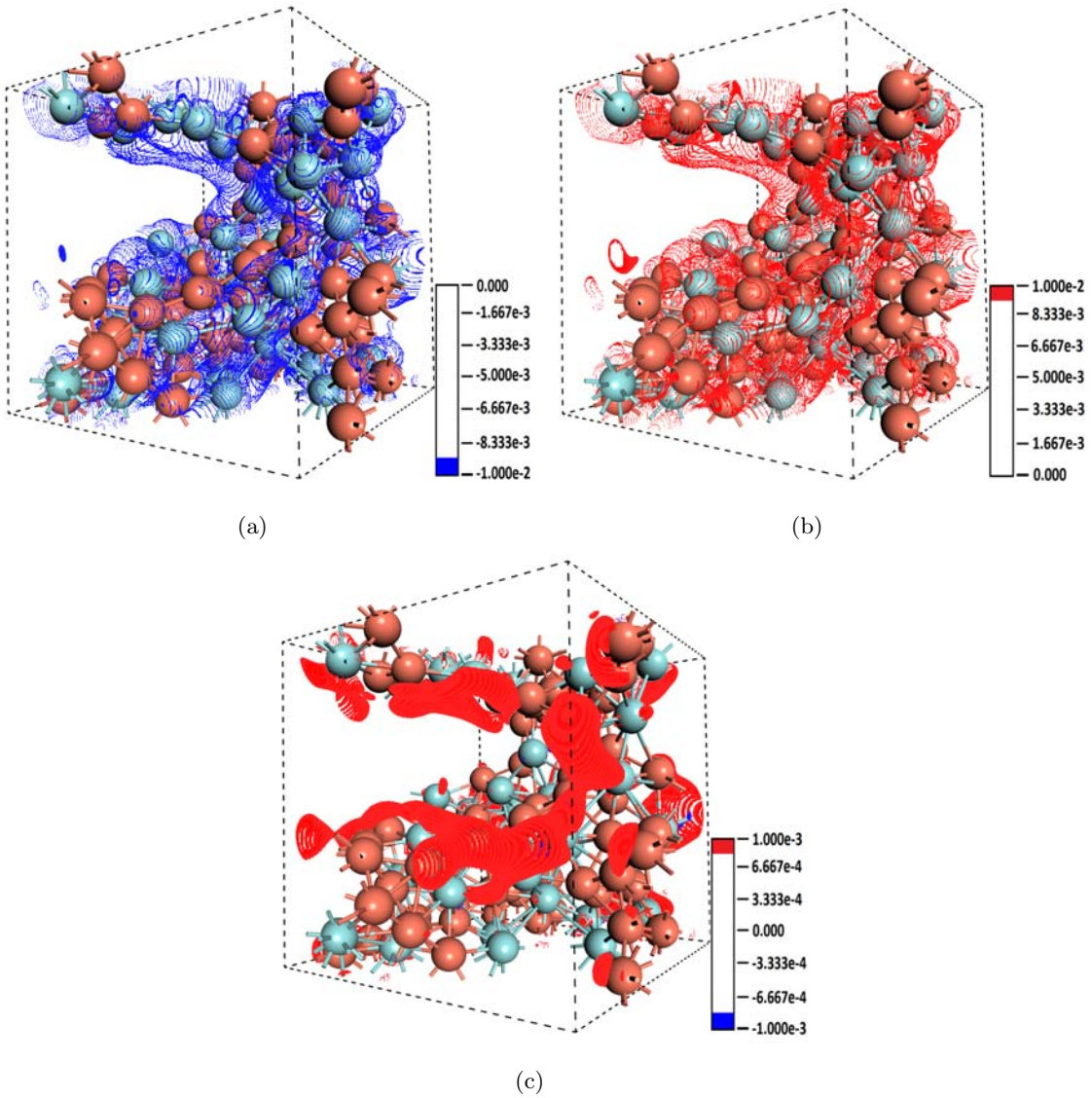

(a) (b)

(c)

Figure 6.32. Fukui functions calculated for the amorphous-based ap-$Cu_{64}Zr_{36}$ represented as field isosurfaces; a) electrophilic (f_N^-; highest eletrophilic sites are marked in blue); b) nucleophilic (f_N^+; highest nucleophilic sites are marked in red); c) radical (f_N^0; highest radical sites are marked in red). The units of the field are Ha/Å^{-3}.

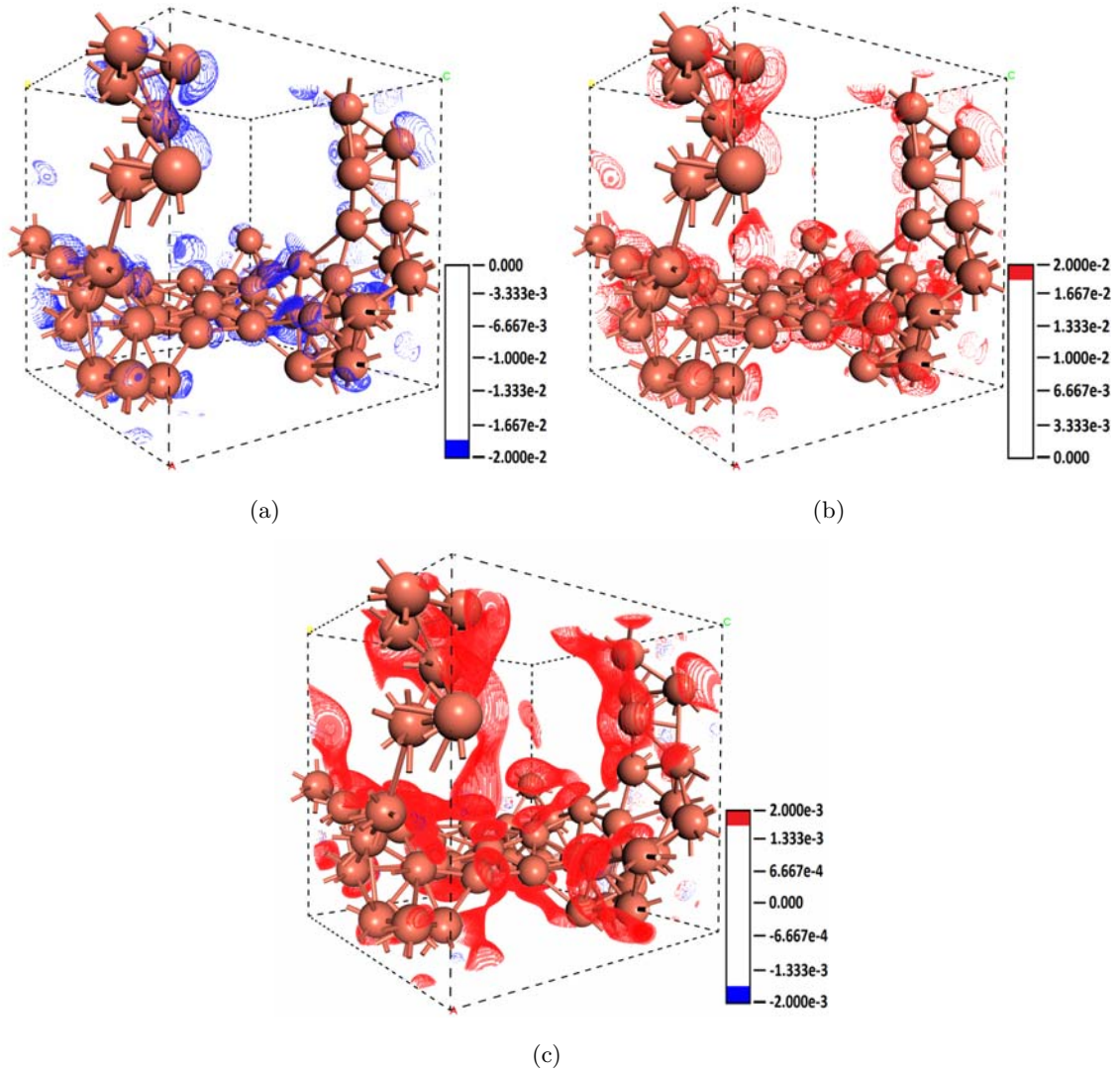

Figure 6.33. Fukui functions calculated for ap-Cu represented as field isosurfaces; a) electrophilic (f_N^-; highest eletrophilic sites are marked in blue); b) nucleophilic (f_N^+; highest nucleophilic sites are marked in red); c) radical (f_N^0; highest radical sites are marked in red). The units of the field are Ha/Å^{-3}.

In ap-Cu (Fig. 6.34a) it is interesting to notice that electrophilic FF exhibits negative values in the backbone with the most negative ones near the Cu atoms that lie close to the *surface*. This is similar to the case of ap-$Cu_{64}Zr_{36}$ in Zr atoms (Fig. 6.34a), however, the highest values are on the surface of the pore. For this reason we can propose a similar discussion regarding the ability of accepting electrons on the surface. Furthermore, Cu atoms do not exhibit a high susceptibility to an electrophilic or neucleophilic attack, rather it is sensitive to radical attacks. In ap-Zr (6.34a) the eletrophilic FF shows more negative

values around Zr atoms near the *surface* of the pore, thus the electronic structure will remain stable upon electron removal.

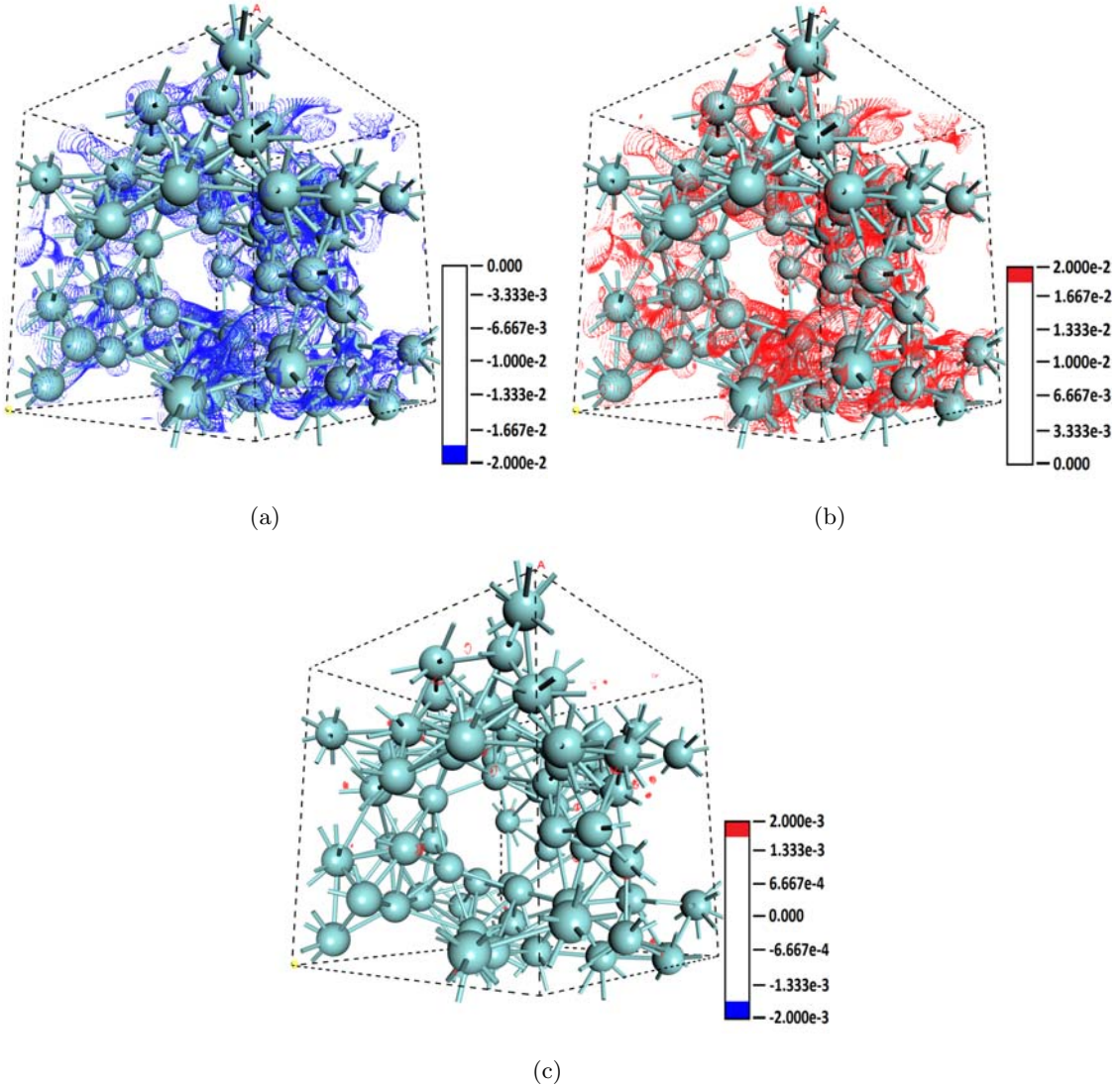

(a) (b)

(c)

Figure 6.34. Fukui functions calculated for ap-Zr represented as field isosurfaces; a) electrophilic (f_N^-; highest eletrophilic sites are marked in blue); b) nucleophilic (f_N^+; highest nucleophilic sites are marked in red); c) radical (f_N^0; highest radical sites are marked in red). The units of the field are Ha/Å^{-3}.

Moreover, the nucleophilic FFs (Figs. 6.33b and 6.34b) suggest an opposition to accepting electrons near the surface up to a certain point near the surroundings of atomic centers. Radical FFs do not provide enough information as electrophilic and nucleophilic FFs do, rather it helps to acknowledge that negative values are not dominant (Figs. 6.33c

and 6.34c); again, we face the problem of the lack of a criterion to establish the pore surface since, qualitatively, we may say that our amorphous porous pure metals could be able to store chemical agents. A quantitative study based on energetic terms is essential [22, 23].

Despite the unclear quantitative behavior—in the chemical context—of the amorphous porous samples generated for this dissertation, FFs provide relevant qualitative information on the chemical reactivity. We must emphasize the fact that the information should be considered carefully and predictive, for FFs are usually applied to relatively small molecules and the viability to extrapolate its usage to solids is unknown. Some people suggest that the values provided by energy calculations are so small so as not to consider the FF as a relevant indicator of chemical reactivity. Nevertheless, in this work it was used due to its qualitative power to contribute to the study of the reactivity of amorphous porous solids as a coarse approximation method.

Conclusions

In the present thesis, topological, electronic and vibrational properties of amorphous and liquid alloys, as well as reactivity studies of amorphous porous alloys were calculated for the Cu-Zr system by means of *ab initio* molecular dynamics simulations. We propose a new approach to generate amorphous and liquid alloys based on the San Diego amorphization method; the expanding lattice method and the dealloying technique were applied to generate amorphous porous metallic structures. Five alloys were chosen in order to span a wide concentration range: Cu_XZr_{100-X} ($X = 20, 36, 50, 64, 80$), and to examine how the properties evolve as a function of the atomic constituents. The topological analysis of the generated amorphous and liquid structures is summarized as follows:

- The structure of the amorphous alloys agrees reasonably well with neutron dispersion and X-ray diffraction experiments since they exhibit a typical pair-distribution-function (PDF) profile of the glassy phase. The second-peak split in the PDFs, related to icosahedron-like short-range order (ILSRO), is present in all the alloys. As a result, the bond-angle distribution calculations show a significant contribution of an icosahedron-like geometry; besides, other Frank-Kasper (FK) triangulated coordination shells arise as complex geometries. The driving mechanism that fosters the formation of distorted icosahedra and FK polyhedra, stabilizing the amorphous network, are the Zr atoms due to the atomic size difference compared to Cu. However, the lowest amount of atoms bonded with 12 neighbors is present when there is equal content of both species: $Cu_{50}Zr_{50}$. This behavior is understood as a competition between the B2 crystalline structure and the amorphous phase, the latter leading to a lower energy than the former; thus, $Cu_{50}Zr_{50}$ concentration would not exhibit a high glass-forming ability as the other four concentrations.

- Since the structure of a material is temperature-dependent, the simulated liquid samples resemble the amorphous behavior of the second-peak split, which means that even at such temperatures there is a strong presence of ILSRO and FK distorted polyhedra. This was supported by BAD calculations which undoubtedly exhibit a substancial presence of such geometries. However, 12-bonded atoms in the liquid were less abundant than in the amorphous, and a similar trend prevailed for $Cu_{50}Zr_{50}$;

therefore, Zr motion plays a paramount role in short-range ordering. Moreover, the presence of a bimodality in the structure factors reinforces the existence of ILSRO to some extent.

Based on the above results the proposed approach was validated, so then the electronic and vibrational properties, where Zr plays a relevant role, were calculated.

In both simulated amorphous and liquid cases the tendency is alike: as Zr content increases, so does the number of states at the Fermi level. The general profile of the electronic density of states (eDOS) is a somewhat narrow peak between -4 and -2 eV due to Cu 3d orbitals and a flat region near the Fermi level which is a contribution of both Cu and Zr p orbitals, and mainly of Zr 4d orbitals. Although a localized-bonding approach in metals may not be adequate, the existence of highly stable complex geometries in the amorphous phase must be related to bonds beyond the metallic kind. We believe that a hybridization process takes place since partial eDOS show increasing contributions form s, p and d orbitals as Zr concentration increases.

eDOS in the amorphous and the crystal for $Cu_{50}Zr_{50}$ exhibits the interesting feature that the number of states at the Fermi level in the amorphous is thrice the value of the crystal. This leads to the idea that, under the BCS theory and the right conditions, qualitatively the amorphous material might have more electrons to form Cooper pairs reaching the superconducting phase. This argument is a coarse approximation because the role of strong coupling must be investigated.

Vibrational densities of states (vDOS) have barely been reported in metallic glasses. In both amorphous and liquid samples a broaden shape with an enhanced population of low frequency modes is found as a result of a large structural disorder. A noteworthy issue in the vDOS of our amorphous and liquid alloys is the presence of negative frequencies, which lack physical meaning and whose number is larger in the liquids; negative frequencies in amorphous come out of the relaxation process, i.e., if a full San Diego approach with quenching stages is applied, negative modes will disappear. For liquids a different approach from the harmonic approximation could be considered instead, like introducing damping and driving forces. Although the phonon spectra presented in this work for liquids alloys should be considered as predictive due to the abscence of experimental counterparts, these results might be used as guideline for further exhaustive theoretical or experimental investigations.

In the last part, the Expanding Lattice method and the dealloying technique were implemented to generate amorphous porous $Cu_{64}Zr_{36}$ alloys (ap-$Cu_{64}Zr_{36}$) based on different initial structures: an unstable cystal and an amorphized sample, and amorphous porous Cu and Zr, correspondingly. We found in ap-$Cu_{64}Zr_{36}$ that the direction in which pores grow is

sensitive to the initial structural configuration; however, "through" pore topology emerges regardless the initial structure. Nevertheless, we cannot estimate the pore size using the depletion criterion as was used for other amorphous porous samples reported previously because not all PDFs have such a drop. Along with these, we found that icosahedron-like and distorted Frank-Kasper geometries appear and they increase with porosity; thus, these geometries affect the stability of the backbone. Despite the results obtained, further investigations are needed in order to see the influence of a larger number of atoms in the simulation box, the short-range order behavior if the cell is optimized and a criterion to estimate the pore size (defining the surface) is needed.

In the samples that were dealloyed we found that Zr tends to stabilize the backbone as porosity increases due to longer bonds. In both amorphous porous Cu and Zr we also observed that ILSRO prevails once dealloyed. This is very relevant because the generation of pure amorphous metals could be approached via porous dealloyed structures since, so far, no amorphous pure bulk metals have been reported. We also found that if the depletion criterion is to be used to quantitatively analyze pore sizes, porosity percentages should be larger than, or around 50%, otherwise the PDF does not show a clear dropping.

Finally, the reactivity was qualitatively studied in terms of the Fukui Functions. Based on our results, we are not able to either assert or reject the idea that our amorphous porous samples are able to act as storage for chemical agents due to the lack of a criterion to define the surface. In spite of the scarcity of quantitative information provided by FFs, the qualitative data is valuable because it supplies a guide to understand the possible behavior that such materials will exhibit.

In summary, based on comparisons with experiment, the present dissertation provides evidence that the implementation of a variant of the San Diego method to generate reliable amorphous and liquid Cu-Zr alloys was successfully carried out. Moreover, this study contributes to the understanding of the atomic-scale structure and electronic and vibrational properties of amorphous an liquid alloys; besides, it pioneers the way to the simulation of bulk metallic glass foams and the extraordinary properties they might exhibit.

Appendix

In Fig. 35 the phase diagram of Cu-Zr alloys is shown. It is important to mention that the melting temperatures of some concentrations are not well defined; therefore, they are indicated with dashed lines.

It is also noteworthy that the concentrations we chose do not have a crystalline counterpart, apart from the 50-50 concentration. This is why we used the B2 50-50 stable crystal to compare the structural transition from the crystalline phase to the amorphous and the liquid.

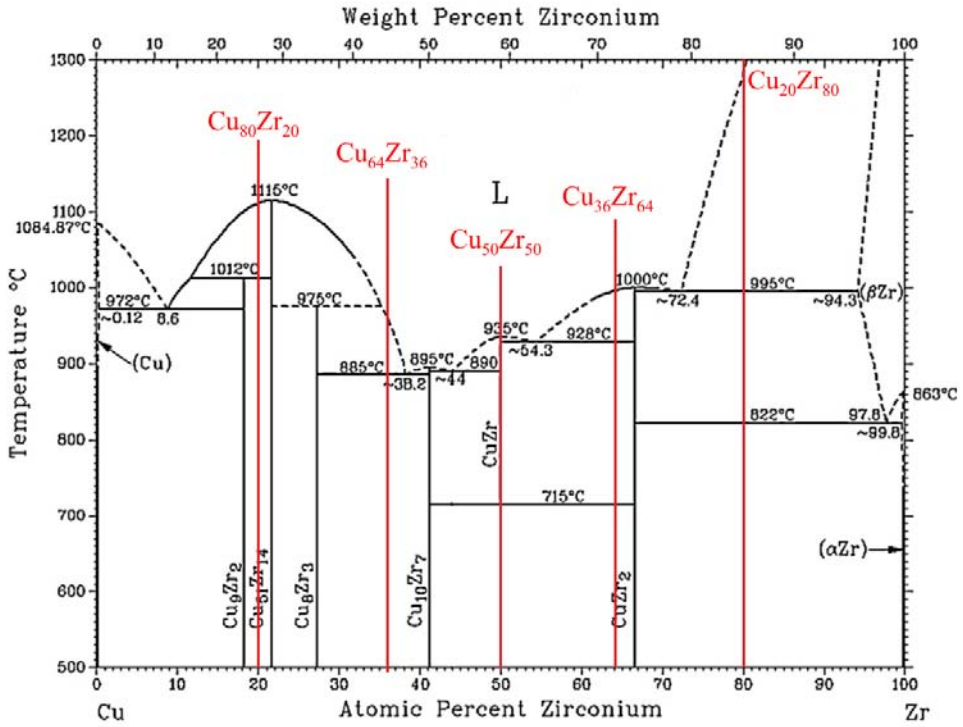

Figure 35. Phase diagram of Cu-Zr alloys. Red lines are the amorphous and liquid concentrations studied in this dissertation.

Bibliography

[1] A. B. Bathia, D. E. Thornton, Phys. Rev. B **2**, 3004 (1970).

[2] N. E. Cusack, *"The Physics of Structurally Disordered Matter: An Introduction"*, IOP Publishing Ltd. (1987).

[3] Y. Waseda, *The Structure of Non-Crystalline Materials*, McGraw-Hill Inc. (1980).

[4] S. R. Elliot, *Physics of Amorphous Materials*, Longman Scientific and Technical (1984).

[5] Y. Waseda, *Anomalous X-Ray Scattering for Materials Characterization*, Springer (2002).

[6] J. Galván Colín, M. Sc. Thesis, Universidad Nacional Autónoma de México, México, 2011.

[7] E. Blaisten-Barojas, Kinam **6A**, 71 (1984).

[8] J. D. Honeycutt, H. C. Andersen, J. Phys. Chem. **91**, 4950 (1987).

[9] D. Faken, H. Jónsson, Comp. Mater. Sci. **2**, 279 (1994).

[10] W. Klement, R. H. Willens, P. Duwez, Nature **187**, 869 (1960).

[11] A. Inoue, X. M. Wang, W. Zhang, Rev. Adv. Mater. Sci. **18**, 1 (2008).

[12] J. Banhart, Prog. Mater. Sci **46**, 559 (2001).

[13] A. H. Brothers, D. C. Dunand, Scripta Mater. **54**, 513 (2006).

[14] J. Erlebacher, M. J. Aziz, A. Karma, N. Dimitrov, K. Sieradzki, Nature **410**, 450 2001.

[15] IUPAC. Compendium of Chemical Terminology, 2nd ed. (the "Gold Book"). Compiled by A. D. McNaught and A. Wilkinson. Blackwell Scientific Publications, Oxford (1997). XML on-line corrected version: http://goldbook.iupac.org (2006-) created by

M. Nic, J. Jirat, B. Kosata; updates compiled by A. Jenkins. ISBN 0-9678550-9-8. doi:10.1351/goldbook.

[16] J. Schroers, C. Veazey, W. L. Johnson, App. Phys. Lett. **82**, 370 (2003).

[17] A. H. Brothers, D. C. Dunand, App. Phys. Lett **84**, 1108 (2004).

[18] M. H. Lee, D. J. Sordelet, App. Phys. Lett. **89**, 021921 (2006).

[19] M. D. Demetreiou, G. Duan, C. Veazey, K. De Blauwe, W. L. Johnson, Scripta Mater. **57**, 9 (2007).

[20] A. H. Brothers, D. C. Dunand, Q. Zheng, J. Xu, J. App. Phys. **102**, 023508 (2007).

[21] L. D. Gelb, MRS Bull. **34**, 592 (2009).

[22] A. A. Valladares, A. Valladares, R. M. Valladares, A. G. Calles, Mat. Res. Soc. Symp. Proc. **971**, Z07-08 (2007).

[23] A. A. Valladares, A. Valladares, R. M. Valladares, Mat. Res. Soc. Symp. Proc. **988**, QQ-09 (2007).

[24] R. M. Valladares, A. Valladares, A. G. Calles, A. A. Valladares Mat. Res. Soc. Symp. Proc. **1042**, S03-28 (2008).

[25] C. Romero, J. C. Noyola, U. Santiago, R. M. Valladares, A. Valladares, A. A. Valladares, Materials **3**, 467 (2010).

[26] C. Romero, A. A. Valladares, R. M. Valladares, A. Valladares J. Non-Cryst. Solids **362**, 14 (2013).

[27] C. U. Santiago-Cortés, L. M. Mejía-Mendoza, R. M. Valladares, A. Valladares, A. A. Valladares, J. Non-Cryst. Solids **358**, 596 (2012).

[28] M. I. Mendelev, D. J. Sordelet, M. J. Kramer, J. Appl. Phys. **102**, 043501 (2007).

[29] X. D. Wang, S. Yin, P. Cao, J. Z. Jiang, H. Franz, Z. H. Jin, Appl. Phys. Lett. **92**, 011902 (2008).

[30] G. Duan, D. Xu, Q. Zhang, G. Zhang, T. Cagin, W. L. Johnson, W. A. Goddard III, Phys. Rev. B **71**, 224208 (2005).

[31] N. Mattern, A. Schöps, U. Kühn, J. Acker, O. Khvostikova, J. Eckert, J. Non-Cryst. Solids **354**, 1054 (2008); N. Mattern, P. Jóvari, I. Kaban, S. Gruner, A. Elsner, V. Kokotin, H. Franz, B. Beuneu, J. Eckert, J. Alloys Compd. **485**, 163 (2009).

[32] N. Jakse, A. Pasturel, Phys. Rev. B **78**, 214204 (2008).

[33] M. Li, C. Z. Wang, S. H. Hao, M. J. Kramer, K. M. Ho, Phys. Rev. B **80**, 184201 (2009).

[34] Y. L. Sun, J. Shen, A. A. Valladares, J. Appl. Phys. **106**, 0735520 (2009).

[35] J. Antonowicz, A. Pietnoczka, W. Zalewski, R. Bacewicz, M. Stoica, K. Georgarakis, A. R. Yavari, J. Alloys Compd. **509S**, S34 (2011).

[36] A. E. Lagogianni, G. Almyras, Ch. E. Lekka, D. G. Papageorgiou, G. A. Evangelakis, J. Alloys Compd. **483**, 658 (2009).

[37] C. Valencia-Balvín, C. Loyola, J. Osorio-Guillén, G. Gutiérrez., Physica B **405**, 4970 (2010).

[38] A. A. Valladares, J. A. Díaz-Celaya, J. Galván-Colín, L. M. Mejía-Mendoza, J. A. Reyes-Retana, R. M. Valladares, A. Valladares, F. Álvarez-Ramírez, D. Qu, J. Shen, Materials **4**, 716 (2011).

[39] D. Holland-Moritz, F. Yang, T. Kordel, S. Klein, F. Kargl, J. Gegner, T. Hansen, J. Bednarcik, I. Kaban, O. Shuleshova, N. Mattern, A. Meyer, Europhys. Lett. **100**, 56002 (2012).

[40] S. G. Hao, C. Z. Wang, M. J. Kramer, K. M. Ho, J. Appl. Phys. **107**, 053511 (2010).

[41] P. Oelhafen, E. Hauser, H.-J. Güntherodt, K. H. Bennemann, Phys. Rev. Lett. **43**, 1134 (1979).

[42] D. Nguyen Manh, D. Mayou, F. Cyrot-Lackmann, A. Pasturel, J. Phys. F: Met. Phys. **17**, 1309 (1987); D. Nguyen Manh, D. Pavuna, F. Cyrot-Lackmann, D. Mayou, A. Pasturel, Phys. Rev. B **33**, 33-5921 (1986).

[43] T. Fujiwara, J. Phys. F: Met. Phys. **12**, L251 (1982).

[44] U. Krey, H. Ostermeier, J. Zweck, Phys. Stat. Sol. B **144**, 203 (1987); H. Ostermeier, U. Krey, Mat. Sci. Engin. **99**, 273 (1988).

[45] Y. Takahara, N. Narita, Mat. Trans. Japan Institute of Metals, **45**, 1172 (2004).

[46] C. G. H. Walker, S. A. Morton, P. K. Hucknall, D. Freig, J. A. D. Matthew, D. Norman, J. Phys. Conden., Matter **9**, 8601 (1997).

[47] T. Hua, L. YunLong, Z. Chong, Z. JiJun, W. Bin, W. Qing, Science China, **54**, 2-249 (2011).

[48] J.-B. Suck, H. Rudin, H.-J. Güntherodt, H. Beck, J. Daubert, W. Gläser, J. Phys. C: Solid St. Phys., **13**, L167 (1980).

[49] S. Kobayashi, S. Takeuchi, J. Phys. C: Solid St. Phys., **13**, L969 (1980).

[50] S. Nakashima, Y. Kawakita, T. Otomo, R. Suenaga, A. Q. R. Baron, S. Tsutsui, S. Kohara, S. Takeda, K. Itoh, T. Fukunaga, M. Hasegawa, J. Phys.: Conf. Series **92**, 012136 (2007).

[51] P. Hohenberg, W. Kohn, Phys. Rev. **136**, B864 (1964).

[52] W. Koch, M. C. Holthausen, *A Chemist's Guide to Density Functional Theory*, 2^{nd} edition, Wiley-VCH Verlag GmbH (2001).

[53] R. G. Parr, W. Yang, *Density-Functional Theory of Atoms and Molecules*, Oxford University Press (1989).

[54] W. Kohn, L. J. Sham, Phys. Rev. **140**, A1133 (1965).

[55] L. H. Thomas, Proc. Cambridge Phil. Soc. **23**, 542 (1927).

[56] E. Fermi, Rend. Accad. Naz. Lincei **6**, 602 (1927).

[57] D. M . Ceperley, B. J. Alder, Phys. Rev. Lett. **45**, 566 (1980).

[58] S. H. Vosko, L. Wilk, M. Nusair, Can. J. Phys. **58**, 1200 (1980).

[59] J. P. Perdew, Y. Wang, Phys. Rev. B **45**, 13244 (1992).

[60] F. Ercolessi, *A Molecular Dynamics Primer*, Spring College in Computational Physics (1997).

[61] F. Álvarez, Tesis Doctoral, Posgrado en Ciencias Físicas, UNAM (2002).

[62] W. G. Hoover, A. J. Ladd, B. Moran, Phys. Rev. Lett. **48**, 1818 (1982).

[63] S. Nosé, Mol. Phys, **52** 255 (1984).

[64] D. C. Rapaport, *The Art of Molecular Dynamics Simulation*, 2nd ed. Combridge University Press (2004).

[65] R. Carr, M. Parrinello, Phys. Rev. Lett. **55**, 2471 (1985).

[66] DMol^3 v.6.0, Accelrys Materials Studio Modelling, Accelrys, Inc. (2012).

[67] B. Delley, J. Chem. Phys. **92**, 508 (1990); B. Delley, J. Chem. Phys. **113**, 7756 (2000).

[68] H. Yoshida, Phys. Lett. A **150**, 262 (1990).

[69] M. Suzuki, J. Math. Phys. **32**, 400 (1991).

[70] E. B. Wilson, J. C. Decius, P. C. Cross, *Molecular Vibrations. The Theory of Infrared and Raman Vibrational Spectra*", Dover Publications, Inc. (1980).

[71] DMol^3 Manual for Accelrys Materials Studio Modeling (2005).

[72] W. Yang, R. G. Parr, *Proc. Natl. Acad. Sci. USA* **82**, 6723 (1985).

[73] R. G. Parr, R. A. Donnelly, M. Levy, W. E. Palke, *J. Chem. Phys.* **68**, 381 (1978).

[74] P. W. Ayers, *J. Math. Chem.* **43**, 285 (2008).

[75] L. J. Bartolotti, P. W. Ayers, *J. Phys. Chem. A* **109**, 1146 (2005).

[76] K. Fukui, T. Yonezawa, C. Nagata, *Bull. Chem. Soc. Jpn.* **27**, 423 (1954).

[77] K. Fukui, T. Yonezawa, H. Shingu, *J. Chem. Phys.* **20**, 722 (1952).

[78] K. Fukui, *Science* **218**, 747 (1987).

[79] P. W. Ayers, W. Yang, L. J. Bartolotti, "Fukui Function", in: P. K. Chattaraj (Ed.), Chemical reactivity theory: a density functional view, CRC Press, pp. 255-268 (2009).

[80] C. U. Santiago Cortés, Ph.D. Thesis, Universidad Nacional Autónoma de México, México, 2012.

[81] C. Romero Ramgel, Ph.D. Thesis, Universidad Nacional Autónoma de México, México, 2014.

[82] E. Y. Peña, M. Mejía, J. A. Reyes, R. M. Valladares, F. Álvarez, A. A. Valladares, J. Non-Cryst. Solids **338-340**, 258 (2004).

[83] C. Romero, Z. Mata, M. Lozano, H. Barrón, R. M. Valladares, F. Álvarez, A. A. Valladares, J. Non-Cryst. Solids **338-340**, 258 (2004).

[84] A. Valladares, R. M. Valladares, F. Álvarez-Ramírez, A. A. Valladares, J. Non-Cryst. Solids **352**, 1032 (2006).

[85] A. A. Valladares, J. Non-Cryst. Solids **353**, 3540 (2007).

[86] A. A. Valladares, A new approach to the *ab initio* generation of amorphous semiconducting structures. Electronic and vibrational studies. In: Glass Materials Research Progress; Wolf J. C., Lange L., editors. Nova Science Publishers Inc., New York: 2008; pp. 61-123.

[87] L. M. Mejía-Mendoza, R. M. Valladares, A. A. Valladares, Molecular Simulation **34**, 989 (2008).

[88] J. A. Reyes-Retana, A. A. Valladares, Comp. Mat. Sci. **47**, 934 (2010).

[89] J. A. Díaz-Celaya, A. A. Valladares, R. M. Valladares, Intermetallics **18**, 1818 (2010).

[90] P. R. Subramanian, D. J. Chakrabarti, D. E. Laughlin, *Phase Diagrams of Binary Copper Alloys*, Ohio: Materials Information Society, (1994).

[91] J. Galván-Colín, A. A. Valladares, R. M. Valladares, A. Valladares, Mater. Res. Soc. Symp. Proc. **1517**, DOI: 10.1557/opl.20121757 (2013).

[92] P. Forey; J. L. Glimois; J. L. Feron; G. Develey; C. Becle; C. R. Acad. Sci. C **291**, 177 (1980).

[93] M. V. Nevitt; J. W. Downey; T. Metall. Soc. Aime **224**, 195 (1962).

[94] E. F. Yaroslav; Y. Klaus; Inorg. Chem. **44**, 8191 (2005).

[95] J. Hafner, J. Phys. F: Met. Phys. **12**, L205 (1982).

[96] J. Hafner, J. Phys. Colloque **C9 46**, 69 (1985).

[97] H. W. Sheng, W. K. Luo, F. M. Alamgir, J. M. Bai, E. Ma, Nature **439**, 419 (2006).

[98] F. C. Frank, J. S. Kasper, Acta Cryst. **1**, 184 (1958).

[99] F. C. Frank, J. S. Kasper, Acta Cryst. **12**, 483 (1959).

[100] A. Hirata, L. J. Kang, T. Fujita, B. Klumov, K. Matsue, M. Kotani, A. R. Yavari, M. W. Chen, Science **341**, 376 (2013).

[101] A. J. C. Wilson, *International Tables for Crystallography* ***C***, 3rd Edition, Kluwer Academic Publishers 2004.

[102] A. Valladares, R. M. Valladares, F. Álvarez-Ramírez, A. A. Valladares, J. Non-Cryst. Solids **352**, 1032-1036 (2006).

[103] Z. Mata-Pinzón, A. A. Valladares, R. M. Valladares, A. Valladares, PLoS ONE, DOI: 10.1371/journal.pone.0147645 (2016).

[104] F. Faupel, W. Frank, M.-P. Macht, H. Mehrer, V. Naundorf, K. Rätzke, H. R. Schober, S. K. Sharma, H. Teichler, Rev. Mod. Phys. **75**, 237-280 (2003).

[105] S. Takeno, M. Gôda, Prog. Theor. Phys. *45*, 331-352 (1971).

[106] P. B. Thakor, P. N. Gajjar, A. R. Jani, Pramana-J. Phys. *72*, 1045-1049 (2009).

[107] A. M. Vora, Journal of Non-Oxide Glasses *2*, 91-96 (2010).

[108] J-B. Suck, Experimental investigations of collective excitations in disordered matter, In: Collective dynamics of nonlinear and disordered systems, Eds. G. Radons, W. Just, P. Häussler, Springer Berlin, Heidelberg, pp. 147-170 (2005).

[109] M. Chen, NPG Asia MAter. **3**, 82-90 (2011).

[110] A. M. James, M. P. Lord, *Macmillan's Chemical and Physical Data*, Macmillan Press, Basingstoke, UK (1992).

[111] P. Bultnick, R. Carbó-Dorca, W. Langenaeker, J. Chem. Phys. **118**, 4349-4356 (2003); P. Bultnick, R. Carbó-Dorca, J. Math. Chem **34**, 67-74 (2003).

[112] J. Melin, P. W. Ayers, J. V. Ortiz, J. Phys. Chem. A **111**, 10017-10019 (2007).